Thesis presented to the Instituto Tecnológico de Aeronáutica, in partial fulfillment of the requirements for the degree of Doctor of Science in the Program of Space Science and Technology, Area of Sensors and Space Actuators.

Márcio Martins da Silva Costa

COMPACT POLARIMETRY RECONSTRUCTION ALGORITHM FOR A GEOPHYSICAL MEDIA WITH VOLUMETRIC SCATTERING USING L-BAND QUAD-POL DATA

Thesis approved in its final version the signatories below:

Angelo Passaro

Prof. Dr. Angelo Passaro
Advisor

Dr. Rafael Lemos Paes
Co-advisor

Prof. Dr. Pedro Teixeira Lacava
Pro-Rector of Graduate Courses

Campo Montenegro
São José dos Campos, SP – Brazil.
2019

Cataloging-in Publication Data
Documentation and Information Division

Costa, Márcio Martins da Silva
Compact Polarimetry Reconstruction Algorithm for a Geophysical Media with Volumetric Scattering using L-band Quad-POL Data / Márcio Martins da Silva Costa.
São José dos Campos, 2019.
152 f.

Thesis of Doctor of Science – Course of Space Science and Technology, Area of Space Sensors and Actuators – Instituto Tecnológico de Aeronáutica, 2019. Advisor: Professor Dr. Angelo Passaro. Co-orientador: Rafael Lemos Paes.

1. Compact Polarimetry. 2. Radar polarimetry. 3. Radar remote sensing. 4. Spaceborne radar. 5. Synthetic Aperture Radar (SAR). I. Instituto Tecnológico de Aeronáutica. II. Compact Polarimetry Reconstruction Algorithm for a Geophysical Media with Volumetric Scattering using L-band Quad-POL Data.

BIBLIOGRAPHIC REFERENCE

COSTA, Márcio Martins da Silva **Compact Polarimetry Reconstruction Algorithm for a Geophysical Media with Volumetric Scattering using L-band Quad-POL Data**. 2019. 152 f. Thesis of Doctor of Science in Space Science and Technology – Instituto Tecnológico de Aeronáutica, São José dos Campos.

CESSION OF RIGHTS

AUTHOR’S NAME: Márcio Martins da Silva Costa
PUBLICATION TITLE: Compact Polarimetry Reconstruction Algorithm for a Geophysical Media with Volumetric Scattering using L-band Quad-POL Data
PUBLICATION KIND/YEAR: Thesis / 2019

Márcio Martins da Silva Costa
Divisão de Sistemas Espaciais - Space System Division
Comissão de Coordenação e Implantação de Sistemas Espaciais (CCISE)
Commission for Coordination and Deployment of Space Systems (CCISE)
Esplanada dos Ministérios - Bl. M, Ed. Anexo, Brasília-DF, CEP: 70.045-900

COMPACT POLARIMETRY RECONSTRUCTION ALGORITHM FOR A GEOPHYSICAL MEDIA WITH VOLUMETRIC SCATTERING USING L-BAND QUAD-POL DATA

Márcio Martins da Silva Costa

Thesis Committee Composition:

Prof. Dr.	Gustavo Soares Vieira	President	ITA
Prof. Dr.	Angelo Passaro	Advisor	ITA
Prof. Dr.	Renato Machado	Internal Member	ITA
Prof. Dr.	Fernando Pellon de Miranda	External Member	COPPE-UFRJ
Prof. Dr.	João Antonio Lorenzzetti	External Member	INPE

ITA

"With love and affection, I dedicate this work to the lights that God has sent to illuminate my ways: my parents Martins and Eletice, my brother Marcelo, my children Letícia and João Martins, my beloved wife Graciete, and our Master Jesus. Reasons of my life."

Acknowledgments

Ao finalizar os trabalhos deste Doutorado, deparo-me com esta seção ainda em branco, que talvez seja a mais difícil de escrever. Tantos me ajudaram, tantas organizações me apoiaram, o que torna hercúlea a tarefa de reunir em uma única página a gratidão que tenho por todos. Limito-me, assim, aos que efetivamente tiveram ação direta para que esta pesquisa se concretizasse. Em poucas linhas, seguem as minhas imensuráveis palavras de gratidão.

Capitão de Mar e Guerra Ken Williams Schonfelder, Marinha do Brasil, meu então Diretor em 2013. Abriu mão de meus préstimos, acreditou neste futuro e em seus potenciais desdobramentos em favor do país. Sua assinatura me levou às portas do ITA. Gratidão!

Prof. Dr. José Claudio Mura, Instituto Nacional de Pesquisas Espaciais (INPE), e Prof. Dr. David Fernandes, Instituto Tecnológico de Aeronáutica (ITA). Dispenderam momentos preciosos me orientando, sendo meus mestres e amigos. Sempre serão uma referência para mim. Gratidão!

Prof. Dr. Angelo Passaro, Instituto de Estudos Avançados (IEAv/ITA). Recebeu-me como orientador no ITA nos últimos dois anos do curso. Referência de profissionalismo, dedicação, insistência e paciência. Além destes, a amizade e o apreço serão sempre as marcas destes anos juntos. Gratidão!

Graciete Costa, minha amada esposa. Como ser um aluno de Doutorado enquanto observava a imagem de minha família reunida no lar sem a minha presença? Por vários momentos deixei de ser esposo, deixei de ser pai e quase quis deixar de ser aluno. Mas me concedeu a base segura de compreensão, força, carinho e amor que não deixaram a minha luz esmorecer. Sem você nunca teria concluído este trabalho que, juntos, deixamos de legado e incentivo aos nossos amados filhos, Letícia e João Martins. Gratidão! Te amo muito!

Por fim, dedico as últimas linhas à *Inteligência Suprema, causa primária de todas as coisas*. Sem acreditar em Seus desígnios, em Seu amor e em Sua luz, nada faria. A Ti, a maior gratidão de todas por me permitir ser um mero aprendiz nesta maravilhosa escola azul a cruzar o universo.

“If I have seen further than others,

it is by standing upon the shoulders of giants.”

Sir Isaac Newton

Resumo

Um dos objetivos do Programa Espacial Brasileiro (PEB) é lançar um satélite SAR (Radar de Abertura Sintética) nos próximos anos. Para prover subsídios para futuros estudos de viabilidade, esta Tese propõe um algoritmo de reconstrução de Polarimetria Compacta (CP) para um meio geofísico com espalhamento volumétrico. Este estudo considera a banda L, mecanismos de espalhamento volumétrico e um meio geofísico com propriedades de simetria azimutal. A principal contribuição deste trabalho é a introdução de um algoritmo para CP, considerando a simetria azimutal. Essa abordagem é uma questão importante para os sistemas de satélite SAR que irão operar em baixas latitudes brasileiras, especialmente em regiões com predominância de mecanismos de espalhamento volumétrico, como a floresta Amazônica, e áreas do país cobertas por irregularidades ionosféricas, como bolhas de plasma e distúrbios ionosféricos itinerantes de média escala (MSTIDs). Os processos de pseudo reconstrução de imagens SAR obtidas a partir deste novo algoritmo de CP apresentam resultados melhores que os métodos CP tratados na literatura para o cenário considerado. O coeficiente de correlação de Pearson, o Erro Quadrático Médio (RMSE) e gráficos de espalhamento são usados para analisar o processo de pseudo reconstrução, considerando as imagens originais Quad-POL.

Palavras-Chave: Polarimetria Compacta; Polarimetria radar, Sensoriamento remoto por radar, Sistema espacial radar, Radar de Abertura Sintética (SAR).

Abstract

One of the objectives of the Brazilian Space Program (PEB) is to launch a Synthetic Aperture Radar (SAR) satellite in the next years. To provide subsidies for the future feasibility studies, this Thesis proposes a Compact Polarimetry (CP) reconstruction algorithm for a geophysical media with volumetric scattering. This study considers the L-band, volume scattering mechanisms, and a geophysical medium with azimuthal symmetry properties. The main contribution of this work is the introduction of an algorithm for CP, considering the azimuthal symmetry. This approach is an important issue for SAR satellite systems that will operate in Brazilian low latitudes, especially in regions with volume scattering mechanisms such as the Amazon rainforest, and in the areas of the country covered by ionospheric irregularities, as plasma bubbles and Medium Scale Traveling Ionospheric Disturbances (MSTIDs). The process of pseudo reconstruction of SAR images obtained from this new CP algorithm presents better results than the CP methods discussed in the literature for the considered scenario. Pearson's correlation coefficient, Root Mean Square Error (RMSE), and scatter plots are used to analyze the pseudo reconstruction process regarding the original Quad-POL images.

Keywords: Compact Polarimetry, Radar polarimetry, Radar remote sensing, Spaceborne radar, Synthetic Aperture Radar (SAR).

List of Figures

List of Tables

List of Abbreviations and Acronyms

ALOS-2	Advanced Land Observing Satellite-2
AEB	Brazilian Space Agency
DEMs	Digital Elevation Models
FAB	Brazilian Air Force
GIS	Geographic Information Systems
PEB	Brazilian Space Program
CCISE	Commission for Coordination and Implementation of Space Systems
Co-POL	Linear polarization or co-polarized (HH and VV)
CP	Compact Polarimetry
Cross-POL	Cross-polarization (HV and VH)
DBF	Digital beamforming
DLR	German Aerospace Center
Full-POL	Full Polarimetric / Polarimetry
HH	Horizontally polarized transmitted and received
HV	Horizontally polarized transmitted and vertically polarized received
Hybrid-POL	Hybrid Polarimetric mode
IBGE	Brazilian Institute of Geography and Statistics
IMO	International Maritime Organization
ISRO	Indian Space Research Organization
JAXA	Japan Aerospace Exploration Agency
JPL	NASA Jet Propulsion Laboratory
MCTIC	Brazilian Ministry of Science, Technology, Innovations and Communications

MSTIDs	Medium Scale Traveling Ionospheric Disturbances
NASA	National Aeronautics and Space Administration (USA)
NISAR	NASA-ISRO Synthetic Aperture Radar
PALSAR	Phased Array type L-band Synthetic Aperture Radar-2
PESE	Brazilian Strategic Space Systems Program
PRF	Pulse Repetition Frequency
RCM	RADARSAT Constellation Mission
Rhc	Right Circular Polarization on transmission
RISAT-1	Radar Imaging Satellite-1
RMSE	Root Mean Square Error
ROI	Regions of Interest
SAR	Synthetic Aperture Radar
SMAP	Soil Moisture Active Passive
TEC	Total Electron Content
TSX	TerraSAR-X
VH	Vertically polarized transmitted and horizontally polarized received
VV	Vertically polarized transmitted and received

List of Symbols

c_0	Speed of light
C_{cp11}	Covariance matrix component of a system with right circular polarization on transmission
C_{cp12}	Covariance matrix component of a system with right circular polarization on transmission
C_{cp21}	Covariance matrix component of a system with right circular polarization on transmission
C_{cp22}	Covariance matrix component of a system with right circular polarization on transmission
$C_{az}^{CP(3\times3)}$	Compact Polarimetry Covariance matrix (3×3) after pseudo reconstruction using CP_{az} algorithm
$C_{sr}^{CP(3\times3)}$	Compact Polarimetry Covariance matrix (3×3) after pseudo reconstruction using Souyris et al algorithm
$C^{Full-POL}$	Covariance matrix of a Full-POL system
$C^{Full-POL(3\times3)}$	Covariance matrix (3×3) of a Full-POL system
$C_{rot}^{Full-POL(3\times3)}$	Covariance matrix (3×3) of a Full-POL system for geophysical media with rotation symmetry properties
$C_{az}^{Full-POL(3\times3)}$	Covariance matrix (3×3) of a Full-POL system for geophysical media with azimuthal symmetry properties
C_{co-POL}	Covariance matrix component of a system with right circular polarization on transmission with only the co-POL terms

C_{cr-POL}	Covariance matrix component of a system with right circular polarization on transmission with only the cross-POL terms
C_{res}	Covariance matrix component of a system with right circular polarization on transmission with only the residual terms
C_{Rhc}	Covariance matrix of a system with right circular polarization on transmission
CP_{az}	Proposed algorithm for Compact Polarimetry, considering the azimuthal symmetry
δ_h	Phase angle of the horizontal component of the electric field
δ_v	Phase angle of the vertical component of the electric field
$\vec{E}$	Transmitted electric field vector
E_h	Horizontal component of the electric field
E_v	Vertical component of the electric field
E_{0h}	Amplitude of E_h
E_{0v}	Amplitude of E_v
$\vec{E}_{hv}^{i}$	Incident wave
$\vec{E}_{hv}^{s}$	Scattered wave
$\vec{E}(z)$	Electric field that propagates on the z axis
$\vec{E}(z,t)$	Instantaneous electric field
$\vec{E}_h(z)$	Horizontal component of the Electric field that propagates on the z axis
$\vec{E}_v(z)$	Vertical component of the Electric field that propagates on the z axis
$\vec{e}_h$	Unit vectors in the direction h

$\vec{e}_v$	Unit vectors in the direction v
ε'	Electric permissivity
I_0	Intensity parameter of the electromagnetic wave polarization ellipse
$\Im$	Imaginary part of the complex quantity
$\vec{J}$	Stokes vector
$\vec{J}_r^T$	Jones vector associated to the reception
$\vec{J}_t$	Jones vector associated to the transmission
k_0	Wavenumber
k_r	Complex constant
$\vec{k}$	Vector notation of Sinclair matrix
$\vec{k}_{Rhc}$	Vector notation of Sinclair matrix of a system with right circular polarization on transmission
n	Number of iterations of the algorithm
N	Nord et al. parameter
p	Wave polarization degree
p_x	Total number of pixels
μ	Magnetic permeability
R	Distance between the SAR sensor and the target
r	Pearson correlation coefficient
$\Re$	Real part of the complex quantity
ρ_{az}	Complex correlation or degree/magnitude of coherence between S_{HH} and S_{VV} for CP_{az} algorithm
ρ_{HH-VV}	Complex correlation or degree/magnitude of coherence between S_{HH} and S_{VV}

$\rho_{HH-VV}^{(0)}$	Complex correlation or degree/magnitude of coherence between S_{HH} and S_{VV} at the initialization of the Compact Polarimetry algorithm
$\rho_{HH-VV}^{(0)}$	Complex correlation or degree/magnitude of coherence between S_{HH} and S_{VV} after *n* iteration of the algorithm
S	Sinclair matrix, or Scattering matrix
S_{1-4}	Stokes parameters
S_{HH}	Scattering matrix component considering a wave transmitted with *h* polarizations and the respective echo signal, a wave with *h* polarization
S_{HV}	Scattering matrix component considering a wave transmitted with *h* polarizations and the respective echo signal, a wave with *v* polarization
S_{RH}	Scattering matrix component considering wave transmitted circularly to the right and the respective echo signal, a wave with *h* polarization
S_{RV}	Scattering matrix component considering wave transmitted circularly to the right and the respective echo signal, a wave with *v* polarization
S_{VH}	Scattering matrix component considering a wave transmitted with *v* polarizations and the respective echo signal, a wave with *h* polarization
S_{VV}	Scattering matrix component considering a wave transmitted with *v* polarizations and the respective echo signal, a wave with *v* polarization
Υ	The true data
$\hat{\Upsilon}$	The estimated data generated from an estimator
Υ_i	The value on pixel in location *i*
$\Upsilon_{\max}^{\Psi}$	The maximum value of RMSE obtained in Souyris, Nord, and CP_{az} algorithms for a given value of Ψ.
ϕ	Auxiliary angle of the electromagnetic wave polarization ellipse

χ_p	Ellipticity angle of the electromagnetic wave polarization ellipse
X_{az}	Equivalent to $\left\langle \left\|S_{HV}\right\|^2 \right\rangle$ for CP_{az} algorithm
X_{nd}	Equivalent to $\left\langle \left\|S_{HV}\right\|^2 \right\rangle$ for Nord et al. algorithm
X_{sr}	Equivalent to $\left\langle \left\|S_{HV}\right\|^2 \right\rangle$ for Souyris et al. algorithm
$X_{az}^{(n)}$	Value of the Equivalent to $\left\langle \left\|S_{HV}\right\|^2 \right\rangle$ after *n* iteration of the CP_{az} algorithm
$X_{sr}^{(n)}$	Value of the Equivalent to $\left\langle \left\|S_{HV}\right\|^2 \right\rangle$ after *n* iteration of the Souyris et al. algorithm
$X_{nd}^{(n)}$	Value of the Equivalent to $\left\langle \left\|S_{HV}\right\|^2 \right\rangle$ after *n* iteration of the Nord et al. algorithm
ψ_p	Inclination angle of the electromagnetic wave polarization ellipse
Ψ	Faraday rotation angle
ω	Angular frequency
ω_c	Carrier frequency in radians
$(\cdot)^T$	Denotes that the matrix is transposed
$\langle \cdot \rangle$	Indicates the spatial media
$(\ )^H$	Means the transposed and complex conjugate (Hermitian operator).
$(\ )^*$	Indicates the complex conjugate

Index

1. INTRODUCTION

1.1. Motivation

The immense continental region in which Brazil is circumscribed is a real challenge for monitoring and surveillance of the national territory in real-time. The Brazilian Institute of Geography and Statistics (IBGE) defines six large continental biomes in the country: Amazon rainforest, Atlantic Forest, Caatinga, Savanna, Pantanal, and Pampa. The first one has an approximate area of 4 million square kilometers, which is equivalent to about 49.3 percent of the entire national territory [1], [2]. Beyond this substantial dimension, according to an agreement established with the International Maritime Organization (IMO), Brazil is responsible for Search and Rescue Operations in a vast oceanic area that comprises about 10 million square kilometers.

This extensive area requires remote sensing activities, providing data as fast as possible that may lead to information on deforestation, forest fires, oil spills at sea, illicit border actions, slides, floods, to support precision agriculture, among other occurrences and strategic information. In this context, space system's products can bring relevant solutions supporting various users who employ images in their activities. In 2019, the Brazilian Space Agency (AEB), an autarchy linked to the Ministry of Science, Technology, Innovations and Communications (MCTIC), started to review the Brazilian Space Program (PEB) in partnership with the Commission for Coordination and Implementation of Space Systems (CCISE), a Brazilian Air Force (FAB) organization responsible for establishing the strategies of implantation of Brazilian Strategic Space Systems Program (PESE). A Synthetic Aperture Radar (SAR) satellite mission is considered in this context for the next years.

This Thesis provides some insights into the use of Compact Polarimetry (CP) and the L-band for future Definition of Mission Objectives [3]. The L-band has been exploited by various space missions and remains the focus of space agencies. The recent portfolio of missions can be exemplified by ALOS-2 (Japan Aerospace Exploration Agency - JAXA), launched in 2014, and ALOS-4, scheduled to be launched in 2020 to replace the first one. Another example is the NASA ISRO SAR satellite. This mission is a partnership between the National Aeronautics and Space Administration (NASA) and the Indian Space Research Organization (ISRO), aiming to put the first dual-frequency SAR satellite in orbit in 2021, operating in the L and S-bands. The last example is the multiresolution SAR satellite Tandem-L Mission to be launched in 2022 by the German Aerospace Center (DLR), for creating detailed digital elevation models (DEMs) [4].

Low frequency is an interesting alternative for Brazil, considering the dimensions of the Amazon rainforest and other biomes that have some forest formation. With the ability to penetrate through the leaves canopy [5], L-band can provide, e.g., prior identification of illicit movements under the treetops aimed at deforestation activities. At the Atlantic Ocean area, L-band can be applied for monitoring sea traffic and oil spill, even with an average spatial resolution of 3 to 5 meters.

These scenarios, forest and sea, have their scattering characteristics leading to a unique study for each area. Therefore, take into account the diversity of biomes distributed in a vast continental area, the option in this study is to consider the general mechanisms of volumetric scattering, whose behavior is expected to be compatible with azimuthal symmetry [5].

Azimuthal symmetry is a group of symmetry encountered in remote sensing of the geophysical environment. The other groups are reflection, rotation and centrical symmetry [5], all described in the appendix A. Azimuthal symmetry occurs when the scattering of the environment has the characteristics of the rotation, and the reflection groups at the same time.

Most previous studies had been used the reflection symmetry as the base for investigation CP [6]–[13]. However, considering the premises adopted for the Brazilian scenario and the fact that the Earth's ionosphere above this country characterizes an environment with irregularities, such as plasma bubbles and Medium Scale Traveling Ionospheric Disturbances (MSTIDs), with characteristics of rotation symmetry [5], [14], the main contribution of this research is to analyze a proposed algorithm for CP, considering the azimuthal symmetry (from now on called CP_{az} algorithm).

1.2. A Brief Update on SAR Technology

The ability to monitor large areas with high-resolution images, independent of daylight, vegetal and cloud coverage, smoke, and weather conditions, gives to SAR system advantages over optical sensors. The SAR also can penetrate vegetation and soil.

The cost associated with spaceborne SAR is relatively high. However, the coverage and the huge amount of data generated by these sensors, allied to the effort to optimizing geospatial data collection have boosted the development of new SAR technologies However the coverage and the huge amount of data generated by this sensors, allied to the effort to optimize geospatial data collection have boosted the development of new SAR technologies [15].

In fact, the use of SAR satellites has grown in the last years. Several missions are already operational, and there are at least ten new missions to be launched in the next five years [4], [16].

The information obtained after the processing of SAR data are valuable for several civilian applications, such as the systematic monitoring and analysis of [17]:

a) Plantation and deforestation, forest biomass change, forest height, forest fire, vertical forest structure, species, growth, crop classification (applications in the biosphere);

b) Volcanic activities, earthquakes, landslides, tectonic plates (applications in geo/lithosphere);

c) Ice cover and mass change, soil moisture, flooding, ocean currents, water level change, oil pollution, river flow, water resources in the deserts (applications in hydro/cryosphere);

d) Urbanization, traffic, urban density (urban applications), among others.

SAR data also have also several applications in Defense providing, for instance [18]:

a) Capacity to access, manipulate, analyze, and manage spatially reference data for mission planning in Geographic Information Systems (GIS);

b) Operational environment awareness;

c) Monitoring of borders;

d) Surveillance of ship traffic;

e) Identification and navigation;

f) Detection and surveillance of targets, among others.

Until 2014, the most conventional spaceborne SAR systems have used a planar antenna. In general, a few paths of transmission and reception elements are employed to steer the antenna beam towards the swath area [19]. This approach limits the acquisition of SAR images combining high-resolution and wide-swath coverage. The SAR process involves the use of the Doppler shift generated by the relative movement to the ground. If the goal is to have a high-resolution in azimuth, the Doppler bandwidth must be higher on the receiver of the SAR, which implies in to increase the Pulse Repetition Frequency (PRF). However, if the PRF is increased, the echo window length is reduced to avoid the interference between consecutive pulses of the reflected signals, implying in the reduction of the swath width. In other words, with conventional technologies, it seems that it’s not possible to have high-resolution and wide swath at the same time [17], [20].

In recent years, several new techniques have been developed with the purpose to overcome this restriction. However, two of them are attracting more interest because of their anticipated advantages compared with current systems. The first is the use of offset reflector antennas, and the second is the Compact Polarimetry.

Offset reflector antennas are not new technology. Since 1983 missions as Venera 15/16, Cassini, and Magellan, launched in deep space, have used reflector antenna resources [21].

Years later, in 1988, Kare [22] introduced an offset architecture during the joint studies conducted by NASA/ Jet Propulsion Laboratory (JPL) and DLR for the Tandem-L project.

The heritage of the successful employment of reflector antennas over the years has enhanced the trend to implement new designs in modern SAR systems [23].

In 2015 NASA/JPL launched the Soil Moisture Active Passive (SMAP) mission, an L-band SAR satellite outfitted with a 6 m mesh deployable offset reflector antenna able to provide high spatial resolution with a 1000 km swath [24].

Some examples of the next scheduled SAR mission using an offset reflector antenna are the NISAR mission and the Tandem-L mission. The first one is the joint NASA-ISRO Earth-observing mission to make global measurements of the causes and consequences of land surface changes, beyond other applications as ecosystem disturbances, ice sheet collapse, and evaluation of natural hazards. The NISAR is going to be the first SAR satellite to use two different radar frequencies (S and L-band). In this case, the mechanical characteristic of the offset reflector antenna is being associated with digital beamforming (DBF) techniques to implement the SweepSAR mode. This mode consists of an one-dimensional phased array feed that illuminates a narrow segment of the 12 m antenna reflecting surface on the transmission, enabling to cover 242 km wide swaths on the ground. NISAR is planned to be launch in December 2021 (Figure 1.1) [16], [25].

Figure 1.1 – Artistic conception of the deployed NASA–ISRO NISAR where it can be identified the Offset Reflector Antenna (up), the boom assembly (middle), and the spacecraft bus (down). (image credit: NASA/JPL-Caltech, available in [16]).

The second one, the Tandem-L mission (Figure 1.2), foresees the employment of two formation-flying SAR satellites to monitor the dynamic process on the Earth’s surface. The Tandem-L concept associates a mesh deployable offset reflector antenna with a DBF technique, in order to provide a 350 Km wide swath with an azimuthal resolution of 7m [16].

Both missions have some advantages over conventional SAR. They require less power to transmit than the traditional technologies, are relatively immune to range ambiguities, are simpler to implement, are better suited for longer wavelength systems, such as L-band, and they do not require extremely high data transmission rates. Additionally, the realization of a Hybrid Polarimetric (Hybrid-POL, mode described below) system is easier than with an active Planar Antenna, and the beam shape is generated according to the mechanical molding of the reflector dish. In this case, each feeder illuminates a segment of the antenna dish that reflects to certain range of the target area. The processing of the echo signals from each feeder allows building a mosaicking of sub-swaths. This is the method to generate a large swath. [17], [26], [27].

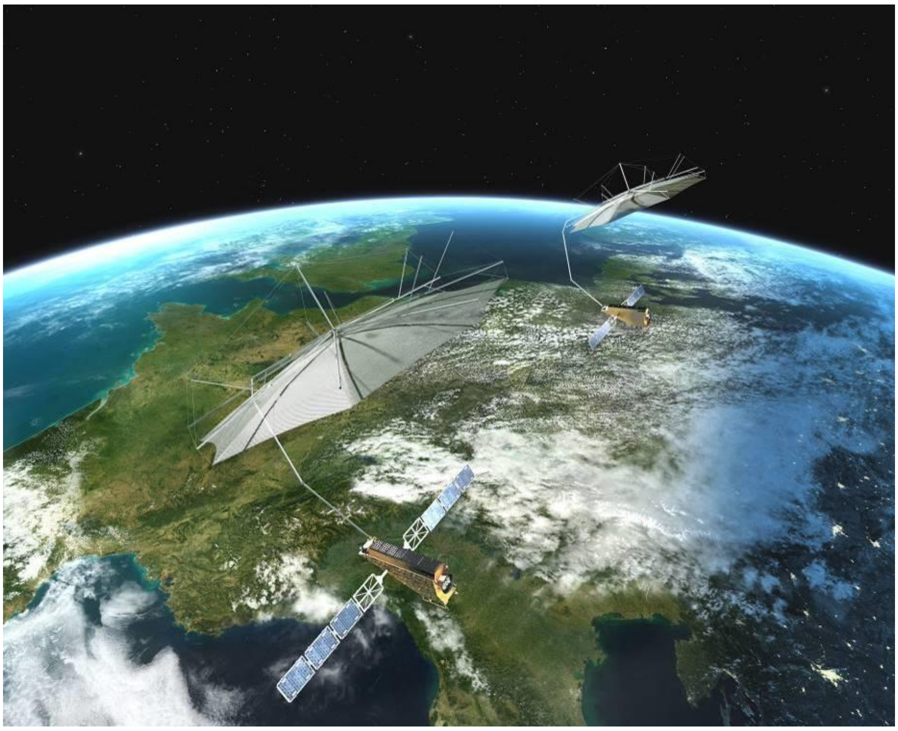

Figure 1.2 – Artistic conception of the deployed Tandem-L
(image credit: Microwaves and Radar Institute - DLR, available in [28]).

Concerning CP, the object of this Thesis, the technique was introduced by Souyris et al., in 2005 [6] (from now on called just Souyris). The objective was to reduce the cost and the complexity of the space segment that employed Full Polarimetric (Full-POL) in their systems.

The first satellite to operate in CP mode was the Mini-SAR sensor incorporated in the Chandrayaan-1 mission, launched by ISRO in 2008. The principal goal of the Mini-SAR was to systematically map the surface polewards of 80° latitude for both poles with the use of S-band. The Mini-SAR used a Hybrid-POL technique, transmitting a left-circular polarized signal and receiving the linear Horizontal and Vertical polarization signals coherently [29].

Currently, RISAT-1 missions (Radar Imaging Satellite-1), ALOS-2, and RADARSAT Constellation Mission (RCM) are the missions that have incorporated CP modes in their payloads.

RISAT-1 is a C-band SAR remote-sensing mission launched on April 26th, 2012 from the Indian Space Research Organization - ISRO, assuming 536 Km heliosynchronous orbit. It has been the first space system to operate the Hybrid-POL CP mode. Due to its features, RISAT-1 can provide high-resolution images (around 1 m) with 100 km swath. The mission has been supporting the worldwide community of remote sensing with SAR data. It is expected that the mission will continue through the RISAT-1A mission, which can be launched in March 2020 [30].

Another current orbital SAR system that employs CP is the ALOS-2 (Advanced Land Observing Satellite-2). The mission was launched on May 24th, 2014, by JAXA from the Yoshinobu Launch Complex located at Tanegashima Space Center in Japan. The SAR Radar system named Phased Array type L-band Synthetic Aperture Radar-2 (PALSAR) was included in ALOS-2 to monitor Earth's dynamic processes, such as earthquakes, volcanoes, biomass changes, among others. In this mission, the CP mode intends to be evaluated experimentally [16].

RCM is a set of three identical small satellites launched on Jun 12th, 2019. It will allow accessing 90% of Earth’s surface with a high spatial resolution (<1.3m in spot mode) and high temporal resolution, i.e., up to four times a day. Each satellite will have a small planar antenna, which restricts the swath to about 30 to 40 km in stripmap mode. However, it is expected that the constellation will reach 100 km swath by the image composition from the three satellites [16]. It is the first spaceborne SAR to employ Hybrid-POL mode in the world in operational mode.

More insights on SAR technology are presented in appendix C [31] and D [32].

1.3. Thesis Objective

Once presented some issues about the motivation and SAR technology, from now on the focus of this works turns to the CP, which is the subject of this Thesis.

The usual CP model adopted in previous works has been the Souyris’ approach based on the case in which the illuminated scenario has reflection symmetry with relation to the incident plane. This concept allows implementing simplifications, taking into account the absence of ionospheric effects [6], [12], [33], [34].

This research proposes an approach to the CP algorithm considering a geophysical media with azimuthal symmetry properties. This choice is based on the fact that most generally, the volume scattering mechanisms could behave in a way compatible with this type of symmetry. The objectives of this Thesis are to evaluate the results of an algorithm for CP considering the azimuthal symmetry and to provide some insight on the use of CP for future Brazilian L-band SAR Definition of Mission Objectives [3].

The evaluation of the use of the azimuthal symmetry for the analysis of SAR images from satellite systems operating in the Brazilian low latitudes, especially in regions with volume scattering mechanisms such as the Amazon rainforest, and covered by ionospheric irregularities, such as plasma bubbles and MSTIDs [5], [14], can contribute to enhance the image quality and providing more detailed information.

It should be emphasized that this Thesis will not explore the theoretical basis involving SAR systems, as signal processing and Polarimetry. The author considers that there is a vast literature on these subjects [20], [35]–[40].

1.4. Thesis Organization

This Thesis is organized into six chapters. The first chapter presents the motivation of this document, a brief update on SAR technology, the Thesis objectives, and how it is organized. In addition to the update on SAR, two papers are included in Appendices C and D. Chapter 2 presents the mathematical modeling needed to develop the CP. The first Section introduces a literature review, followed by the polarimetric model, the reciprocity theorem, and the Hybrid-POL, which is the CP mode assumed in this research problem. Chapter 3 presents the main reconstruction methods considered in the literature, although other methods were introduced in other works [12], [41]. Souyris [6] and Nord et. al [7] algorithms are developed in Sections 3.1 and 3.2, respectively. Section 3.3 presents the main contribution of this Thesis, where the CP algorithm considering the azimuthal symmetry is introduced (CP_{az} algorithm). Chapter 4 presents the adopted methodology. Chapter 5 presents the results and the analysis, and chapter 6 presents the conclusions and final considerations. Additionally, we have included six appendices. Appendix A summarized the symmetry properties in polarimetric remote sensing presented by Nghiem et al. [5] to provide fundamental understanding of the concepts discussed in this Thesis. Likewise, fundamentals of the effects of the Ionosphere in the scattering matrix are presented in Appendix B. This Appendix also introduce the mathematical model used to find the value of the Faraday rotation angle Ψ. Appendices C and D present an update on SAR, as mentioned before. Appendix E presents Tables and Figures of the results from Section 5.3. At last, Appendix F describes the bands of radar frequency proposed by Institute of Electrical and Electronic Engineers (IEEE).

2. COMPACT POLARIMETRY

2.1. Literature Review

Full Polarimetry (or Full-POL) is a way to obtain the Matrix scattering of a target in its most complete form, using the alternating transmission of a linearly polarized wave on the horizontal and then at the vertical, next receiving at the antennas the reflected signal polarized horizontally and vertically. With this method, it is possible to get HH, HV, VH and VV images, where the first letter indicates the transmitted signal and the second, the received signals.

Although this mode of transmission is the most complete, in relation to the polarimetric characteristics of the targets, and extensive tooling has been developed for extracting information from its images (polarimetric response, nature of reflectors, etc.), SAR systems with Full-POL are very complex and expensive. Thus, it is common to have systems with partial polarizations such as (HH, HV) or (VH, VV). A simple example could be the mission TerraSAR-X (TSX) [16], wherein the SAR satellite sensor operates in mode Scan SAR only with single polarization (HH ou VV) or with cross-polarization (VH).

The concept of CP has emerged as the middle ground between SAR system of Full-POL and SAR systems with Partial Polarization.

The original model of Souyris foresaw a transmission using a polarization different from the usual horizontal and vertical, taking as an example an oriented wave of $\pi/4$ [6]. Two years later, Stacy and Preiss proposed the so-called Dual-Circular mode in which the wave would be transmitted and received using circular polarization [42]. In 2009, Raney proposed the Hybrid-POL in which the transmission is realized with the use of the circular transmission to the right or the left, with the signal received by linear polarization, horizontal and vertical [12], [43]. In 2009, Nord introduced an alteration on the Souyris algorithm in order to consider the double-bounce scattering properties [7].

In the following years, several doctoral Thesis turned their attention to this theme in based on function of the increasing interest on the technique for application in Earth observation of space systems.

Exemplifying some of these works, in 2010, Marco Lavalle (University of Rennes, France) proposed a theoretical formulation for a CP algorithm from Full-POL images acquired by the Airborne SAR System of DLR. The pseudo reconstruction was applied in an interferometric scenario to investigate the potential of CP in applications related to the remote sensing of forest. The results showed the effectiveness of CP for certain combinations of soil volume and surface area [8].

In 2011, Rajib Kumar Panigrahi (Indian Institute of Technology in Guwahati) proposed an algorithm eliminating the effects of secondary lobes and reducing the width of the main lobe in a CP transmission. Full-POL data from AirSAR was used to perform a pseudo-reconstruction of the CP image [9].

In the same year, My-Linh Truong-Loi (University of Rennes, France) studied the potential application of a SAR system of low frequency operating in several scenarios. The CP analysis was performed from the Full-POL images acquired from the RAMSES / ONERA, SETHI, AirSAR and PALSAR Airborne [10].

In 2012, Reza Shirvany investigated in detail the statistical properties of Dual-POL SAR data using data acquired by the RADARSAT-2, AirSAR, and UAVSAR systems, covering, for example, urban land, vegetation and maritime surveillance [44].

Two years later, Michael Denbina [12] conducted researches to explore the viability of the CP SAR comparing with the traditional linear Dual-POL for iceberg detection and ice on the sea scenarios. As Lavalle [8], Denbina employed pseudo algorithms to simulate CP from RADARSAT-2 images. The objective of this study was to evaluate the expected performance for the detection of targets through the RCM [12].

In 2015, Rafael Lemos Paes [45] emulated new CP architectures from Full-POL data to evaluate the technique of detection of metallic targets at sea. Paes has employed both Single-POL and Dual-POL images from the Cosmo-Skymed Mission and Dual-POL images from the TerraSAR-X mission. Experimental results have shown that CP Hybrid-POL mode parameters can distinguish targets in the ocean only with the use of a global threshold technique.

This brief bibliographic research does not exhaust all the studies done in the CP area. However, it shows that previous PhD Theses have used pseudo reconstructions from Full-POL data, due to the absence of CP in most space SAR systems. These works also considered the use of the Reciprocity Theorem to be described in Section 2.3, due to the possibility of simplification involving the transmission and reception of the signals in the studied scenarios.

The use of compact polarimetry is not yet unanimous in the scientific world. The technique allows reconstructing a pseudo Full-POL image from a simplified system. Then, the CP system may provide products with lower quality than the desired results. However, observing a tendency of mass reduction and simplification of space systems, the CP could be an alternative to the high potential of application in the future.

2.2. Polarimetric Model

Consider the instantaneous electric field E(*z*, *t*) of the plane electromagnetic wave, transmitted by a SAR system that propagates on the *z* axis, represented by their horizontal (*h*) and vertical components (*v*) [46], [47]

$$\vec{E}\left(z\right)=E_h(z)\vec{e}_h+E_v(z)\vec{e}_v\,, \tag{2.1}$$

where $\vec{e}_h$ e $\vec{e}_v$ are unit vectors in the direction *h* and *v*, respectively, and the electric field components are represented by

$$E_h\left(z\right)=E_h\exp\left(-jk_0z\right), \tag{2.2}$$

$$E_v\left(z\right)=E_v\exp\left(-jk_0\vec{z}\right), \tag{2.3}$$

where k_0 is the wave number expressed as $k_0=\omega\sqrt{\mu\varepsilon'}$, for a magnetic permeability μ, electric permissivity ε' and angular frequency ω.

$$E_h=E_{0h}\exp\left\{-j\delta_h\right\}, \tag{2.4}$$

$$E_v=E_{0v}\exp\left\{-j\delta_v\right\}, \tag{2.5}$$

δ_h and δ_v are phase angles and E_{0h} and E_{0v} amplitudes of E_h and E_v, respectively. The instantaneous values of $E_h(z)$ and $E_v(z)$ are given by

$$e_h=E_h\left(z,t\right)=\Re\left\{E_h\left(z\right)\exp\left(j\omega_0t\right)\right\}=E_{0h}\cos\left(\omega_0t-k_0z-\delta_h\right), \tag{2.6}$$

$$e_v=E_v\left(z,t\right)=\Re\left\{E_v\left(z\right)\exp\left(j\omega_0t\right)\right\}=E_{0v}\cos\left(\omega_0t-k_0z-\delta_v\right), \tag{2.7}$$

where $\Re$ is the real part of the complex quantity and e_h, e_v represents a compact notation of $E_h\left(z,t\right)$, $E_v\left(z,t\right)$, respectively.

Considering $E_{0h} \neq 0$ and $E_{0v} \neq 0$, we have the electromagnetic wave polarization ellipse represented by

$$\left(\frac{e_h}{E_{0h}}\right)^2 + \left(\frac{e_v}{E_{0v}}\right)^2 - 2\left(\frac{e_h}{E_{0h}}\right)\left(\frac{e_v}{E_{0v}}\right)\cos(\delta) = \text{sen}^2(\delta), \text{ para } \delta = \delta_h - \delta_v, \qquad (2.8)$$

and illustrated in the Figure 2.3. The angle χ_p is the ellipticity angle, ranging between $-\pi/4$ and $\pi/4$; the angle ψ_p is the inclination angle, ranging between $-\pi/2$ and $\pi/2$; I_0 is intensity parameter; ϕ I is the auxiliary angle; and e_v is the direction of propagation [47].

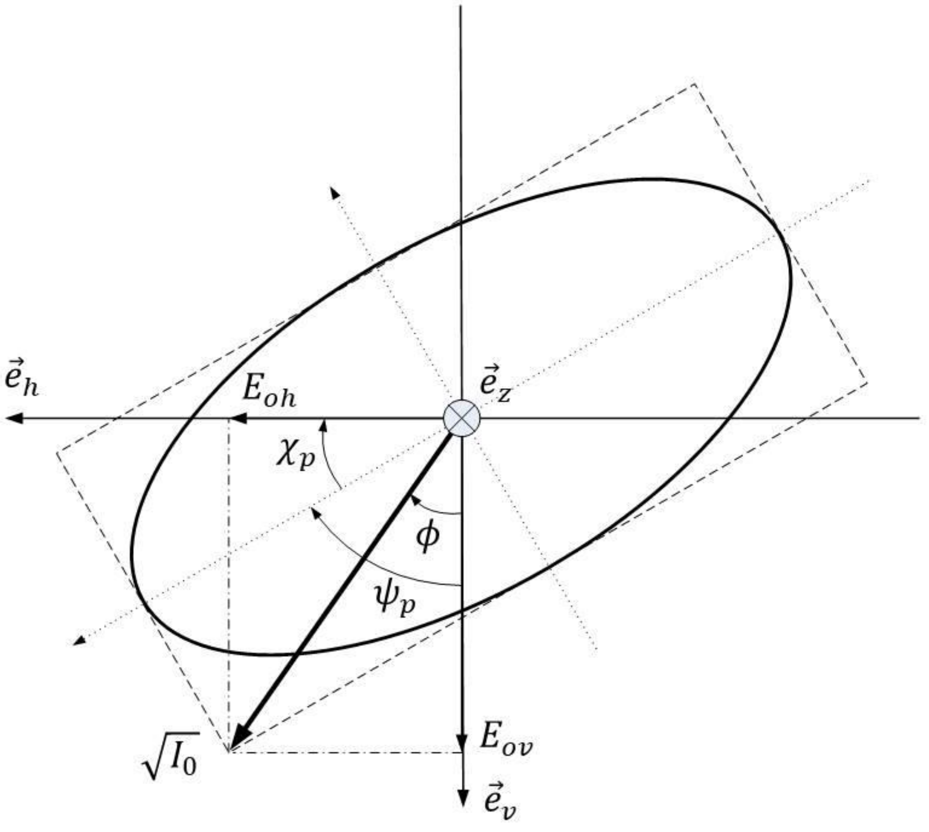

Figure 2.3 – Polarization Ellipse.

Observing the geometry in Figure 2.3, the following relations can be established

$$\text{tg}\phi = \frac{E_{0h}}{E_{0v}} \Rightarrow \phi = \text{tg}^{-1}\left(\frac{E_{0h}}{E_{0v}}\right), \text{ and} \qquad (2.9)$$

$$I_0 = E_{0h}^2 + E_{0v}^2. \qquad (2.10)$$

The polarization states of a wave vary according to the values of amplitude E_{0h} and E_{0v}, respectively; to the wave phase angle δ; to the ellipticity angle χ_p; to the inclination angle ψ_p. Table 2.1 summarizes some examples of linear and circular polarization states.

Table 2.1 – Examples of Linear and Circular Polarization States.

State	E_{0h}	E_{0v}	δ	χ_p	ψ_p
Horizontal Linear	1	0	0	0	$\pm\pi/2$
Linear Vertical	0	1	0	0	0
Linear Diagonal	$1/\sqrt{2}$	$1/\sqrt{2}$	$0,\pi$	0	$\pm\pi/4$
Circular to the left	$1/\sqrt{2}$	$1/\sqrt{2}$	$\pi/2$	$\pi/4$	$-\frac{\pi}{2}$ a $\frac{\pi}{2}$
Circular to the right	$1/\sqrt{2}$	$1/\sqrt{2}$	$-\pi/2$	$-\pi/4$	$-\frac{\pi}{2}$ a $\frac{\pi}{2}$

For the case of the last example shown in Table 2.1, circular polarization to the right, replacing the values presented in expression (2.8), we arrive at expressions (2.11) and (2.12), illustrated by Figure 2.4 [48].

$$\left(\frac{e_h}{E_{0h}}\right)^2+\left(\frac{e_v}{E_{0v}}\right)^2=1 \tag{2.11}$$

$$E_{0v}=E_{0h}=1/\sqrt{2}\,. \tag{2.12}$$

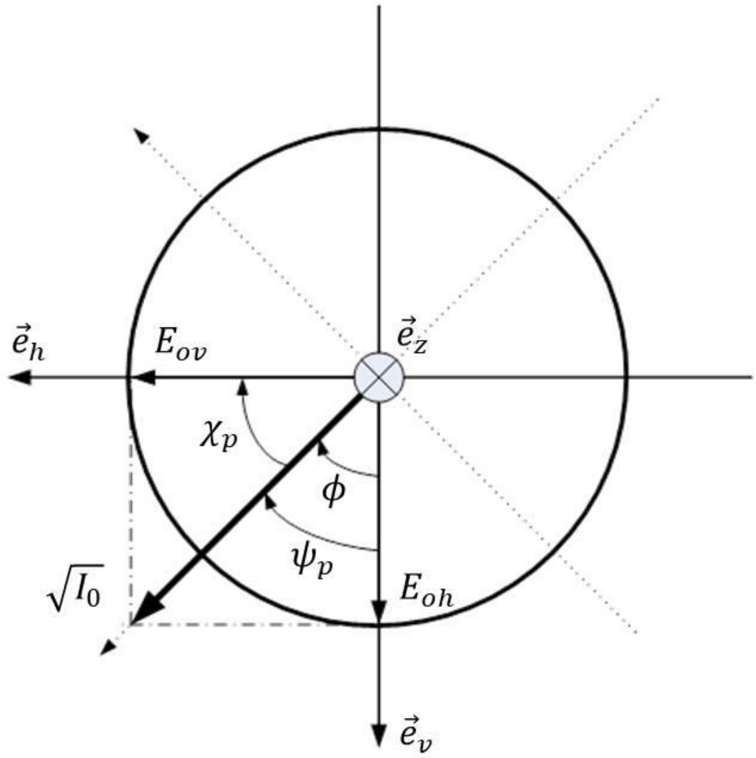

Figure 2.4 – Circular Polarizations Elements.

Considering the polarization of the wave by the Stokes theory, we have

$$\vec{J}=\begin{bmatrix} S_1 \\ S_2 \\ S_3 \\ S_4 \end{bmatrix}=\begin{bmatrix} \left|E_{0v}\right|^2+\left|E_{0h}\right|^2 \\ \left|E_{0v}\right|^2-\left|E_{0h}\right|^2 \\ 2\Re\left\{E_{0v}E_{0h}^*\right\} \\ 2\Im\left\{E_{0v}E_{0h}^*\right\} \end{bmatrix}=\begin{bmatrix} \left|E_{0v}\right|^2+\left|E_{0h}\right|^2 \\ \left|E_{0v}\right|^2-\left|E_{0h}\right|^2 \\ 2E_{0v}E_{0h}^*\cos\left(\delta\right) \\ 2E_{0v}E_{0h}^*\sin\left(\delta\right) \end{bmatrix}=\begin{bmatrix} I_0 \\ I_0\cos 2\psi_p\cos 2\chi_p \\ I_0\sin 2\psi_p\cos 2\chi_p \\ I_0\sin 2\psi_p \end{bmatrix}, \qquad (2.13)$$

where $\Im$ is the imaginary part of the complex quantity and the follow relations are observed between the independent parameters S_1, S_2, S_3 and S_4, denominated as Stokes parameters, where

$$S_1^2=S_2^2+S_3^2+S_4^2\text{, and} \qquad (2.14)$$

$$p=\frac{\sqrt{S_2^2+S_3^2+S_4^2}}{I_0}\,. \qquad (2.15)$$

The expression (2.15) is defined as a wave polarization degree. Where $p=0$, there is not a correlation between E_{0h} and E_{0v} and the waves are defined as completely depolarized. For $p=1$, the correlation between E_{0h} and E_{0v} is maximum and the waves are defined as completely polarized [38].

The models described above, using the polarization ellipse, are suitable for graphical verification of the electromagnetic wave. However, for implementation in computational processes, the wave polarization can be represented by means of a two-dimensional complex vector [46]. Therefore, the set of expressions (2.6) and (2.7) can be represented together by the Jones vector $\vec{E}_{hv}$

$$\vec{E}_{hv}=\begin{bmatrix} E_h\left(z,t\right) \\ E_v\left(z,t\right) \end{bmatrix}=\begin{bmatrix} E_{0h}\cos\left(\omega t-k_0 z-\delta_h\right) \\ E_{0v}\cos\left(\omega t-k_0 z-\delta_v\right) \end{bmatrix}. \tag{2.16}$$

Table 2.2 presents some Jones unit vectors used in usual cases of polarizations.

Table 2.2 – Jones unitary vectors for usual polarizations.

	Linear H	Linear V	Circular to the right	Circular to the left
$\vec{J}$	$\begin{bmatrix}1\\0\end{bmatrix}$	$\begin{bmatrix}0\\1\end{bmatrix}$	$\frac{1}{\sqrt{2}}\begin{bmatrix}1\\-j\end{bmatrix}$	$\frac{1}{\sqrt{2}}\begin{bmatrix}1\\j\end{bmatrix}$

Observing the basic concepts of Electromagnetic Theory and the scattering process that occurs when the wave transmitted by the SAR reaches the target [38], we can establish the following relationship between the Jones vector of the incident wave $\vec{E}_{hv}^{i}$ and the scattered wave $\vec{E}_{hv}^{s}$

$$\vec{E}_{hv}^{s} = \frac{\exp\{-j\omega_c/c_0\}}{R} S\,\vec{E}_{hv}^{i}, \tag{2.17}$$

where ω_c is the carrier frequency in radians, c_0 is the speed of light and R is the distance between the SAR sensor and the target. The term $\exp\{-j\omega_c/c_0\}/R$ in expression (2.17) means that we take in account the effects of propagation in amplitude and phase [46]. S is called the Sinclair matrix, or Scattering matrix, is expressed by

$$S = \begin{bmatrix} S_{HH} & S_{HV} \\ S_{VH} & S_{VV} \end{bmatrix}, \tag{2.18}$$

where the coefficients of $S_{i,j}$ are defined by i for the transmitted polarization and j for received polarization.

The four elements that constitute the Sinclair matrix represent four distinct characteristics associated with the polarization states of the incident electromagnetic wave and the receiving antenna. The element S_{HH} indicates that the transmission was carried out with horizontal polarization and the reception occurred with the electromagnetic wave also polarized horizontally. In the sequence, the element S_{HV} indicates that the transmission was carried out with horizontal polarization and the reception occurred with the vertical polarized electromagnetic wave. Elements that have polarization states of the shape $i = j$ are called linear polarization or co-polarized (Co-POL). If $i \neq j$, the elements are called cross-polarization (Cross-POL).

From these concepts, as a complete SAR system (Full-POL) is defined as the one formed with four channels, where the readings data are stored in HH, HV, VH, and VV. This architecture allows four degrees of freedom in terms of possibilities of use of polarimetric resources. However, it presents a high cost in terms of transmitted average power, half the bandwidth and the limitation of the possibilities of angles of incidence of the satellite transmission that allow the formation of an image suitable for processing and analysis [13], [34], [46].

Based on expression (2.17), the measurement of the electric field $\vec{E}_{hv}^{s}$ for a given polarization in transmission and reception can be expressed by

$$\vec{E}_{hv}^{s} = k_r \vec{J}_r^T S \, \vec{J}_t \ , \tag{2.19}$$

where k_r is a complex constant, $\vec{J}_r^T$ represents the Jones vector associated to the reception; $(\,\cdot\,)^T$ denotes that the matrix is transposed; and $\vec{J}_t$ represents the Jones vector associated to the transmission [34]. The basic form of these vectors is described in Table 2.

The Sinclair matrix (2.18) also can be can also be described in vector notation, using the Scattering $\vec{k}$, being expressed by

$$\vec{k} = \begin{bmatrix} S_{HH} & S_{HV} & S_{VH} & S_{VV} \end{bmatrix}^T . \tag{2.20}$$

As coherent targets are those that generate full polarization waves when illuminated by waves with the same characteristics, a scattering matrix *S*, or vector $\vec{k}$, would be sufficient to describe their deterministic behaviors. However, most of the targets found in nature produce non-coherent (or incoherent) scatter, depending on the temporal and/or spatial variations to which the incident electromagnetic waves are subjected [36].

Another relevant consideration is the size of the resolution cell. In most radar systems, the resolution element is larger than the wavelength used by the system. In other words, in the dimension of a single cell, several deterministic scatters are found, which makes the matrix *S* a small resource of representation of the illuminated area [49].

This limitation of statistical representation can be overcome through the use of second-order matrices, called Coherence matrices *T* and Covariance matrices *C*. Both have similar properties, being Hermitian, positive, semi-defined, which leads to real and not negative eigenvalues. However, since the Covariance matrix is more widely used in the radar backscatter analysis, it will be the object of the mathematical modeling developed in this work [50].

The Covariance matrix is calculated from the mean of the complex product between the scattering vector $\vec{k}$ (2.20), and its transposed conjugate, given by

$$C^{Full-POL} = \left\langle \vec{k} \cdot \vec{k}^{H} \right\rangle, \tag{2.21}$$

where the notation $\langle \cdot \rangle$ indicates the spatial media and the notation $(\ )^{H}$ means the transposed and complex conjugate (Hermitian operator).

Considering the scattering vector presented at the expression (2.20), we have a Covariance matrix 4×4, given by

$$C^{Full-POL(4\times4)} = \left\langle \begin{bmatrix} S_{HH} & S_{HV} & S_{VH} & S_{VV} \end{bmatrix} \cdot \begin{bmatrix} S_{HH} & S_{HV} & S_{VH} & S_{VV} \end{bmatrix}^{H} \right\rangle, \tag{2.22}$$

$$C^{Full-POL(4\times4)} = \begin{bmatrix} \left\langle |S_{HH}|^{2} \right\rangle & \left\langle S_{HH} S_{HV}^{*} \right\rangle & \left\langle S_{HH} S_{VH}^{*} \right\rangle & \left\langle S_{HH} S_{VV}^{*} \right\rangle \\ \left\langle S_{HV} S_{HH}^{*} \right\rangle & \left\langle |S_{HV}|^{2} \right\rangle & \left\langle S_{HV} S_{VH}^{*} \right\rangle & \left\langle S_{HV} S_{VV}^{*} \right\rangle \\ \left\langle S_{VH} S_{HH}^{*} \right\rangle & \left\langle S_{VH} S_{HV}^{*} \right\rangle & \left\langle |S_{VH}|^{2} \right\rangle & \left\langle S_{VH} S_{VV}^{*} \right\rangle \\ \left\langle S_{VV} S_{HH}^{*} \right\rangle & \left\langle S_{VV} S_{HV}^{*} \right\rangle & \left\langle S_{VV} S_{VH}^{*} \right\rangle & \left\langle |S_{VV}|^{2} \right\rangle \end{bmatrix}. \tag{2.23}$$

2.3. Reciprocity Theorem

Based on the property of symmetry of several and frequent mechanisms of reflection, the Reciprocity Theorem [36] was established, which establishes as a premise that $S_{HV} = S_{VH}$, which allows the Scattering matrix S to be written in the form of three complex elements, such as

$$S = \begin{bmatrix} S_{HH} & S_{HV} \\ S_{HV} & S_{VV} \end{bmatrix}. \tag{2.24}$$

As a result, the Scattering vector $\vec{k}$, represented in (2.20), can be defined as [38], [40]

$$\vec{k} = \begin{bmatrix} S_{HH} & \sqrt{2}\, S_{HV} & S_{VV} \end{bmatrix}^T , \tag{2.25}$$

where the insertion of the factor $\sqrt{2}$ and 2 in (2.25) and in the following expressions has the purpose of maintaining the total scattering power (or the invariance of the span) at the same levels of employment as the Sinclair matrix (2.18), whose four elements are complete [12], [34].

Due to this simplification, the Covariance matrix presented in (2.23) is reduced to a matrix 3×3, in the form

$$C^{Full-POL(3\times 3)} = \begin{bmatrix} \left\langle |S_{HH}|^2 \right\rangle & \sqrt{2}\left\langle S_{HH}S_{HV}^* \right\rangle & \left\langle S_{HH}S_{VV}^* \right\rangle \\ \sqrt{2}\left\langle S_{HV}S_{HH}^* \right\rangle & 2\left\langle |S_{HV}|^2 \right\rangle & \sqrt{2}\left\langle S_{HV}S_{VV}^* \right\rangle \\ \left\langle S_{VV}S_{HH}^* \right\rangle & \sqrt{2}\left\langle S_{VV}S_{HV}^* \right\rangle & \left\langle |S_{VV}|^2 \right\rangle \end{bmatrix}. \tag{2.26}$$

In practical terms, the Reciprocity Theorem can be applied to monostatic systems, or when the medium between the target and the antenna of the system is reciprocal, in other words, it does not cause changes in the behavior of the electromagnetic wave that runs through it [5], [39].

However, an important exception to the application of this theorem must be considered when the wave travels through regions of the ionosphere where the presence of anisotropic plasma generates significant changes in propagation through the effect called Faraday rotation [40, Sec. 1.4.1], whose description is in Appendix B.

In order to simplify the development of the CP_{az} algorithm, we consider the use of the Reciprocity Theorem every time in this work, except with the implementation of the *M* matrix, presented in expression (B.19).

2.4. Hybrid Polarimety

This Thesis considers the Hybrid-POL mode (Right Circular Polarization on transmission (*Rhc*) and linear polarization on receive), having in mind that the circular polarizations reduce, but not remove completely due to the effects of Ionosphere over wave propagation rotation. Is this case, the transmitted signal has a phase delay. However, the echo signals polarized in H e V suffer the effects of Faraday rotation [34], [51], [52].

Considering a wave transmitted circularly to the right and the reception of the echo signal made simultaneously by antennas with horizontal and vertical polarization, the Jones vector for the right circular polarization, shown in Table 2.2, and assuming the Theorem of Reciprocity, the scattering vector $\vec{k}_{Rhc}$ is defined as [38], [40]

$$\vec{k}_{Rhc} = \frac{1}{\sqrt{2}}\begin{bmatrix} S_{HH} & S_{HV} \\ S_{HV} & S_{VV} \end{bmatrix}\begin{bmatrix} 1 \\ -j \end{bmatrix} = \frac{1}{\sqrt{2}}\begin{bmatrix} S_{RH} \\ S_{RV} \end{bmatrix}, \tag{2.27}$$

with

$$\begin{aligned} S_{RH} &= S_{HH} - jS_{HV}, \\ S_{RV} &= S_{HV} - jS_{VV}, \end{aligned} \tag{2.28}$$

where S_{RH} represents the right circular transmission and linear horizontal reception and S_{RV} represents the right circular transmission and linear vertical reception.

It may be noted by (2.27) that if we have the components S_{HH}, S_{HV}, and S_{VV} from the Scattering matrix *S* of a Full-POL SAR system, it is possible to generate the components S_{RH}, and S_{RV} of the SAR CP system. It is emphasized, however, that in the case of a SAR CP system, with only the components S_{RH} and S_{RV}, it would not be possible to obtain the components S_{HH}, S_{HV}, and S_{VV}.

The Covariance matrix relative to the Scattering vector $\vec{k}_{Rhc}$ turns

$$C_{Rhc} = \left\langle \vec{k}_{Rhc} \vec{k}_{Rhc}^{H} \right\rangle = \left\langle \begin{bmatrix} S_{RH} & S_{RV} \end{bmatrix} \cdot \begin{bmatrix} S_{RH} & S_{RV} \end{bmatrix}^{H} \right\rangle. \tag{2.29}$$

Expanding (2.29)

$$C_{Rhc} = \begin{bmatrix} C_{cp11} & C_{cp12} \\ C_{cp21} & C_{cp22} \end{bmatrix} = \begin{bmatrix} \left\langle |S_{RH}|^2 \right\rangle & \left\langle S_{RH} S_{RV}^{*} \right\rangle \\ \left\langle S_{RV} S_{RH}^{*} \right\rangle & \left\langle |S_{RV}|^2 \right\rangle \end{bmatrix} \tag{2.30}$$

$$C_{Rhc} = \begin{bmatrix} \left\langle \left(S_{HH} - jS_{HV}\right)\left(S_{HH}^{*} + jS_{HV}^{*}\right) \right\rangle & \left\langle \left(S_{HH} - jS_{HV}\right)\left(S_{HV}^{*} + jS_{VV}^{*}\right) \right\rangle \\ \left\langle \left(S_{HV} - jS_{VV}\right)\left(S_{HH}^{*} + jS_{HV}^{*}\right) \right\rangle & \left\langle \left(S_{HV} - jS_{VV}\right)\left(S_{HV}^{*} + jS_{VV}^{*}\right) \right\rangle \end{bmatrix} \tag{2.31}$$

$$C_{Rhc} = \begin{bmatrix} \left\langle |S_{HH}|^2 \right\rangle + \left\langle |S_{HV}|^2 \right\rangle & \left\langle S_{HH} S_{HV}^{*} \right\rangle + \left\langle S_{HV} S_{VV}^{*} \right\rangle \\ \quad + \left\langle jS_{HH} S_{HV}^{*} \right\rangle - \left\langle jS_{HV} S_{HH}^{*} \right\rangle & \quad + \left\langle jS_{HH} S_{VV}^{*} \right\rangle - \left\langle j|S_{HV}|^2 \right\rangle \\ \left\langle S_{HV} S_{HH}^{*} \right\rangle + \left\langle S_{VV} S_{HV}^{*} \right\rangle & \left\langle |S_{HV}|^2 \right\rangle + \left\langle |S_{VV}|^2 \right\rangle \\ \quad - \left\langle jS_{VV} S_{HH}^{*} \right\rangle + \left\langle j|S_{HV}|^2 \right\rangle & \quad + \left\langle jS_{HV} S_{VV}^{*} \right\rangle - \left\langle jS_{VV} S_{HV}^{*} \right\rangle \end{bmatrix}. \tag{2.32}$$

This resulting matrix can be rearranged into a sum of three matrices, where in the first only the co-POL terms (HH and VV) are arranged; in the second, only the terms with cross-POL (HV and VH); and, at the last, the residual terms [7], [33] as follow

$$C_{Rhc} = C_{co-POL} + C_{cr-POL} + C_{res} \tag{2.33}$$

$$C_{co-POL} = \frac{1}{2}\begin{bmatrix} \left\langle |S_{HH}|^2 \right\rangle & \left\langle jS_{HH}S_{VV}^* \right\rangle \\ \left\langle -jS_{VV}S_{HH}^* \right\rangle & \left\langle |S_{VV}|^2 \right\rangle \end{bmatrix} \tag{2.34}$$

$$C_{cr-POL} = \frac{1}{2}\begin{bmatrix} \left\langle |S_{HV}|^2 \right\rangle & -\left\langle jS_{HV}S_{HV}^* \right\rangle \\ \left\langle j|S_{HV}|^2 \right\rangle & \left\langle |S_{HV}|^2 \right\rangle \end{bmatrix} = \frac{1}{2}\begin{bmatrix} \left\langle |S_{HV}|^2 \right\rangle & -\left\langle j|S_{HV}|^2 \right\rangle \\ \left\langle j|S_{HV}|^2 \right\rangle & \left\langle |S_{HV}|^2 \right\rangle \end{bmatrix} \tag{2.35}$$

$$C_{res} = \frac{1}{2}\begin{bmatrix} \left\langle -2\Im\left(S_{HH}S_{HV}^*\right) \right\rangle & \left\langle S_{HH}S_{HV}^* + S_{HV}S_{VV}^* \right\rangle \\ \left\langle S_{HV}S_{HH}^* + S_{VV}S_{HV}^* \right\rangle & \left\langle 2\Im\left(S_{VV}S_{HV}^*\right) \right\rangle \end{bmatrix}, \tag{2.36}$$

where $\Im$ represents the imaginary part of the complex quantity.

Taking into account that with the use of Compact Polarization only the components S_{RH} and S_{RV} are measurable and that the components S_{HH}, S_{HV}, and S_{VV} are unknown, in the expressions from (2.34) to (2.36) three unknown real terms are observed

$$\left\langle |S_{HH}|^2 \right\rangle, \left\langle |S_{HV}|^2 \right\rangle, \text{ and } \left\langle |S_{VV}|^2 \right\rangle, \tag{2.37}$$

and six complex terms also unknown

$$\left\langle S_{HH}S_{VV}^* \right\rangle, \left\langle S_{VV}S_{HH}^* \right\rangle, \left\langle S_{HH}S_{HV}^* \right\rangle, \left\langle S_{HV}S_{VV}^* \right\rangle, \left\langle S_{HV}S_{HH}^* \right\rangle \text{ and } \left\langle S_{VV}S_{HV}^* \right\rangle. \tag{2.38}$$

The term C_{Rhc} (2.33) is calculable and therefore known, but the terms C_{co-POL}, C_{cr-POL} and C_{res} are unknown.

One of the great challenges of signal processing of SAR CP data is estimating in whole or in part the Covariance matrix $C^{Full-POL(3\times3)}$ or $C^{Full-POL(4\times4)}$ for the case when the Reciprocity Theorem is not considered. Also, you can use the extensive tool developed for Full-POL SAR systems, which use, as the basis, the Covariance matrix.

3. RECONSTRUCTION METHODS

3.1. Souyris Method

The partial reconstruction model of the Covariance matrix from Full-POL SAR system proposed by Souyris [6] considers the case in which the illuminated scenario has reflection symmetry [5] with relation to the incident plane. This model is suitable for regions where there is volumetric scattering, such forest canopy, among others [33], [53]. In the case of reflection symmetry hypothesis, there is a complete no correlation between the co-POL and cross-POL scattering coefficients, which implies [5]

$$\begin{aligned}\left\langle S_{HH}S_{HV}^{*}\right\rangle = \left\langle S_{HV}S_{HH}^{*}\right\rangle = \left\langle S_{VV}S_{VH}^{*}\right\rangle = \left\langle S_{VH}S_{VV}^{*}\right\rangle = 0\\ \left\langle S_{HH}S_{VH}^{*}\right\rangle = \left\langle S_{VH}S_{HH}^{*}\right\rangle = \left\langle S_{VV}S_{HV}^{*}\right\rangle = \left\langle S_{HV}S_{VV}^{*}\right\rangle = 0.\end{aligned} \tag{3.39}$$

In this way, the matrix (2.36) cancels out, and the indeterminations presented in (2.37) and (2.38) are reduced to the four terms $\left\langle |S_{HH}|^2\right\rangle, \left\langle |S_{VV}|^2\right\rangle, \left\langle S_{HH}S_{VV}^{*}\right\rangle$, and $\left\langle |S_{HV}|^2\right\rangle$

$$C_{Rhc} = \frac{1}{2}\left(\begin{bmatrix} \left\langle |S_{HH}|^2\right\rangle & j\left\langle S_{HH}S_{VV}^{*}\right\rangle \\ -j\left\langle S_{VV}S_{HH}^{*}\right\rangle & \left\langle |S_{VV}|^2\right\rangle \end{bmatrix} + \left\langle |S_{HV}|^2\right\rangle \begin{bmatrix} 1 & -j \\ j & 1 \end{bmatrix}\right). \tag{3.40}$$

In order to reduce the indeterminations presented in (2.37), Souyris proposed a method of interpolation of the state of polarization of the electromagnetic waves, assuming that this proposal can be extended to any state of polarization [6].

In this process, a relationship between S_{HH}, S_{HV}, and S_{VV} is established based on the scattering of fully polarized waves and completely depolarized waves.

In the first case, the scattering of the cross-POL energy is very small, while the co-POL components are almost perfectly correlated

$$\left\langle |S_{HV}|^2 \right\rangle \approx 0 \tag{3.41}$$

$$\rho_{HH-VV} = \frac{\left\langle S_{HH} S_{VV}^* \right\rangle}{\sqrt{\left\langle S_{HH} S_{HH}^* \right\rangle \left\langle S_{VV} S_{VV}^* \right\rangle}} \approx 1, \tag{3.42}$$

where ρ_{HH-VV} is the complex correlation or degree / magnitude of coherence between S_{HH} and S_{VV} [36].

For completely depolarized scattered waves, the average power arriving at the radar receiver does not depend on the state of polarization. In this situation, the correlation between the co-POL channels practically cancels out and the scattered energy intensity is practically the same between S_{HH} , $\sqrt{2}S_{HV}$, and S_{VV} . So

$$\left\langle |S_{HH}|^2 \right\rangle \approx \left\langle |S_{VV}|^2 \right\rangle \approx 2\left\langle |S_{HV}|^2 \right\rangle \tag{3.43}$$

$$\rho_{HH-VV} = \frac{\left\langle S_{HH} S_{VV}^* \right\rangle}{\sqrt{\left\langle S_{HH} S_{HH}^* \right\rangle \left\langle S_{VV} S_{VV}^* \right\rangle}} \approx 0 \ . \tag{3.44}$$

The expression (3.43) can be rewritten as

$$\left\langle |S_{HV}|^2 \right\rangle \cong \frac{\left\langle |S_{HH}|^2 \right\rangle + \left\langle |S_{VV}|^2 \right\rangle}{4} . \tag{3.45}$$

Considering these two cases, considered limits of the physical interpretation of the scattering mechanism, Souyris proposed an interpolation of the state of polarization, as shown in Figure 3.5.

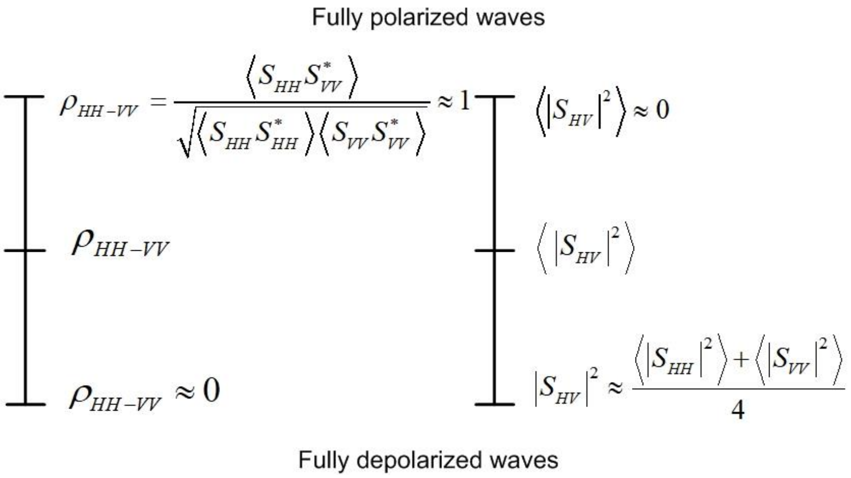

Figure 3.5 – Souyris linear interpolation of the state of polarization.

Comparing the two states, we have

$$\begin{aligned}
&\frac{\rho_{HH-VV}-0}{\left\langle |S_{HV}|^2\right\rangle - \frac{\left\langle |S_{HH}|^2\right\rangle + \left\langle |S_{VV}|^2\right\rangle}{4}} = \frac{1-0}{0-\frac{\left\langle |S_{HH}|^2\right\rangle + \left\langle |S_{VV}|^2\right\rangle}{4}} \\
&\Rightarrow -\rho_{HH-VV}\left(\frac{\left\langle |S_{HH}|^2\right\rangle + \left\langle |S_{VV}|^2\right\rangle}{4}\right) = \left\langle |S_{HV}|^2\right\rangle - \frac{\left\langle |S_{HH}|^2\right\rangle + \left\langle |S_{VV}|^2\right\rangle}{4} \\
&\Rightarrow \quad \left\langle |S_{HV}|^2\right\rangle = \frac{\left\langle |S_{HH}|^2\right\rangle + \left\langle |S_{VV}|^2\right\rangle}{4} - \rho_{HH-VV}\left(\frac{\left\langle |S_{HH}|^2\right\rangle + \left\langle |S_{VV}|^2\right\rangle}{4}\right) \\
&\Rightarrow \quad \left\langle |S_{HV}|^2\right\rangle = \left(1-\rho_{HH-VV}\right)\left(\frac{\left\langle |S_{HH}|^2\right\rangle + \left\langle |S_{VV}|^2\right\rangle}{4}\right).
\end{aligned} \tag{3.46}$$

Coming to the model that relates the ratio between the intensity of the cross-POL components and the mean intensity of the co-POL components with the magnitude of the coherence of the co-POL components

$$\frac{\left\langle |S_{HV}|^2\right\rangle}{\left\langle |S_{HH}|^2\right\rangle + \left\langle |S_{VV}|^2\right\rangle} = \frac{\left(1-\rho_{HH-VV}\right)}{4}. \tag{3.47}$$

The expression (3.47) is the second hypothesis assumed by Souyris. The first being the reflection symmetry presented in (3.40).

By combining (3.40), (3.41), and (3.47), a linear system of four equations, with four unknown elements, was solved numerically through an iterative process, described below.

At first, from (3.40) we define

$$\begin{aligned} 2C_{cp11} &= \left\langle \left|S_{HH}\right|^2 \right\rangle + \left\langle \left|S_{HV}\right|^2 \right\rangle \\ 2C_{cp12} &= j\left\langle S_{HH}S_{VV}^* \right\rangle - j\left\langle \left|S_{HV}\right|^2 \right\rangle \\ 2C_{cp21} &= -j\left\langle S_{VV}S_{HH}^* \right\rangle + j\left\langle \left|S_{HV}\right|^2 \right\rangle \\ 2C_{cp22} &= \left\langle \left|S_{VV}\right|^2 \right\rangle + \left\langle \left|S_{HV}\right|^2 \right\rangle . \end{aligned} \tag{3.48}$$

From (3.48) into (3.43), the degree of coherence between S_{HH} and S_{VV} is express by

$$\rho_{HH-VV} = \frac{-2jC_{cp12} + X_{sr}}{\sqrt{\left(2C_{cp11} - X_{sr}\right)\cdot\left(2C_{cp22} - X_{sr}\right)}}, \tag{3.49}$$

where $X_{sr} = \left\langle \left|S_{HV}\right|^2 \right\rangle$.

From relation (3.47) into (3.48), we develop

$$\begin{aligned} X_{sr} &= \left(\left\langle \left|S_{HH}\right|^2 \right\rangle + \left\langle \left|S_{VV}\right|^2 \right\rangle \right) \frac{\left(1-\rho_{HH-VV}\right)}{4} \\ X_{sr} &= \left(2C_{cp11} + 2C_{cp22} - 2X_{sr}\right) \frac{\left(1-\rho_{HH-VV}\right)}{4} \\ 4X_{sr} &= 2C_{cp11} + 2C_{cp22} - 2X_{sr} - 2C_{cp11}\rho_{HH-VV} - 2C_{cp22}\rho_{HH-VV} + 2X_{sr}\rho_{HH-VV} \\ 6X_{sr} - 2X_{sr}\rho_{HH-VV} &= 2C_{cp11} + 2C_{cp22} - 2C_{11}\rho_{HH-VV} - 2C_{cp22}\rho_{HH-VV} \\ X_{sr}\left(3-\rho_{HH-VV}\right) &= \left(C_{cp11} + C_{cp22}\right)\left(1-\rho_{HH-VV}\right) \\ X_{sr} &= \left(C_{cp11} + C_{cp22}\right) \frac{\left(1-\rho_{HH-VV}\right)}{\left(3-\rho_{HH-VV}\right)}. \end{aligned} \tag{3.50}$$

For the reconstruction process, the iterations of the nonlinear system of equations are performed by steps. As implemented by Souyris [34], the cross-POL term is set to 0 at the initial step.

Step 1 - Initialization

$$\begin{aligned} X_{sr} &= 0 \\ \rho_{HH-VV}^{(0)} &= \frac{\left|-j2C_{cp12}\right|}{\sqrt{2C_{cp11}2C_{cp22}}}, \end{aligned} \tag{3.51}$$

Step 2 - Iteration

$$X_{sr}^{(n)} = \left(C_{cp11} + C_{cp22}\right)\frac{\left|\left(1-\rho_{HH-VV}\right)\right|}{\left|\left(3-\rho_{HH-VV}\right)\right|} \tag{3.52}$$

$$\rho_{HH-VV}^{(n)} = \frac{\left|-2jC_{cp12} + X_{sr}\right|}{\sqrt{\left(2C_{cp11} - X_{sr}\right)\cdot\left(2C_{cp22} - X_{sr}\right)}}, \tag{3.53}$$

where the value of ρ_{HH-VV} at (3.53) update the value of X_{sr} and *n* is the number of iterations.

Step 3 - Reconstruction

$$\begin{aligned} 2C_{cp11} &= \left\langle \left|S_{HH}\right|^2 \right\rangle + \left\langle \left|S_{HV}\right|^2 \right\rangle \quad \Rightarrow \quad \left\langle \left|S_{HH}\right|^2 \right\rangle = 2C_{cp11} - X_{sr} \\ 2C_{cp12} &= j\left\langle S_{HH}S_{VV}^{*} \right\rangle + \left\langle \left|S_{HV}\right|^2 \right\rangle \quad \Rightarrow \quad \left\langle S_{HH}S_{VV}^{*} \right\rangle = -j2C_{cp12} + X_{sr} \\ 2C_{cp22} &= \left\langle \left|S_{VV}\right|^2 \right\rangle + \left\langle \left|S_{HV}\right|^2 \right\rangle \quad \Rightarrow \quad \left\langle \left|S_{VV}\right|^2 \right\rangle = 2C_{cp22} - X_{sr}. \end{aligned} \tag{3.54}$$

Observing the hypothesis of Reflection Symmetry presented in (3.39), the Covariance matrix of the Full-POL mode (2.26) can be rewritten as showing in (3.55)

$$\begin{aligned} \left\langle S_{HH}S_{HV}^{*} \right\rangle = \left\langle S_{HV}S_{HH}^{*} \right\rangle = \left\langle S_{VV}S_{VH}^{*} \right\rangle = \left\langle S_{VH}S_{VV}^{*} \right\rangle = 0 \\ \left\langle S_{HH}S_{VH}^{*} \right\rangle = \left\langle S_{VH}S_{HH}^{*} \right\rangle = \left\langle S_{VV}S_{HV}^{*} \right\rangle = \left\langle S_{HV}S_{VV}^{*} \right\rangle = 0. \end{aligned}$$

$$C^{Full-POL(3\times3)}=\begin{bmatrix}\left\langle\left|S_{HH}\right|^2\right\rangle & \sqrt{2}\left\langle S_{HH}S_{HV}^*\right\rangle & \left\langle S_{HH}S_{VV}^*\right\rangle\\ \sqrt{2}\left\langle S_{HV}S_{HH}^*\right\rangle & 2\left\langle\left|S_{HV}\right|^2\right\rangle & \sqrt{2}\left\langle S_{HV}S_{VV}^*\right\rangle\\ \left\langle S_{VV}S_{HH}^*\right\rangle & \sqrt{2}\left\langle S_{VV}S_{HV}^*\right\rangle & \left\langle\left|S_{VV}\right|^2\right\rangle\end{bmatrix}$$

$$C^{Full-POL(3\times3)}=\begin{bmatrix}\left\langle\left|S_{HH}\right|^2\right\rangle & 0 & \left\langle S_{HH}S_{VV}^*\right\rangle\\ 0 & 2\left\langle\left|S_{HV}\right|^2\right\rangle & 0\\ \left\langle S_{VV}S_{HH}^*\right\rangle & 0 & \left\langle\left|S_{VV}\right|^2\right\rangle\end{bmatrix}. \tag{3.55}$$

Whose terms, by the process of pseudo reconstruction are replaced by those obtained in (3.54), as

$$C_{sr}^{CP(3\times3)}=\begin{bmatrix}2C_{cp11}-X_{sr} & 0 & -2jC_{cp12}+X_{sr}\\ 0 & 2\left\langle\left|S_{HV}\right|^2\right\rangle & 0\\ \left(-2jC_{cp12}+X_{sr}\right)^* & 0 & 2C_{cp22}-X_{sr}\end{bmatrix}. \tag{3.56}$$

The whole process is based on the acceptance of hypotheses and approximations. Notice that randomly picking some pixels $\rho_{HH-VV}^{(n)}$ (3.53) assume very high values in relation to others. Another fact is that the denominator can assume negative values in the square root of the denominator during the iteration. In both situations, in the calculation process, the following values are forced

$$\left|\rho_{HH-VV}^{(n)}\right|=1,\ \text{and}\ \left|X_{sr}^{(n)}\right|=0. \tag{3.57}$$

This issue is a subject of the Section 5.1 where the number of iterations will be discussed.

3.2. Nord Method

Once Souyris Method is suitable for regions where there is volumetric scattering, Nord et al. (from now on called just Nord) proposed a new approach for the algorithm, which was possible to take into account the double-bounce scattering [7].

The method considers the substitution of the value 4 in (3.47) for *N*

$$\begin{gathered}\frac{\left\langle \left|S_{HV}\right|^2 \right\rangle}{\left\langle \left|S_{HH}\right|^2 \right\rangle + \left\langle \left|S_{VV}\right|^2 \right\rangle} = \frac{\left(1-\rho_{HH-VV}\right)}{4} \\ \Downarrow \\ \frac{\left\langle \left|S_{HV}\right|^2 \right\rangle}{\left\langle \left|S_{HH}\right|^2 \right\rangle + \left\langle \left|S_{VV}\right|^2 \right\rangle} = \frac{\left(1-\rho_{HH-VV}\right)}{N},\end{gathered} \tag{3.58}$$

where

$$N = \frac{\left\langle \left|S_{HH} - S_{VV}\right|^2 \right\rangle}{\left\langle \left|S_{HV}\right|^2 \right\rangle}. \tag{3.59}$$

In order to define the parameter *N*, the correlation coefficient presented in (3.44) is considered

$$\rho_{HH-VV} = \frac{\left\langle S_{HH} S_{VV}^* \right\rangle}{\sqrt{\left\langle S_{HH} S_{HH}^* \right\rangle \left\langle S_{VV} S_{VV}^* \right\rangle}}. \tag{3.60}$$

Ever since the arithmetic mean is always greater than or equal to the geometric mean, follow

$$\frac{\left\langle \left|S_{HH}\right|^2 \right\rangle + \left\langle \left|S_{VV}\right|^2 \right\rangle}{2} \geq \sqrt{\left\langle S_{HH} S_{HH}^* \right\rangle \cdot \left\langle S_{VV} S_{VV}^* \right\rangle}. \tag{3.61}$$

Next, (3.61) into (3.60) gives

$$\frac{\left\langle \left|S_{HH}\right|^2 \right\rangle + \left\langle \left|S_{VV}\right|^2 \right\rangle}{2} \geq \frac{\left\langle \left|S_{HH} S_{VV}^*\right| \right\rangle}{\left|\rho_{HH-VV}\right|}. \tag{3.62}$$

Expression (3.62) can be rewrite as

$$-\left|\rho_{HH-VV}\right|\left(\left\langle\left|S_{HH}\right|^2\right\rangle+\left\langle\left|S_{VV}\right|^2\right\rangle\right)\leq-2\left\langle\left|S_{HH}S_{VV}^*\right|\right\rangle. \tag{3.63}$$

Next, the expression $\left(\left\langle\left|S_{HH}\right|^2\right\rangle+\left\langle\left|S_{VV}\right|^2\right\rangle\right)$ is added in both sides of (3.63)

$$\begin{aligned}\left(\left\langle\left|S_{HH}\right|^2\right\rangle+\left\langle\left|S_{VV}\right|^2\right\rangle\right)-\left|\rho_{HH-VV}\right|\left(\left\langle\left|S_{HH}\right|^2\right\rangle+\left\langle\left|S_{VV}\right|^2\right\rangle\right)\leq\\ \left(\left\langle\left|S_{HH}\right|^2\right\rangle+\left\langle\left|S_{VV}\right|^2\right\rangle\right)-2\left\langle\left|S_{HH}S_{VV}^*\right|\right\rangle,\end{aligned} \tag{3.64}$$

$$\left(1-\left|\rho_{HH-VV}\right|\right)\left(\left\langle\left|S_{HH}\right|^2\right\rangle+\left\langle\left|S_{VV}\right|^2\right\rangle\right)\leq\left(\left\langle\left|S_{HH}\right|^2\right\rangle+\left\langle\left|S_{VV}\right|^2\right\rangle\right)-2\left\langle\left|S_{HH}S_{VV}^*\right|\right\rangle. \tag{3.65}$$

Now, considering that the new relation

$$\left|S_{HH}\cdot S_{VV}^*\right|\geq\Re\left\langle S_{HH}\cdot S_{VV}^*\right\rangle, \tag{3.66}$$

the inequality still holds if consider (3.66) into (3.65), so

$$\left(1-\left|\rho_{HH-VV}\right|\right)\left(\left\langle\left|S_{HH}\right|^2\right\rangle+\left\langle\left|S_{VV}\right|^2\right\rangle\right)\leq\left(\left\langle\left|S_{HH}\right|^2\right\rangle+\left\langle\left|S_{VV}\right|^2\right\rangle\right)-2\Re\left\langle S_{HH}S_{VV}^*\right\rangle. \tag{3.67}$$

The right side of (3.67) can be substitute for the complex number

$$\left\langle\left|S_{HH}\right|^2\right\rangle+\left\langle\left|S_{VV}\right|^2\right\rangle-\Re\left\{\left\langle S_{HH}\right\rangle\left\langle S_{VV}\right\rangle\right\}=\left\langle\left|S_{HH}-S_{VV}\right|^2\right\rangle. \tag{3.68}$$

Then, (3.67) can be rewrite as

$$\left(1-\left|\rho_{HH-VV}\right|\right)\left(\left\langle\left|S_{HH}\right|^2\right\rangle+\left\langle\left|S_{VV}\right|^2\right\rangle\right)\leq\left\langle\left|S_{HH}-S_{VV}\right|^2\right\rangle. \tag{3.69}$$

Notice that the term $S_{HH}-S_{VV}$ is one of elements of the Pauli basis related to the double-bounce scattering.

Next, the terms of (3.69) are rearranging as

$$\frac{1}{\left\langle \left|S_{HH}\right|^2 \right\rangle + \left\langle \left|S_{VV}\right|^2 \right\rangle} \geq \frac{1-\left|\rho_{HH-VV}\right|}{\left\langle \left|S_{HH}-S_{VV}\right|^2 \right\rangle} \ . \tag{3.70}$$

And, finally, the both sides of (3.70) are multiplying by $\left\langle \left|S_{HV}\right|^2 \right\rangle$

$$\begin{gathered}
\frac{\left\langle \left|S_{HV}\right|^2 \right\rangle}{\left\langle \left|S_{HH}\right|^2 \right\rangle + \left\langle \left|S_{VV}\right|^2 \right\rangle} \geq \frac{1-\left|\rho_{HH-VV}\right|}{\dfrac{\left\langle \left|S_{HH}-S_{VV}\right|^2 \right\rangle}{\left\langle \left|S_{HV}\right|^2 \right\rangle}}, \\
\Downarrow \\
\frac{\left\langle \left|S_{HV}\right|^2 \right\rangle}{\left\langle \left|S_{HH}\right|^2 \right\rangle + \left\langle \left|S_{VV}\right|^2 \right\rangle} = \frac{1-\left|\rho_{HH-VV}\right|}{N}.
\end{gathered} \tag{3.71}$$

The new expression (3.71) leads to rewrite (3.52) as

$$X_{nd}^{(n)} = \left(C_{cp11} + C_{cp22}\right) \frac{\left|\left(1-\rho_{HH-VV}\right)\right|}{\left|N + 2\left(1-\rho_{HH-VV}\right)\right|} \,. \tag{3.72}$$

The Nord approach is not the focus of this Thesis. However, the methodology used considers this algorithm in order to compare with the CP_{az} algorithm.

3.3. The Proposed Azimuthal Method

Most previous works have assumed reflection symmetry as the basis for studying CP [6]–[10], [12], [13], [44]. However, considering the premises adopted for the Brazilian scenario and the fact that the Earth’s ionosphere above this country characterizes an environment with irregularities, such as plasma bubbles and Medium Scale Traveling Ionospheric Disturbances (MSTIDs), with characteristics of rotation symmetry [5], [14], the main contribution of this research is to analyze an algorithm for CP, considering the azimuthal symmetry (from now on called CP_{az} algorithm).

Following the same process described by Souyris et al. [6], the matrix (2.30) is rearranged into a sum of three matrices. The first one encompasses only the co-POL terms (HH and VV); in the second matrix, only the terms with cross-POL (HV and VH) are included. The last one contains residual terms that are disregarded due to the low entropy value for the set considered in the evaluation of the algorithm as demonstrate in chapter 4. Therefore, the set of equations presented in (2.33), (2.35), and (2.36) can be rewriting in (3.73), as follows

$$C_{Rhc} = C_{co-POL} + C_{cr-POL} + C_{res}$$

$$C_{co-POL} = \frac{1}{2}\begin{bmatrix} \left\langle |S_{HH}|^2 \right\rangle & \left\langle jS_{HH}S_{VV}^* \right\rangle \\ \left\langle -jS_{VV}S_{HH}^* \right\rangle & \left\langle |S_{VV}|^2 \right\rangle \end{bmatrix}$$

$$C_{cr-POL} = \frac{1}{2}\begin{bmatrix} \left\langle |S_{HV}|^2 \right\rangle & -\left\langle jS_{HV}S_{HV}^* \right\rangle \\ \left\langle j|S_{HV}|^2 \right\rangle & \left\langle |S_{HV}|^2 \right\rangle \end{bmatrix} = \frac{1}{2}\begin{bmatrix} \left\langle |S_{HV}|^2 \right\rangle & -\left\langle j|S_{HV}|^2 \right\rangle \\ \left\langle j|S_{HV}|^2 \right\rangle & \left\langle |S_{HV}|^2 \right\rangle \end{bmatrix}$$

$$C_{res} = \frac{1}{2}\begin{bmatrix} \left\langle -2\Im\left(S_{HH}S_{HV}^*\right) \right\rangle & \left\langle S_{HH}S_{HV}^* + S_{HV}S_{VV}^* \right\rangle \\ \left\langle S_{HV}S_{HH}^* + S_{VV}S_{HV}^* \right\rangle & \left\langle 2\Im\left(S_{VV}S_{HV}^*\right) \right\rangle \end{bmatrix}$$

$$C_{Rhc}=\frac{1}{2}\left(\begin{bmatrix}\left\langle\left|S_{HH}\right|^{2}\right\rangle+\left\langle\left|S_{HV}\right|^{2}\right\rangle & -j\left\langle S_{HH}S_{VV}^{*}\right\rangle+\left\langle\left|S_{HV}\right|^{2}\right\rangle\\ j\left\langle S_{HH}S_{VV}^{*}\right\rangle-\left\langle\left|S_{HV}\right|^{2}\right\rangle & \left\langle\left|S_{VV}\right|^{2}\right\rangle+\left\langle\left|S_{HV}\right|^{2}\right\rangle\end{bmatrix}\right). \tag{3.73}$$

Therefore, C_{cp11}, C_{cp12}, and C_{cp22} are defined comparing (2.30) with (3.73) and they are presented in (3.74).

$$C_{Rhc}=\begin{bmatrix}C_{cp11} & C_{cp12}\\ C_{cp21} & C_{cp22}\end{bmatrix}=\begin{bmatrix}\left\langle\left|S_{RH}\right|^{2}\right\rangle & \left\langle S_{RH}S_{RV}^{*}\right\rangle\\ \left\langle S_{RV}S_{RH}^{*}\right\rangle & \left\langle\left|S_{RV}\right|^{2}\right\rangle\end{bmatrix}$$

$$\begin{aligned}2C_{cp11}&=\left\langle\left|S_{HH}\right|^{2}\right\rangle+\left\langle\left|S_{HV}\right|^{2}\right\rangle\\ 2C_{cp12}&=-j\left\langle S_{HV}S_{HV}^{*}\right\rangle+\left\langle\left|S_{HV}\right|^{2}\right\rangle\\ 2C_{cp22}&=\left\langle\left|S_{VV}\right|^{2}\right\rangle+\left\langle\left|S_{HV}\right|^{2}\right\rangle.\end{aligned} \tag{3.74}$$

The next step in this approach considers the azimuthal symmetry conditions [5], which represents the conditions of reflection symmetry (observed in 3.39) adjoining with rotation symmetry (3.75-3.91).

Reflection Symmetry

$$\begin{aligned}\left\langle S_{HH}S_{HV}^{*}\right\rangle=\left\langle S_{HV}S_{HH}^{*}\right\rangle=\left\langle S_{VV}S_{VH}^{*}\right\rangle=\left\langle S_{VH}S_{VV}^{*}\right\rangle=0\\ \left\langle S_{HH}S_{VH}^{*}\right\rangle=\left\langle S_{VH}S_{HH}^{*}\right\rangle=\left\langle S_{VV}S_{HV}^{*}\right\rangle=\left\langle S_{HV}S_{VV}^{*}\right\rangle=0.\end{aligned}$$

Rotation Symmetry

$$\Re\left\{S_{HH}S_{HV}^{*}\right\}=-\Re\left\{S_{VH}S_{VV}^{*}\right\}=\Re\left\{S_{HV}S_{VV}^{*}\right\} \tag{3.75}$$

$$\Im\left\{S_{HH}S_{HV}^{*}\right\}=\Im\left\{S_{VH}S_{VV}^{*}\right\} \tag{3.76}$$

$$\Re\left\{S_{HH}S_{VH}^{*}\right\}=-\Re\left\{S_{HV}S_{VV}^{*}\right\}=\Re\left\{S_{VH}S_{VV}^{*}\right\} \tag{3.77}$$

$$\Im\left\{S_{HH}S_{VH}^{*}\right\}=\Im\left\{S_{HV}S_{VV}^{*}\right\} \tag{3.78}$$

$$\Im\left\{S_{HH}S_{VV}^{*}\right\}=0 \tag{3.79}$$

$$\Im\left\{S_{HV}S_{VH}^{*}\right\}=0 \tag{3.80}$$

$$S_{HH}S_{HH}^{*}=S_{VV}S_{VV}^{*} \tag{3.81}$$

$$S_{HV}S_{HV}^{*}=S_{VH}S_{VH}^{*} \tag{3.82}$$

$$S_{HV}S_{HV}^{*}+S_{VH}S_{VH}^{*}+2\Re\left\{S_{HV}S_{VH}^{*}\right\}=S_{HH}S_{HH}^{*}+S_{VV}S_{VV}^{*}-2\Re\left\{S_{HH}S_{VV}^{*}\right\}, \tag{3.83}$$

which can be reorganized in the following relations

$$\frac{\Re\left\{S_{HH}S_{HV}^{*}\right\}+\Re\left\{S_{HH}S_{VH}^{*}\right\}}{2}=\frac{\Re\left\{S_{HV}S_{VV}^{*}\right\}+\Re\left\{S_{VH}S_{VV}^{*}\right\}}{2}=0\,, \tag{3.84}$$

$$\frac{\Im\left\{S_{HH}S_{HV}^{*}\right\}+\Im\left\{S_{HH}S_{VH}^{*}\right\}}{2}=\frac{\Im\left\{S_{HV}S_{VV}^{*}\right\}+\Im\left\{S_{VH}S_{VV}^{*}\right\}}{2}\,, \tag{3.85}$$

$$\frac{S_{HV}S_{HV}^{*}+S_{VH}S_{VH}^{*}+2\Re\left\{S_{HV}S_{VH}^{*}\right\}}{4}=\frac{S_{HH}S_{HH}^{*}+S_{VV}S_{VV}^{*}-2\Re\left\{S_{HH}S_{VV}^{*}\right\}}{4}\,. \tag{3.86}$$

By the expressions (3.84) and (3.85), it is noted that, for a medium with rotation symmetry, the mean return of the cross-POL components equals the difference between the co-POL elements, summarized in the expression

$$\left|\frac{S_{HV}+S_{VH}}{2}\right|^{2}=\left|\frac{S_{HH}-S_{VV}}{2}\right|^{2}\,. \tag{3.87}$$

Considering the Theorem of reciprocity, the expressions from (3.75) to (3.86) reduce to

$$\left\langle S_{HH}S_{HV}^{*}\right\rangle=\left\langle S_{HV}S_{VV}^{*}\right\rangle \tag{3.88}$$

$$\left\langle\Im\left\{S_{HH}S_{VV}^{*}\right\}\right\rangle=0\Rightarrow\left\langle S_{HH}S_{VV}^{*}\right\rangle=\left\langle\Re\left\{S_{HH}S_{VV}^{*}\right\}\right\rangle \tag{3.89}$$

$$\left\langle\left|S_{HH}\right|^{2}\right\rangle=\left\langle\left|S_{VV}\right|^{2}\right\rangle \tag{3.90}$$

$$\begin{aligned}
&4\left\langle \left|S_{HV}\right|^{2}\right\rangle = \left\langle \left|S_{HH}\right|^{2}\right\rangle + \left\langle \left|S_{VV}\right|^{2}\right\rangle - 2\left\langle \Re\left\{S_{HH}S_{VV}^{*}\right\}\right\rangle \\
&2\left\langle \left|S_{HV}\right|^{2}\right\rangle = \left\langle \left|S_{HH}\right|^{2}\right\rangle - \left\langle S_{HH}S_{VV}^{*}\right\rangle \Rightarrow \left\langle S_{HH}S_{VV}^{*}\right\rangle = \left\langle \left|S_{HH}\right|^{2}\right\rangle - 2\left\langle \left|S_{HV}\right|^{2}\right\rangle .
\end{aligned} \tag{3.91}$$

Regarding the matrix of Covariance presented in (2.26), observing the relations (3.81) and (3.84), $C^{Full-POL(3\times3)}$ becomes

$$C_{rot}^{Full-POL(3\times3)} = \begin{bmatrix} \left\langle \left|S_{HH}\right|^{2}\right\rangle & \sqrt{2}\left\langle S_{HH}S_{HV}^{*}\right\rangle & \left\langle \left|S_{HH}\right|^{2}\right\rangle - 2\left\langle \left|S_{HV}\right|^{2}\right\rangle \\ \sqrt{2}\left\langle S_{HV}S_{HH}^{*}\right\rangle & 2\left\langle \left|S_{HV}\right|^{2}\right\rangle & \sqrt{2}\left\langle S_{HV}S_{VV}^{*}\right\rangle \\ \left\langle \left|S_{HH}\right|^{2}\right\rangle - 2\left\langle \left|S_{HV}\right|^{2}\right\rangle & \sqrt{2}\left\langle S_{VV}S_{HV}^{*}\right\rangle & \left\langle \left|S_{HH}\right|^{2}\right\rangle \end{bmatrix}. \tag{3.92}$$

Including the angle of Faraday rotation Ψ, we have six unknown terms, instead of the five presented next to the expression (3.40), namely, $\left\langle S_{HH}S_{HH}^{*}\right\rangle, \left\langle S_{VV}S_{VV}^{*}\right\rangle, \left\langle S_{HV}S_{HV}^{*}\right\rangle$, $\left\langle S_{HH}S_{VV}^{*}\right\rangle$, and Ψ. According to Souyris [6], the only way to circumvent these indeterminations, and to be possible to estimate the elements in the Coherence matrix of a Complete Polarization system, is to assume the azimuthal symmetry conditions where

Azimuthal Symmetry

$$\left\langle \left|S_{HH}\right|^{2}\right\rangle = \left\langle \left|S_{VV}\right|^{2}\right\rangle , \tag{3.93}$$

$$\left\langle \left|S_{HV}\right|^{2}\right\rangle = \left\langle \left|S_{VH}\right|^{2}\right\rangle , \tag{3.94}$$

$$\left\langle \left|S_{HV}\right|^{2}\right\rangle + \left\langle \left|S_{VH}\right|^{2}\right\rangle + 2\left\langle \Re\left\{S_{HV}S_{VH}^{*}\right\}\right\rangle = \left\langle \left|S_{HH}\right|^{2}\right\rangle + \left\langle \left|S_{VV}\right|^{2}\right\rangle - 2\left\langle \Re\left\{S_{HH}S_{VV}^{*}\right\}\right\rangle , \tag{3.95}$$

$$\left|\frac{\left\langle S_{HV}\right\rangle + \left\langle S_{VH}\right\rangle}{2}\right|^{2} = \left|\frac{\left\langle S_{HH}\right\rangle - \left\langle S_{VV}\right\rangle}{2}\right|^{2} . \tag{3.96}$$

Considering the Reciprocity Principle, (3.93-3.96) can be rewritten respectively by

$$\left\langle \left|S_{HH}\right|^{2} \right\rangle = \left\langle \left|S_{VV}\right|^{2} \right\rangle . \tag{3.97}$$

Following the mathematical development

$$\begin{gathered}
\left|\left\langle S_{HV} \right\rangle\right|^{2} = \left| \frac{\left\langle S_{HH} \right\rangle - \left\langle S_{VV} \right\rangle}{2} \right|^{2} \Rightarrow\ 4\left|\left\langle S_{HV} \right\rangle\right|^{2} = \left|\left\langle S_{HH} \right\rangle - \left\langle S_{VV} \right\rangle\right|^{2} \\
4\left\langle \left|S_{HV}\right|^{2} \right\rangle = \left\langle \left|S_{HH}\right|^{2} \right\rangle + \left\langle \left|S_{VV}\right|^{2} \right\rangle - 2\left\langle \Re\left\{ S_{HH} S_{VV}^{*} \right\} \right\rangle \\
2\left\langle \left|S_{HH}\right|^{2} \right\rangle - 2\left\langle \Re\left\{ S_{HH} S_{VV}^{*} \right\} \right\rangle = \left\langle \left|S_{HH}\right|^{2} \right\rangle + \left\langle \left|S_{VV}\right|^{2} \right\rangle - 2\left\langle \Re\left\{ S_{HH} S_{VV}^{*} \right\} \right\rangle \\
1 - \frac{2\left\langle \Re\left\{ S_{HH} S_{VV}^{*} \right\} \right\rangle}{\left\langle \left|S_{HH}\right|^{2} \right\rangle + \left\langle \left|S_{VV}\right|^{2} \right\rangle} = \frac{4\left\langle \left|S_{HV}\right|^{2} \right\rangle}{\left\langle \left|S_{HH}\right|^{2} \right\rangle + \left\langle \left|S_{VV}\right|^{2} \right\rangle} \\
1 - \frac{2\left\langle \Re\left\{ S_{HH} S_{VV}^{*} \right\} \right\rangle}{2\left\langle \left|S_{HH}\right|^{2} \right\rangle} = 1 - \frac{4\left\langle \left|S_{HV}\right|^{2} \right\rangle}{\left\langle \left|S_{HH}\right|^{2} \right\rangle + \left\langle \left|S_{VV}\right|^{2} \right\rangle} \\
\Rightarrow \left\langle S_{HH} S_{VV}^{*} \right\rangle = \left\langle \left|S_{HH}\right|^{2} \right\rangle - 2\left\langle \left|S_{HV}\right|^{2} \right\rangle \\
4\left\langle \left|S_{HV}\right|^{2} \right\rangle = \left\langle \left|S_{HH}\right|^{2} \right\rangle + \left\langle \left|S_{VV}\right|^{2} \right\rangle - 2\left\langle \Re\left\{ S_{HH} S_{VV}^{*} \right\} \right\rangle \\
\left\langle \left|S_{HV}\right|^{2} \right\rangle = \left| \frac{\left\langle S_{HH} \right\rangle - \left\langle S_{VV} \right\rangle}{2} \right|^{2} .
\end{gathered} \tag{3.98}$$

Hence, the azimuthal symmetry conditions can be summarized as

$$\left\langle \left|S_{HV}\right|^{2} \right\rangle = X_{az} \cong \frac{\left\langle \left|S_{HH}\right|^{2} \right\rangle + \left\langle \left|S_{VV}\right|^{2} \right\rangle - 2\Re\left\langle S_{HH} S_{HV}^{*} \right\rangle}{4} , \tag{3.99}$$

where the 3×3 Covariance matrix for a Full Polarimetric (Full-POL) system is given by

$$C_{az}^{Full-POL(3\times3)} = \begin{bmatrix} \left\langle \left|S_{HH}\right|^{2} \right\rangle & 0 & \left\langle \left|S_{HH}\right|^{2} \right\rangle - 2\left\langle \left|S_{HV}\right|^{2} \right\rangle \\ 0 & 2\left\langle \left|S_{HV}\right|^{2} \right\rangle & 0 \\ \left\langle \left|S_{HH}\right|^{2} \right\rangle - 2\left\langle \left|S_{HV}\right|^{2} \right\rangle & 0 & \left\langle \left|S_{HH}\right|^{2} \right\rangle \end{bmatrix} . \tag{3.100}$$

Considering the linear interpolation of Souyris [34], now focusing on the Ionospheric environment and considering the possible simplifications of the azimuthal symmetry, it can be verified that the conditions presented for the scattering of completely polarized waves do not change. In other words, the scattering of the cross-POL energy is very small, while the co-POL components are almost perfectly correlated, so we have

$$\left\langle |S_{HV}|^2 \right\rangle \approx 0, \tag{3.101}$$

$$\rho_{HH-VV} = \frac{\left\langle S_{HH} S_{VV}^* \right\rangle}{\sqrt{\left\langle S_{HH} S_{HH}^* \right\rangle \left\langle S_{VV} S_{VV}^* \right\rangle}} \approx 1. \tag{3.102}$$

However, for completely depolarized waves and considering the previous relations for azimuthal symmetry, we have

$$\left\langle |S_{HV}|^2 \right\rangle \cong \frac{\left\langle |S_{HH}|^2 \right\rangle + \left\langle |S_{VV}|^2 \right\rangle - 2\Re\left\{ S_{HH} S_{VV}^* \right\}}{4}, \tag{3.103}$$

$$\rho_{HH-VV} = \frac{\left\langle S_{HH} S_{VV}^* \right\rangle}{\sqrt{\left\langle S_{HH} S_{HH}^* \right\rangle \left\langle S_{VV} S_{VV}^* \right\rangle}} \approx 0 . \tag{3.104}$$

Since these two cases are considered limits of the physical interpretation of the spreading mechanism, a linear interpolation of the polarization state is proposed, as shown in Figure 3.6.

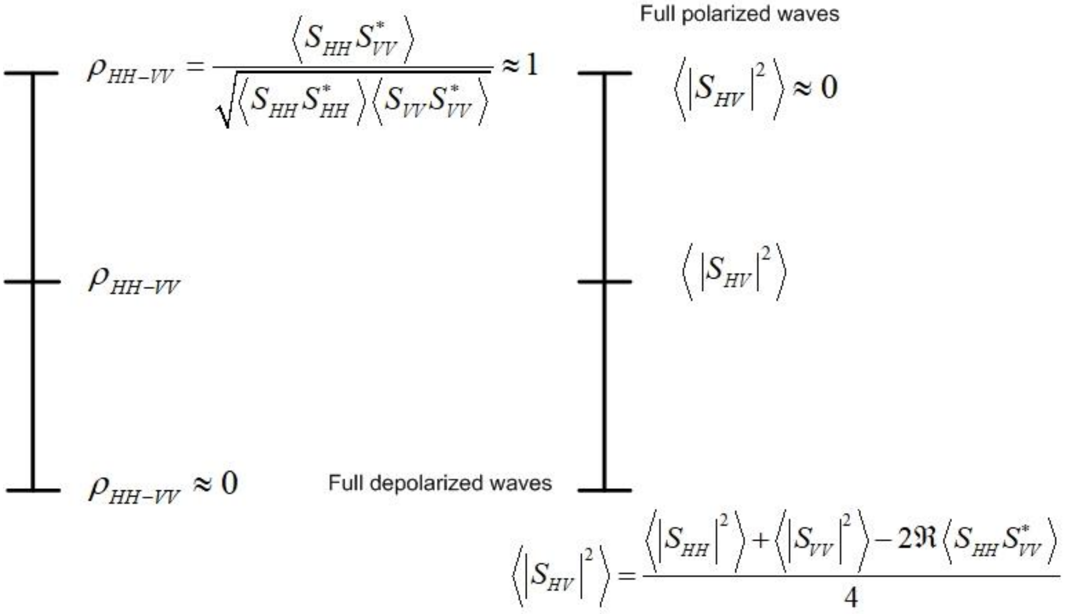

Figure 3.6 – Linear interpolation of the state of polarization for CP_{az} (azimuthal symmetry).

Comparing these two states of polarization related to the full polarized scattered waves and full depolarized scattered waves, which are considered limits of the physical interpretation of the scattering mechanism, the following relations are established

$$\frac{\rho_{HH-VV}-0}{\left\langle |S_{HV}|^2\right\rangle - \frac{|S_{HH}|^2+|S_{VV}|^2-2\Re\left\{S_{HH}S_{VV}^*\right\}}{4}} = \frac{1-0}{0-\frac{|S_{HH}|^2+|S_{VV}|^2-2\Re\left\{S_{HH}S_{VV}^*\right\}}{4}} \tag{3.105}$$

$$\frac{4\rho_{HH-VV}}{4\left\langle |S_{HV}|^2\right\rangle - |S_{HH}|^2 - |S_{VV}|^2 + 2\Re\left\{S_{HH}S_{VV}^*\right\}} = \frac{4}{2\Re\left\{S_{HH}S_{VV}^*\right\} - |S_{HH}|^2 - |S_{VV}|^2}$$

$$\begin{aligned} 4\left\langle |S_{HV}|^2\right\rangle - |S_{HH}|^2 - |S_{VV}|^2 + 2\Re\left\{S_{HH}S_{VV}^*\right\} = \\ 2\Re\left\{S_{HH}S_{VV}^*\right\}\cdot\rho_{HH-VV} - |S_{HH}|^2\cdot\rho_{HH-VV} - |S_{VV}|^2\cdot\rho_{HH-VV} \end{aligned}$$

$$\begin{aligned} 4\left\langle |S_{HV}|^2\right\rangle = -\rho_{HH-VV}\left(|S_{HH}|^2+|S_{VV}|^2-2\Re\left\{S_{HH}S_{VV}^*\right\}\right) \\ +\left(|S_{HH}|^2+|S_{VV}|^2-2\Re\left\{S_{HH}S_{VV}^*\right\}\right) \end{aligned}$$

$$\left\langle |S_{HV}|^2\right\rangle = \frac{(1-\rho_{HH-VV})}{4}\cdot\left(|S_{HH}|^2+|S_{VV}|^2-2\Re\left\{S_{HH}S_{VV}^*\right\}\right). \tag{3.106}$$

Which can be summarized as

$$\rho_{HH-VV} = \rho_{az} = \frac{\left\langle S_{HH} S_{VV}^{*} \right\rangle}{\sqrt{\left\langle S_{HH} S_{HH}^{*} \right\rangle \left\langle S_{VV} S_{VV}^{*} \right\rangle}}, \tag{3.107}$$

$$\frac{1-\rho_{az}}{4} \simeq \frac{\left\langle \left| S_{HV} \right|^{2} \right\rangle}{\left\langle \left| S_{HH} \right|^{2} \right\rangle + \left\langle \left| S_{VV} \right|^{2} \right\rangle - 2\Re \left\langle S_{HH} S_{VV}^{*} \right\rangle}. \tag{3.108}$$

Back to expression (3.106), we have

$$\begin{aligned}
& X_{az} = \frac{\left(1-\rho_{az}\right)}{4} \cdot \left(2C_{cp11} - X_{az} + 2C_{cp22} - X_{az} - 2\Re\left\{S_{HH} S_{VV}^{*}\right\}\right) \\
& X_{az} = \\
& \quad \frac{\left(1-\rho_{az}\right)}{4} \cdot \left(2C_{cp11} - X_{az} + 2C_{cp22} - X_{az} - \Re\left\{S_{HH} S_{VV}^{*}\right\} - \Re\left\{S_{HH} S_{VV}^{*}\right\}\right) \\
& X_{az} = \frac{\left(1-\rho_{az}\right)}{4} \cdot \\
& \quad \left(2C_{cp11} - X_{az} + 2C_{cp22} - X_{az} - \Re\left\{-2jC_{cp12} + X_{az}\right\} - \Re\left\{-2jC_{cp12} + X_{az}\right\}\right) \\
& X_{az} = \frac{\left(1-\rho_{az}\right)}{4} \cdot \left(2C_{cp11} - X_{az} + 2C_{cp22} - X_{az} - 4\Re\left\{-2jC_{cp12}\right\} - 2X_{az}\right) \\
& 4X_{az} = 2C_{cp11} + 2C_{cp22} - 4X_{az} - 4\Re\left\{-2jC_{cp12}\right\} - \\
& \qquad 2C_{cp11}\rho_{az} - 2C_{cp22}\rho_{az} + 4X_{az}\rho_{az} + 4\Re\left\{-2jC_{cp12}\right\}\rho_{az} \\
& 8X_{az} - 4X_{az}\rho_{az} = \left(1-\rho_{az}\right)\left(2C_{cp11} + 2C_{cp22} - 4\Re\left\{-2jC_{cp12}\right\}\right) \\
& 4X_{az}\left(2-\rho_{az}\right) = 2\cdot\left(1-\rho_{az}\right)\left(C_{cp11} + C_{cp22} - 2\Re\left\{-2jC_{cp12}\right\}\right) \\
& 2X_{az}\left(2-\rho_{az}\right) = \left(1-\rho_{az}\right)\left(C_{cp11} + C_{cp22} - 2\Re\left\{-2jC_{cp12}\right\}\right).
\end{aligned} \tag{3.109}$$

So

$$X_{az} = \frac{\left(1-\rho_{az}\right)\left(C_{cp11} + C_{cp22} - 2\Re\left\{-2jC_{cp12}\right\}\right)}{2\left(2-\rho_{az}\right)}. \tag{3.110}$$

Once defined the initial conditions, an iterative process with three steps was designed as in (3.51-3.54) to make possible a CP_{az} pseudo reconstruction, where

Step 1 - Initialization

$$X_{az}^{(0)} = 0$$
$$\rho_{az}^{(0)} = \frac{\left| -j2C_{cp12} \right|}{\sqrt{2C_{cp11} 2C_{cp22}}}, \tag{3.111}$$

Step 2 - Iterations

$$X_{az}^{(n)} = \frac{1}{2}\left(C_{cp11} + C_{cp22} - 2\Re\left\{ -jC_{cp12} \right\} \right) \frac{\left(1 - |\rho_{az}|\right)}{\left(2 - |\rho_{az}|\right)}. \tag{3.112}$$

$$\rho_{az}^{(n)} = \frac{\left| -2jC_{cp12} + X_{az} \right|}{\sqrt{\left(2C_{cp11} - X_{az}\right) \cdot \left(2C_{cp22} - X_{az}\right)}}. \tag{3.113}$$

Where the value at (3.80) updates the value of X_{az} and *n* is the number of iterations.

Step 3 - Reconstruction

$$C_{az}^{CP(3\times3)} = \left\langle \begin{bmatrix} C_{cp11} - X_{az} & 0 & C_{cp11} - 3X_{az} \\ 0 & 2X_{az} & 0 \\ C_{cp11} - X_{az} & 0 & C_{cp22} - X_{az} \end{bmatrix} \right\rangle. \tag{3.114}$$

Notice that the elements 11 and 33 in (3.106) are not considered with the same value as presented in (3.100). This is the way to avoid superposition from HH into VV, leading to only two measurements. In this case, we considered a “light” azimuthal symmetry case [6].

4. METHODOLOGY

The methodology follows the sequence presented in Figure 4.7.

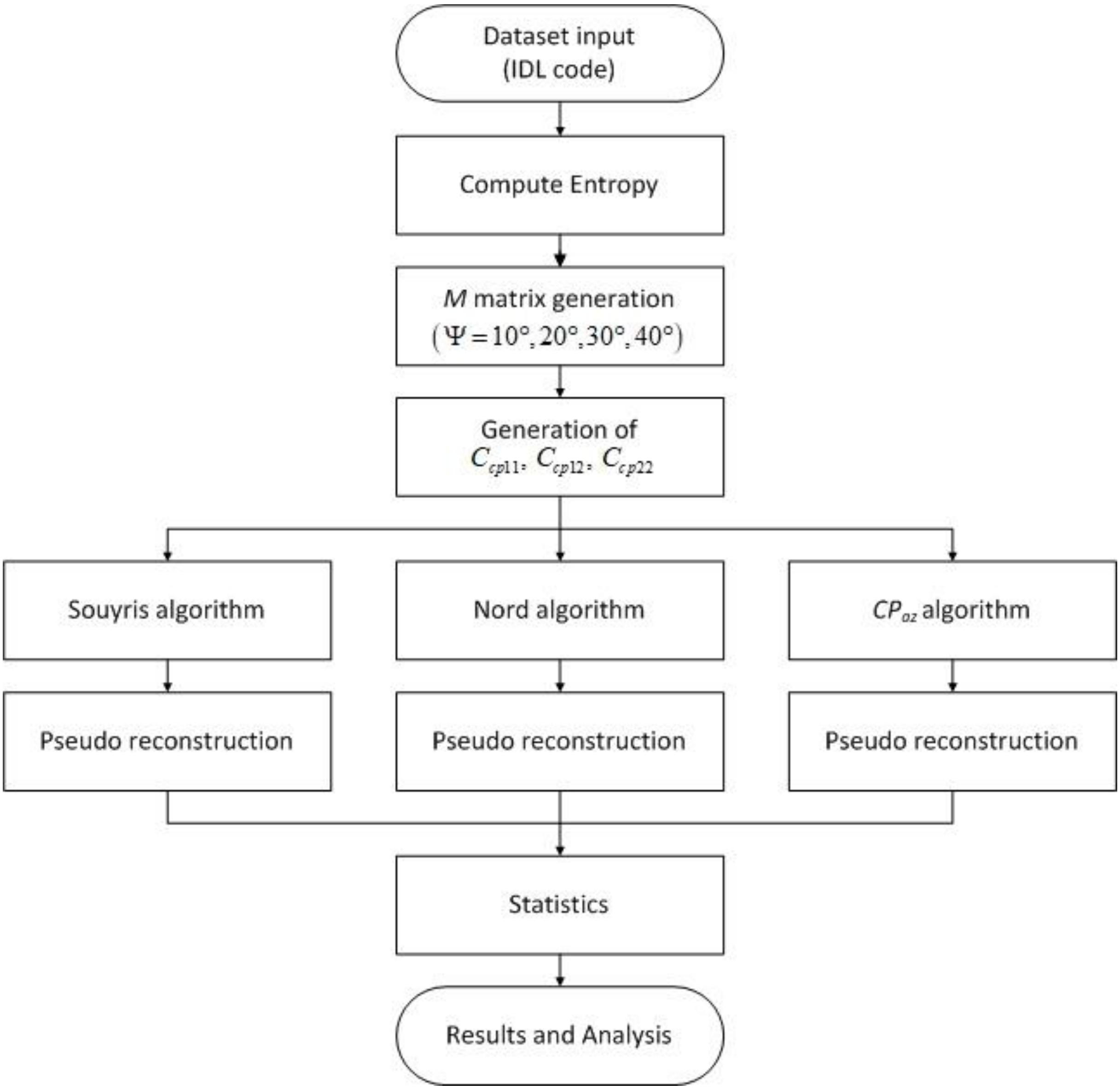

Figure 4.7 – Methodology.

All codes developed for this research are implemented in IDL programming language.

The first step is the definition of an input dataset and the reading of the amplitude of HH, HV, VH, and VV images.

In the following, the entropy [38], [46] of the matrices C_{co-POL} (2.34), C_{cr-POL} (2.35), and C_{res} (2.36) is computed. The matrices are reproduced in the sequence:

$$C_{Rhc} = C_{co-POL} + C_{cr-POL} + C_{res} \tag{2.33}$$

$$C_{co-POL} = \frac{1}{2}\begin{bmatrix} \left\langle |S_{HH}|^2 \right\rangle & \left\langle jS_{HH}S_{VV}^* \right\rangle \\ \left\langle -jS_{VV}S_{HH}^* \right\rangle & \left\langle |S_{VV}|^2 \right\rangle \end{bmatrix} \tag{2.34}$$

$$C_{cr-POL} = \frac{1}{2}\begin{bmatrix} \left\langle |S_{HV}|^2 \right\rangle & -\left\langle jS_{HV}S_{HV}^* \right\rangle \\ \left\langle j|S_{HV}|^2 \right\rangle & \left\langle |S_{HV}|^2 \right\rangle \end{bmatrix} = \frac{1}{2}\begin{bmatrix} \left\langle |S_{HV}|^2 \right\rangle & -\left\langle j|S_{HV}|^2 \right\rangle \\ \left\langle j|S_{HV}|^2 \right\rangle & \left\langle |S_{HV}|^2 \right\rangle \end{bmatrix} \tag{2.35}$$

$$C_{res} = \frac{1}{2}\begin{bmatrix} \left\langle -2\Im\left(S_{HH}S_{HV}^*\right) \right\rangle & \left\langle S_{HH}S_{HV}^* + S_{HV}S_{VV}^* \right\rangle \\ \left\langle S_{HV}S_{HH}^* + S_{VV}S_{HV}^* \right\rangle & \left\langle 2\Im\left(S_{VV}S_{HV}^*\right) \right\rangle \end{bmatrix}. \tag{2.36}$$

This step is conducted in order to verify if the expression C_{res} (2.36) can be disregarded for the next steps of the process due to low entropy values.

$$C_{res} = \frac{1}{2}\begin{bmatrix} \left\langle -2\Im\left(S_{HH}S_{HV}^*\right) \right\rangle & \left\langle S_{HH}S_{HV}^* + S_{HV}S_{VV}^* \right\rangle \\ \left\langle S_{HV}S_{HH}^* + S_{VV}S_{HV}^* \right\rangle & \left\langle 2\Im\left(S_{VV}S_{HV}^*\right) \right\rangle \end{bmatrix}.$$

It is expected higher entropy values from C_{co-POL} (2.34) matrix, followed by low entropy values for the C_{cr-POL} (2.35) matrix, and almost zero for the C_{res} (2.36). Another way to disregard C_{cr-POL} (2.35) matrix is to consider the assumption of reflection symmetry [7], observing the conditions presented in (3.39) as follows:

$$\begin{aligned}
\left\langle S_{HH} S_{HV}^{*} \right\rangle = \left\langle S_{HV} S_{HH}^{*} \right\rangle = \left\langle S_{VV} S_{VH}^{*} \right\rangle = \left\langle S_{VH} S_{VV}^{*} \right\rangle = 0 \\
\left\langle S_{HH} S_{VH}^{*} \right\rangle = \left\langle S_{VH} S_{HH}^{*} \right\rangle = \left\langle S_{VV} S_{HV}^{*} \right\rangle = \left\langle S_{HV} S_{VV}^{*} \right\rangle = 0.
\end{aligned}$$

To simulate the Faraday Rotation effect, we use the *M* matrix [54] presented in Appendix B (equation B.19).

$$\begin{aligned}
M_{HH} &= S_{HH} \cos^2 \Psi - S_{VV} \mathrm{sen}^2 \Psi + \left(S_{HV} - S_{VH} \right) \mathrm{sen} \Psi \cos \Psi, \\
M_{HV} &= S_{HV} \cos^2 \Psi + S_{VH} \mathrm{sen}^2 \Psi - \left(S_{HH} + S_{VV} \right) \mathrm{sen} \Psi \cos \Psi, \\
M_{VH} &= S_{VH} \cos^2 \Psi + S_{HV} \mathrm{sen}^2 \Psi + \left(S_{HH} + S_{VV} \right) \mathrm{sen} \Psi \cos \Psi, \\
M_{VV} &= S_{VV} \cos^2 \Psi - S_{HH} \mathrm{sen}^2 \Psi + \left(S_{HV} - S_{VH} \right) \mathrm{sen} \Psi \cos \Psi,
\end{aligned}$$

where Ψ is the Faraday rotation angle. For initial condition $\Psi = 0^{o}$, *M* reduces to *S* (2.18).

The use of the M matrix allows simulating the E-SAR transmission from the space. As mentioned before, the electromagnetic waves in Hybrid-POL do not suffer the influence of the Ionosphere on the transmission, but the echo undergoes a Ψ angle rotation. In this case, the signal transmitted has only a phase delay, and the echo signals polarized in H e V suffer the effects of Faraday rotation [34], [51], [52].

The Faraday rotation effects can significantly affect transmissions in L-band. The worst-case scenario happens during the day when solar irradiation contributes to the formation of anisotropic plasma. In these conditions Ψ can reach values of about 22.05^{o} to 41.0^{o} [54]. This range was considered to rotate the original dataset of 10^{o}, 20^{o}, 30^{o}, and 40^{o} to generate different pseudo reconstructions images in order to access the effect of the atmosphere.

The next step generates the C_{cp11}, C_{cp12}, and C_{cp22} matrices as defined in (3.48).

$$\begin{aligned} 2C_{cp11} &= \left\langle |S_{HH}|^2 \right\rangle + \left\langle |S_{HV}|^2 \right\rangle \\ 2C_{cp12} &= j\left\langle S_{HH}S_{VV}^* \right\rangle - j\left\langle |S_{HV}|^2 \right\rangle \\ 2C_{cp21} &= -j\left\langle S_{VV}S_{HH}^* \right\rangle + j\left\langle |S_{HV}|^2 \right\rangle \\ 2C_{cp22} &= \left\langle |S_{VV}|^2 \right\rangle + \left\langle |S_{HV}|^2 \right\rangle. \end{aligned} \tag{3.48}$$

Following, the Souyris algorithm [6], the Nord algorithm [7], and the CP_{az} algorithm were performed in order to provide the pseudo reconstruction datasets.

In this research, the Pearson correlation coefficient and the Root Mean Square Error (RMSE) are the statistics parameters used to compare the results obtained from CP_{az} algorithm with the ones from the algorithms of Souyris and Nord.

Equations (4.115) and (4.116) present the definition of these statistics parameters.

$$r = \frac{\left(p_x \sum_{i=1}^{p_x} \Upsilon_i \hat{\Upsilon}_i - \sum_{i=1}^{p_x} \Upsilon_i \hat{\Upsilon}_i\right)}{\sqrt{\left(p_x \sum_{i=1}^{p_x} \Upsilon_i^2 - \sum_{i=1}^{p_x} \Upsilon_i^2\right)\left(p_x \sum_{i=1}^{p_x} \hat{\Upsilon}_i^2 - \sum_{i=1}^{p_x} \hat{\Upsilon}_i^2\right)}},$$

$$r = \frac{\left(\sum_{i=1}^{p_x} \Upsilon_i \hat{\Upsilon}_i\right)}{\sqrt{\left(\sum_{i=1}^{p_x} \Upsilon_i^2\right)\left(\sum_{i=1}^{p_x} \hat{\Upsilon}_i^2\right)}}, \tag{4.115}$$

$$RMSE = \sqrt{\frac{1}{p_x} \sum_{i=1}^{p_x} \left(\Upsilon_i - \hat{\Upsilon}_i\right)^2}, \tag{4.116}$$

where r is the Pearson correlation coefficient, p_x is the total number of pixels, Υ_i is the value on pixel in location *i* of the true data Υ, and $\hat{\Upsilon}$ is the estimated data generated from pseudo reconstruction.

The Pearson correlation coefficient is a statistical measure of the correlation between two dataset. The range of *r* is

$$-1 \leq r \leq 1, \tag{4.117}$$

where:

a) Negative values indicate negative linear correlation;

b) The value of *0* indicates no correlation between the images;

c) Positive values indicate positive linear correlation; and

d) Values closer to -1 or 1 indicate higher correlation between the images.

The cases studied in this Thesis only consider $r \geq 0$, as can be observed in the scatter plots of Section 5.3.

RMSE is the square root of the variance of the residuals. It indicates the absolute measure of the fit of the model to the data – how close the model's predicted values (in this case, the pseudo reconstruction image) are of the observed data points (the full-POL image). This value is compared with the maximum of the amplitude value of the image Full-POL and the maximum of the amplitude of the pseudo reconstructions image.

Scatter plots, Regions of Interest (ROI) in the image, and 2-D H/α plane help to complement the evaluation. Graphical resources present in "ENVI" and "PolSARpro" computer programs are used in these analyses.

5. RESULTS

5.1. Dataset results

The Dataset of the L-band Full-POL image of the city of Oberpfaffenhofen, southern Germany, acquired by the E-SAR (DLR Airborne SAR System), in 2000, was chosen to evaluate the CP_{az} algorithm.

Follow the image parameters [47]:

a) Azimuthal dimension: 4000 samples (columns);

b) Radial dimension: 1580 samples (lines);

c) Spatial resolution: 3 x 3 meters; and

d) Pixel spacing: 2.5 x 2.5 meters.

This image presents several scattering mechanisms in the same dataset, as shown in Figure 5.8 by the 2-D H/α plane. Zone four (Z4 in Figure 5.8) is filled with red pixels that correspond to double-bounce scattering of the Gilching city located upper left in Figure 5.9 (b). Zone two (Z2) is filled entirely by green pixels that correspond to the volumetric scattering of the small wood lower left and upper right in Figure 5.9 (b). Zone nine (Z9), correspond to scattering from smooth surfaces (grass) located lower right in Figure 5.9 (b). The other scattering mechanisms, as vegetation layers and metal dihedral spreaders, also have significant representations in other zones [38], [40].

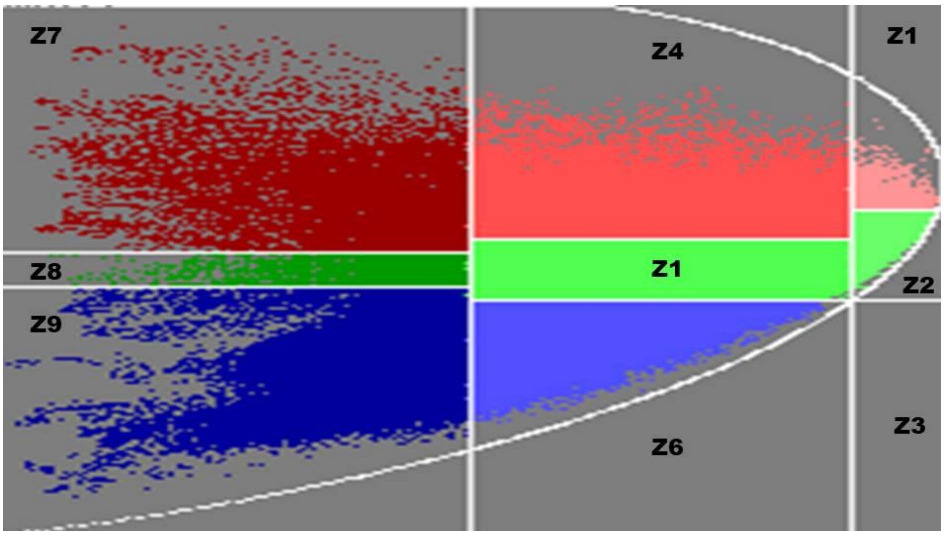

Figure 5.8 – E-SAR dataset distribution 2-D H/α plane.

Figure 5.9 (a) and (b) presents the RGB false-color composition and the optical image available in Google Earth, respectively, where in Figure (a) is assumed HH (blue), HV (red), and VV (green). This convention of a RGB false-color composition is considered from now on.

a) RGB E-SAR Composition.
b) Image from Google Earth.

Figure 5.9 – Dataset from Oberpfaffenhofen city, South Deutschland, acquired by E-SAR (*Airborne SAR System of DLR*), where the RGB false-color composition (a) considers HH (blue), HV (red), and VV (green).

The next step generates the amplitude of the images. The images HV and VH must be equivalents in a calibrated SAR system [47], considering the Reciprocity Theorem presented in Section 2.3 valid. This equivalence can be observed qualitatively in Figure 5.10

(b) and (c). Notice that white and black colors are predominant in these images. As examples, the volumetric scattering of the small wood located lower left and upper right in Figure 5.10 (b) and (c) is majority represented by the white color. In the surface scattering (grass) located lower right in the same Figure the black color predominates. In turn, the images HH and VV provide additional information about the scene, as can be verified in Figure 5.10 (a) and (d), respectively. The scattering now presents more details with the white and black colors substituted by shades of gray.

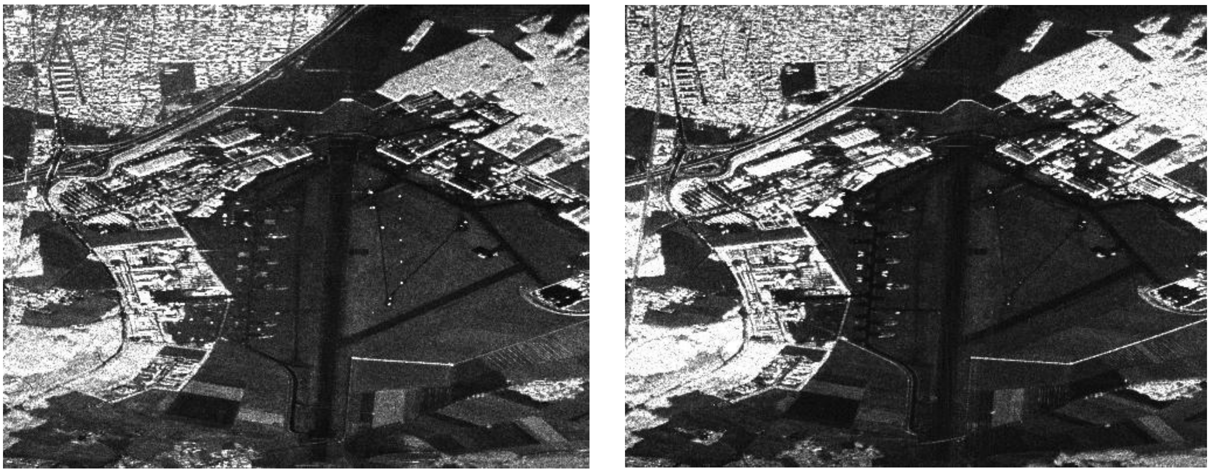

a) Image HH: $|S_{HH}|$. b) Image HV: $|S_{HV}|$.

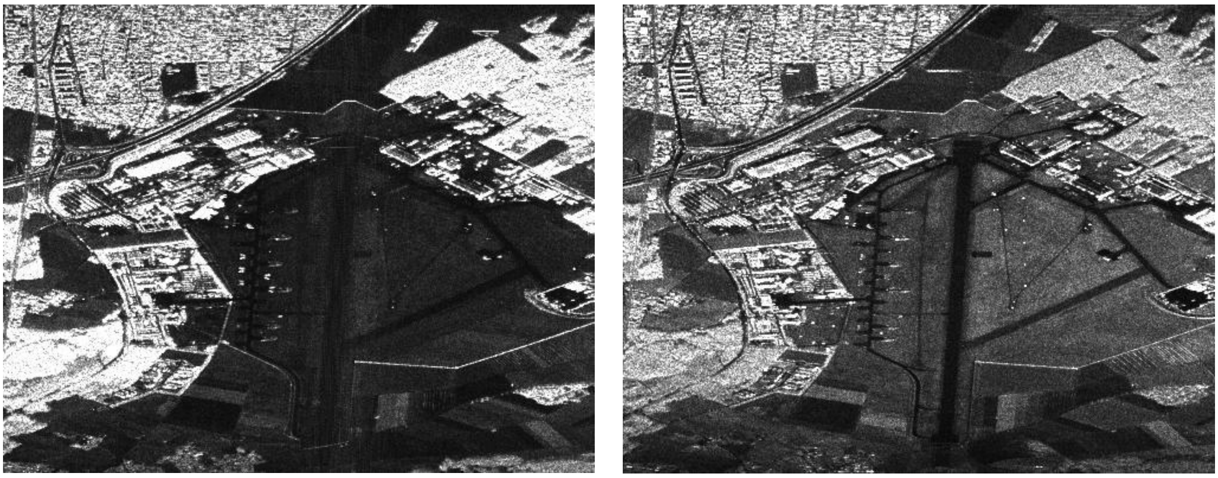

c) Image VH: $|S_{VH}|$. d) Image VV: $|S_{VV}|$.

Figure 5.10 –E-SAR polarimetric amplitude of the images.

Following the methodology, the entropy [38], [46] of the matrices C_{co-POL} (2.34), C_{cr-POL} (2.35), and C_{res} (2.36) was evaluated.

Figure 5.11 illustrates the calculated entropy values. As expected, the matrix with co-POL terms presents higher entropy values, as showed in Figure 5.11(a). The matrix with cross-POL terms presents low entropy, as illustrated in Figure 5.11(b). The matrix with residual terms had the entropy values near zero, as illustrated in Figure 5.11(c), which means that the matrix of residual terms may be disregarded in the next step of this work.

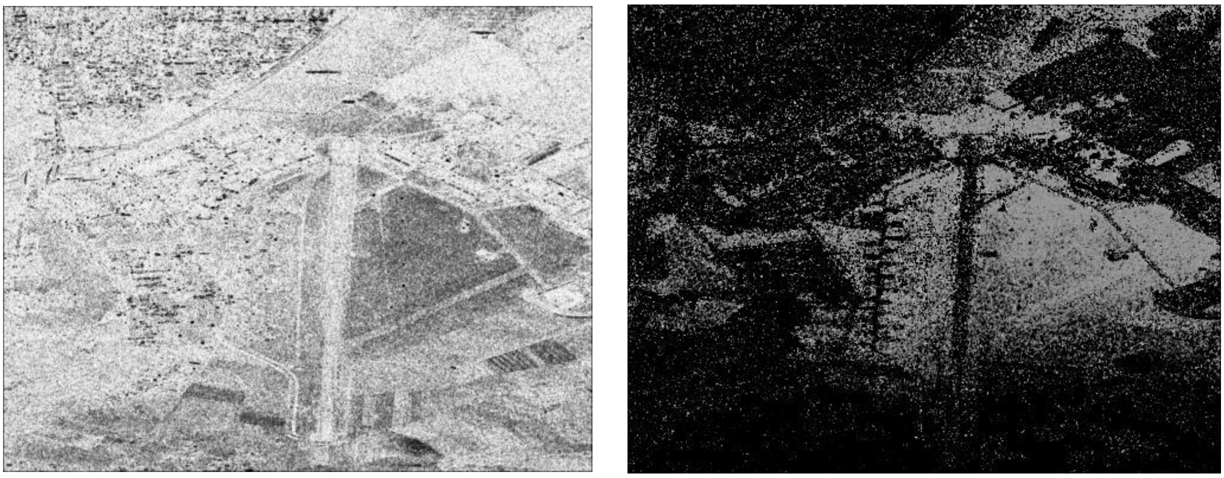

a) Entropy of the co-POL matrix C_{co-POL}.

b) Entropy of cross-POL matrix C_{cr-POL}.

c) Entropy of the residual matrix C_{res}.

Figure 5.11 – Entropy values of Covariance matrix C_{Rhc}.

5.2. Pseudo reconstruction process

Souyris, Nord, and CP_{az} algorithms result in non-linear system of equations that can be solved by an iterative process [6], [12], [51]. The iterative process is interrupted when the estimated value of X_{sr} varies by less than 1% between two consecutive iterations:

$$\text{Precision} = \left| \frac{X_{sr}(i) - X_{sr}(i-1)}{X_{sr}(i)} \right|, \tag{5.118}$$

where *i* is the number of iteration.

The stopping condition was reached after 21 iterations for this image. It must be observed that the iterative process is not well behaved, Figure 5.12. The oscillations continue with the same amplitude even after more than one hundred iterations. However, the number of iterations obtained in this work is compatible with the ones cited previously in the literature, such as in [12].

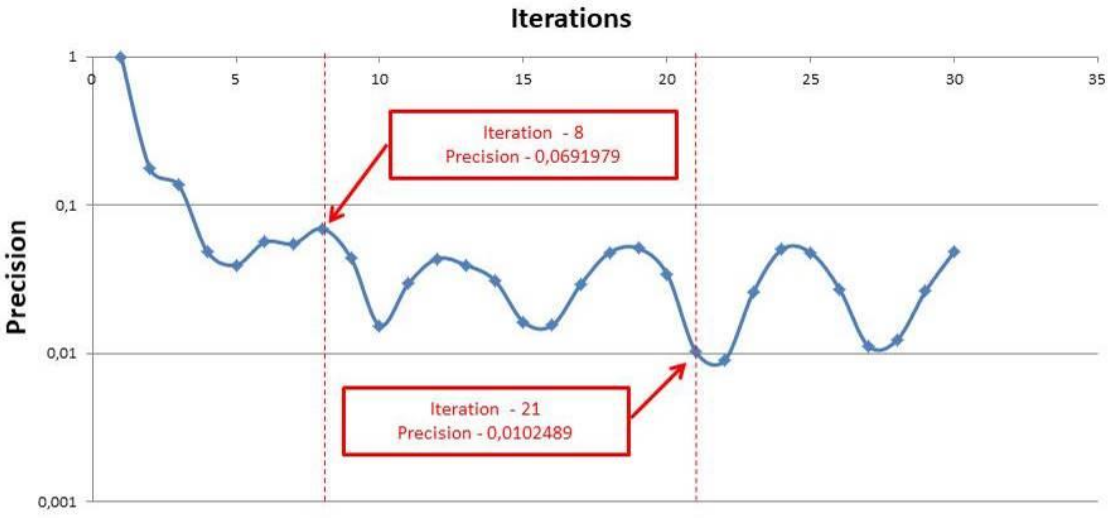

Figure 5.12 – Evolution of the iterative process.

The process of pseudo reconstruction using the three previously described algorithms, the Souyris, the Nord, and the CP_{az} ones, results in the images presented in Figure 5.13: (a) the E-SAR Full-POL image, (b) CP image generated by the Souyris algorithm, (c) CP image generated by the Nord algorithm, and (d) the CP image generated by CP_{az} algorithm with Faraday rotation angle $\Psi = 0°$. As mentioned before, the RGB false-color composition images assume HH (blue), HV (red), and VV (green).

Qualitatively, the comparison of the four amplitude images shows that the pseudo reconstruction images reproduce approximately the characteristics of the original Full-POL image. In Figure 5.13 (b), (c), and (d), we can observe the same boundaries and shapes present in Figure 5.13 (a).

The volumetric scattering at the lower left and upper right of Figure 5.13 (a) is represented with the predominance of the magenta color. The same areas in Figure 5.13 (b) (Souyris pseudo reconstruction), and Figure 5.13 (c) (Nord pseudo reconstruction) are represented by shades of red and green, respectively. The CP_{az} pseudo reconstruction (Figure 5.13 (d)) presents better results remaining the magenta color in the lower left of the image.

CP_{az} pseudo reconstruction (Figure 5.13 (d)) also presents better results comparing the surface scattering (grass) located lower right of the images. Figures 5.13 (a) and Figure 5.13 (d), Full-POL and CP_{az} pseudo reconstruction, respectively, presents shades of lighter green; while Figures 5.13 (b) and Figure 5.13 (c), Souyris and Nord pseudo reconstruction, respectively, present shades of darker green.

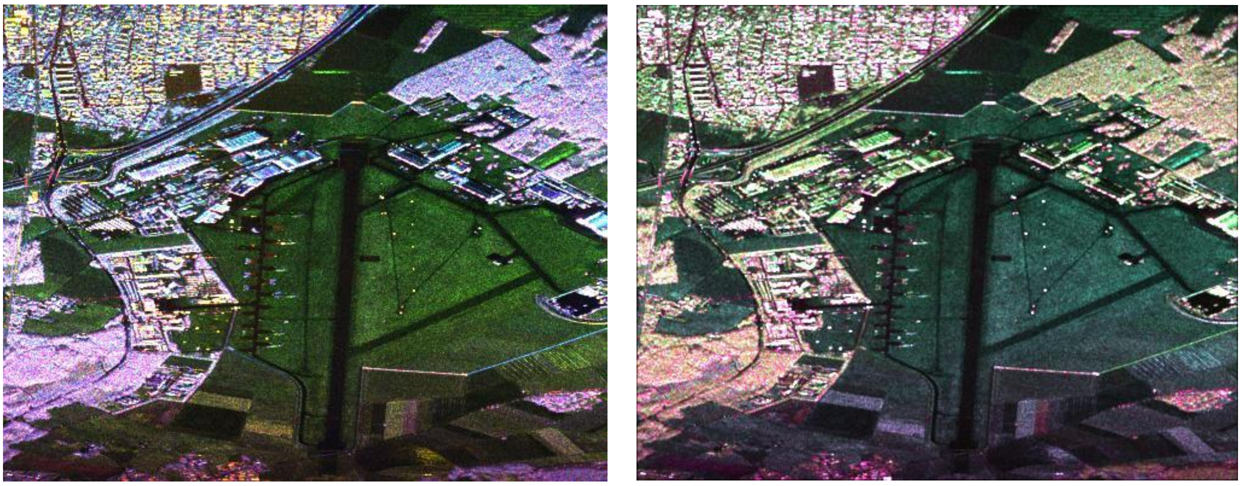

a) RGB E-SAR image.

b) RGB pseudo reconstruction by Souyris.

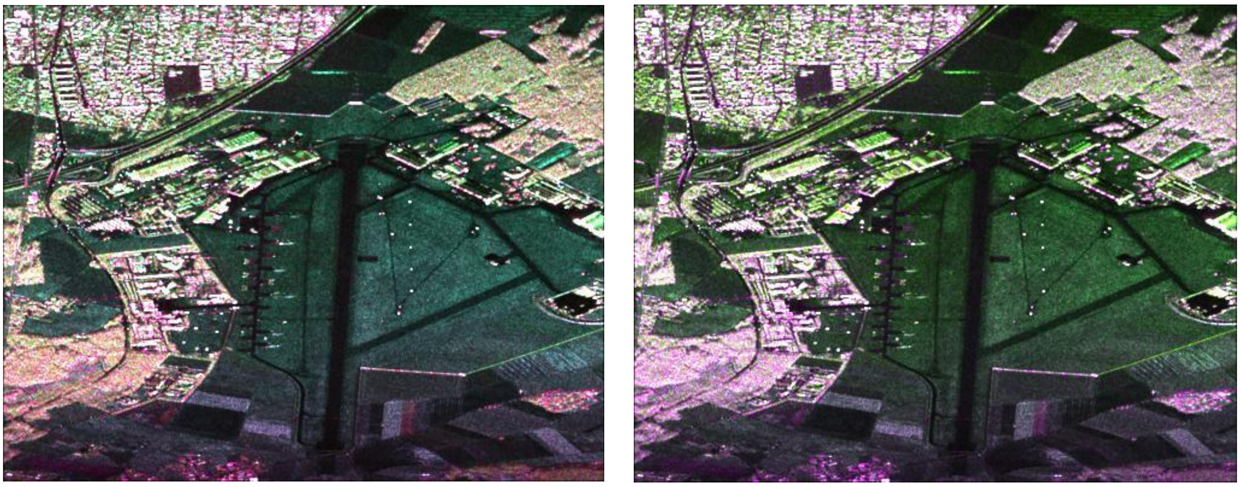

c) RGB pseudo reconstruction by Nord.

d) RGB pseudo reconstruction by CP_{az} algorithm.

Figure 5.13 – Comparison of the Full-POL image with the pseudo reconstruction by Souyris, Nord, and CP_{az} algorithm.

5.3. Compact Polarimetry algorithm analysis

The Pearson correlation coefficient and RMSE estimator are used for the image analysis. The results are presented in four tables (Appendix E). The first and second ones display the values obtained by the Pearson correlation coefficient and RMSE. The third table shows the maximum amplitude of the images, and the last table presents the RMSE percentage error, considering the corresponding maximum value of the pseudo reconstruction image.

The columns of these tables represent, respectively, the images HH (Mhh), HV (Mhv), and VV (Mvv) of the E-SAR system after the application of the Faraday rotation. In turn, the lines presented the pseudo reconstruction method considered.

Another resource used to evaluate the CP algorithm was the scatter plot. Using ENVI functions [55], E-SAR images were compared with pseudo reconstruction images generating figures with nine scatter plots (Appendix E). In the first line of these figures, E-SAR images HH, HV, and VV are compared with their respective images generated by the Souyris method. In the second line, E-SAR images are compare with the images generated by the Nord method, and in the third line, E-SAR images are compare with the images generated by CP_{az} algorithm. The red diagonal line present in all graphs indicates perfect correlation between images. Both graphic axes present values from 0 to 255. This range denotes the gray scale where the values close zero means pure black color, and values close to 255 means pure white color. Average values of 120 means medium gray color. The concentration of the pixels is distributed in green, blue, and purple colors, where green indicates a high percentage of concentration of pixels; blue indicates a medium concentration of pixels; and purple indicates lower concentration of the pixels in the image. Most scatter plots present green color close to the range 0-100, which means that the image considered has a high concentration of dark gray, as can be observed in the amplitude images presented in Figure 5.10.

Finally, the amplitude of the images was presented as an illustration of the Faraday rotation effect (Appendix E). The presentation of these images allows identifying the predominant channel in the respective scene, observing the colors that stand out in the pictures.

5.3.1. The Faraday rotation effect over the CP algorithm

The Pearson parameters shows that the components co-POL (HH and VV) behave differently as Faraday rotation angle Ψ increases. Channel HH of the pseudo reconstruction images keeps better correlation with the E-SAR images until $\Psi = 20^o$, when it starts to decreases. The same behavior can be observed for channel VV of the pseudo reconstruction images, where the decrease of the correlation with the E-SAR images starts to happen when $\Psi = 10^o$. In the opposite way, the correlation of the channel HV increases until $\Psi = 40^o$. Figure 5.14 illustrates the relationship between the Pearson correlation coefficient and the Faraday rotation angle.

If Ψ continues to increase, the correlation at $\Psi = 90^o$ back to the same levels of correlation obtained for $\Psi = 0^o$.

In turn, the colors of the images of amplitude of the pseudo reconstruction methods (Appendix E) start to fade as Faraday rotation angle Ψ increases. The result is an image with shades of gray (Figure E.37) instead of three channels red, green, and blue when $\Psi = 40^o$.

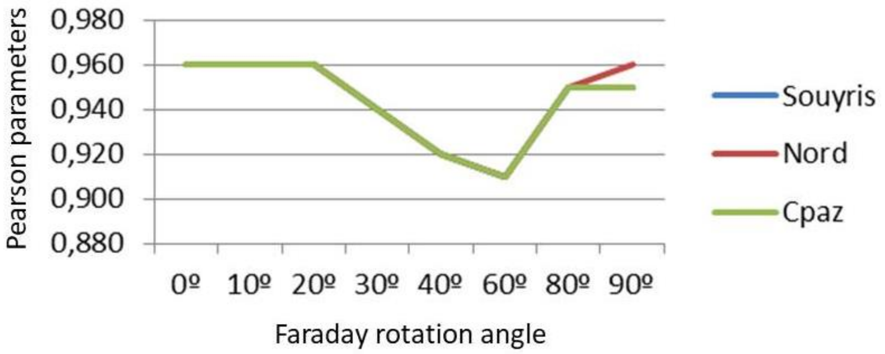

a) Channel HH.

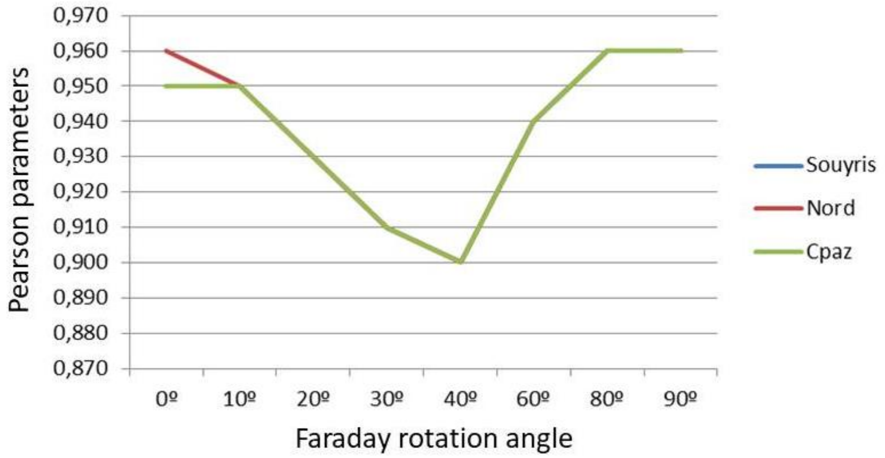

b) Channel VV.

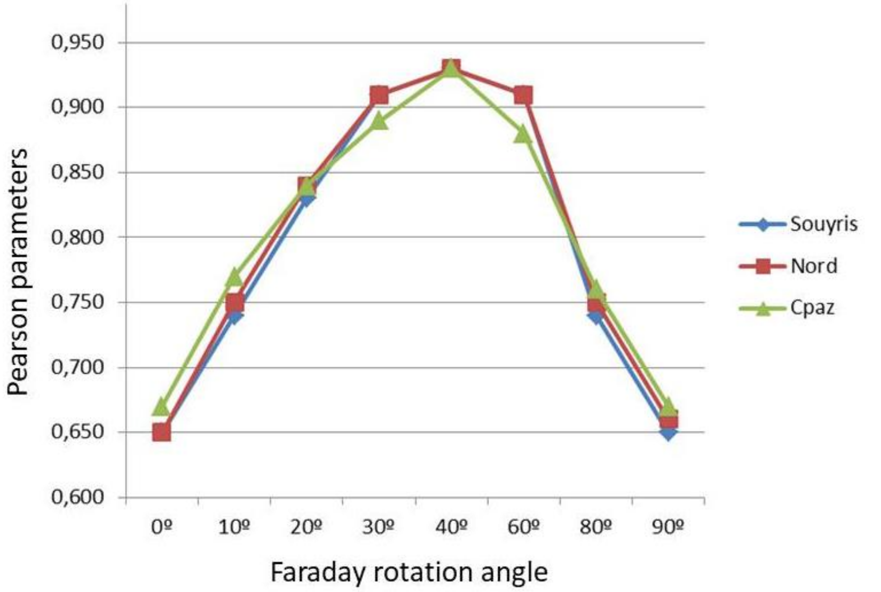

c) Channel HV.

Figure 5.14 – Behavior of the co-POL and cross-POL components, considering the Pearson parameters.

The physical interpretation of this phenomenon can be obtained observing the CP process. The Matrices presented in equation (3.48) are the base of the equations that belong to the initialization and the iteration of the pseudo reconstruction method.

Under the Faraday rotation effect, the matrices S_{HH}, S_{HV}, and S_{VV} are substituted by the matrices M_{HH}, M_{HV}, and M_{VV} (equation B.19). In the sequence, the iteration process updates the value of X_{sr} (3.52), which matrix will suffer the effects of Ψ through the rotated M matrices.

$$\begin{aligned}
2C_{cp11} &= \left\langle |M_{HH}|^2 \right\rangle + \left\langle |M_{HV}|^2 \right\rangle \\
2C_{cp12} &= j\left\langle M_{HH} M_{VV}^* \right\rangle - j\left\langle |M_{HV}|^2 \right\rangle \\
2C_{cp21} &= -j\left\langle M_{VV} M_{HH}^* \right\rangle + j\left\langle |M_{HV}|^2 \right\rangle \\
2C_{cp22} &= \left\langle |M_{VV}|^2 \right\rangle + \left\langle |M_{HV}|^2 \right\rangle,
\end{aligned} \tag{3.48}$$

$$X_{sr}^{(n)} = \left(C_{cp11} + C_{cp22}\right) \frac{\left|(1-\rho_{HH-VV})\right|}{\left|(3-\rho_{HH-VV})\right|}. \tag{3.52}$$

Finally, the third step of the pseudo reconstruction methodology (3.54) uses the matrices of C_{cp} and X_{sr} to generate the pseudo images $\left\langle |S_{HH}|^2 \right\rangle$ (channel HH), $\left\langle S_{HH} S_{VV}^* \right\rangle$ (channel HV), and $\left\langle |S_{VV}|^2 \right\rangle$ (channel VV). Therefore, if C_{cp} and X_{sr} are rotated by Ψ, the generated channels also will be.

$$\begin{aligned}
\left\langle |S_{HH}|^2 \right\rangle &= 2C_{cp11} - X_{sr} \\
\left\langle S_{HH} S_{VV}^* \right\rangle &= -j2C_{cp12} + X_{sr} \\
\left\langle |S_{VV}|^2 \right\rangle &= 2C_{cp22} - X_{sr}.
\end{aligned} \tag{3.54}$$

Pearson parameters help us to understand the physical effects produced by the CP methodology under the Faraday rotation effect.

Figure 5.15 illustrates the Faraday rotation effect over the channels of the E-SAR image (blue shade vectors) and over the channels of the CP algorithm (red shade vectors).

When $\Psi = 0^{\circ}$, the E-SAR images and CP images have high correlation and the vectors of the correspondent channels are close to each other. Under Faraday rotation, each channel of the E-SAR system turns to the right, observing the same value of Ψ. On the other hand, the components of the CP process changes the direction differently, as far as Ψ increases to 40º. This effect over the HH and VV channels of the CP method makes these channels to increase the correlation with the HV channel of the E-SAR image instead to increase the correlation with their respective E-SAR channels. In turn, the HV channel increases the correlation with the HV channel of the E-SAR image, as expected.

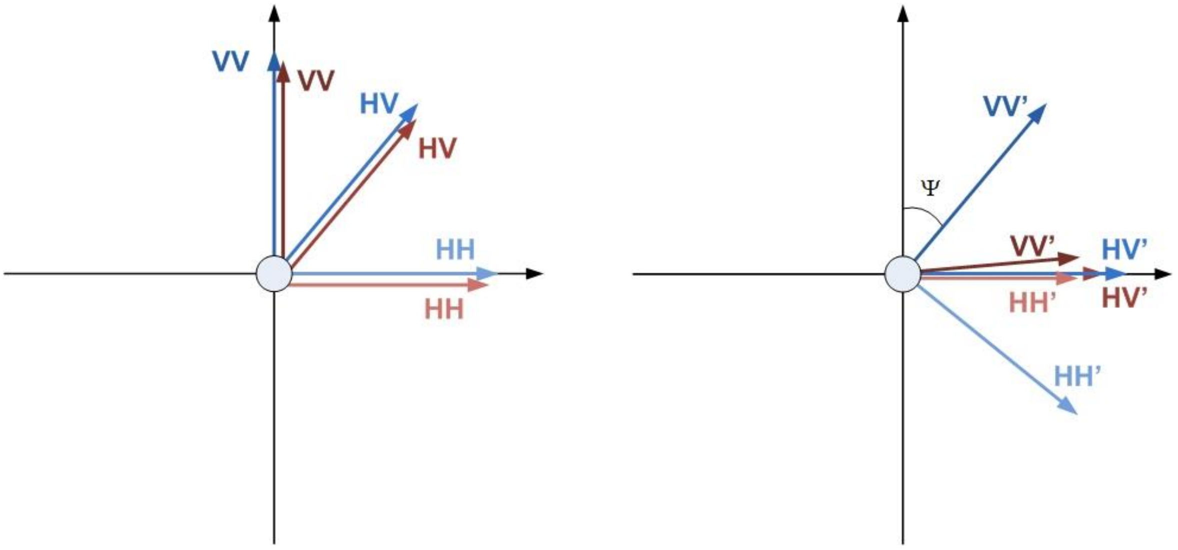

a) $\Psi = 0^{\circ}$. b) $\Psi = 40^{\circ}$.

Figure 5.15 – Faraday rotation effect over the channels of the E-SAR image (blue shade vectors) and over the channels of the CP_{az} algorithm (red shade vectors).

The effect presented in Figure 5.15 (b) over the pseudo reconstruction channels can be also demonstrated using scatter plots. Figures 5.16 (a) and (b) shows the correlation of the channel VV with the channel HH and channel HV, respectively. It can be observed that the correlation is almost the same in both Figures. And Figure 5.16 (c) shows the correlation between the pseudo reconstruction channel HH and HV. In this case, the pixels are concentrated close to the red line, which indicates that the channels have a high correlation.

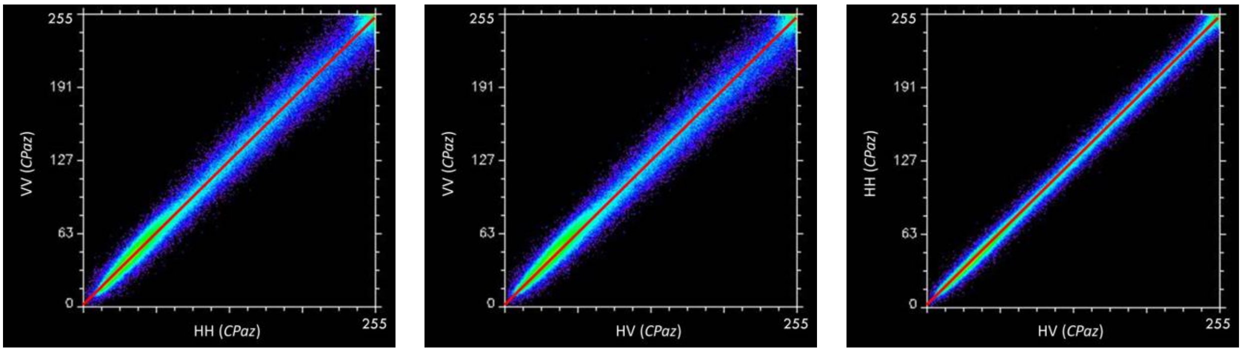

a) Correlation between VV and HH channels.

b) Correlation between VV and HV channels.

c) Correlation between HH and HV Channels.

Figure 5.16 – Correlation between channels of CP_{az} algorithm when $\Psi = 40^{o}$.

Hence, the first analysis of correlation between the images concludes that CP algorithms suffer alterations when subject to the Faraday rotation effect. As Ψ increases, CP channels rotate observing the same behavior of the Full-POL channels. Close to $\Psi = 40^{o}$, CP channels overlap and the RGB false color composition presents shades gray. The phenomenon is cyclical, as demonstrated in Figure 5.14.

5.3.2. CP_{az} performance

The analysis performed using statistic parameters, scatter plots and figures of the amplitude of the images shows that CP_{az} algorithm presents better results than others methods of pseudo reconstructions, even under Faraday rotation effect.

The better result of CP_{az} algorithm can be also observed in Figures E.28, E.30, and E.32. The scatter plot of channel HV of the CP_{az} image (center of the third line in Figure E.28) shows that most pixels are concentrated close to the red line, while equivalent scatter plot for Souyris (center of the first line in Figure E.28) presents the green and blue pixels farthest of the red line, and the equivalent scatter plot for Nord (center of the second line in Figure E.28) all the pixels are more spread out in the graph. Pearson statistics presented in Figure 5.14 (c) confirms this result from $\Psi = 0^{o}$ to $\Psi = 20^{o}$.

With regard to the RMSE statistics (Tables E.3 to E.7), the errors of the CP_{az} method are similar to the other methods. It was observed that channel HH presented error about 0.01; channel HV presented errors about 0.03; and channel VV presented errors close to 0.03.

The description of Figure 5.13 (Section 5.2) also highlighted the better results of CP_{az} algorithm over other CP methods. Shades of magenta color in the lower left and shades of lighter green in the lower right of the CP image are very similar to the E-SAR image. As Ψ increases, the differences between the images are only observed with the use of statistics.

5.3.3. Correlation observing Regions of Interest (ROI)

The analysis of regions in the image where specific scattering mechanisms are prominent, given us additional information to evaluate the algorithms. Figure 5.17 illustrates areas in the Google Earth image with a predominance of characteristics that can be associated with a specific scattering mechanism.

Figure 5.17 – Google Earth image of the city of Oberpfaffenhofen (Germany).

Figure 5.18 shows the selected ROIs. The upper red square (ROI 1) corresponds to a city with human-made buildings in which the primary scattering mechanism is the double-bouncing. The ROI in the lower left of Figure 5.18 (ROI 2) corresponds to a small wood located on the Münchener street margins, providing some volumetric scattering. The third area selected (ROI 3), located on the right side of the image, have mainly grass, in which the main scattering mechanism is the surface one.

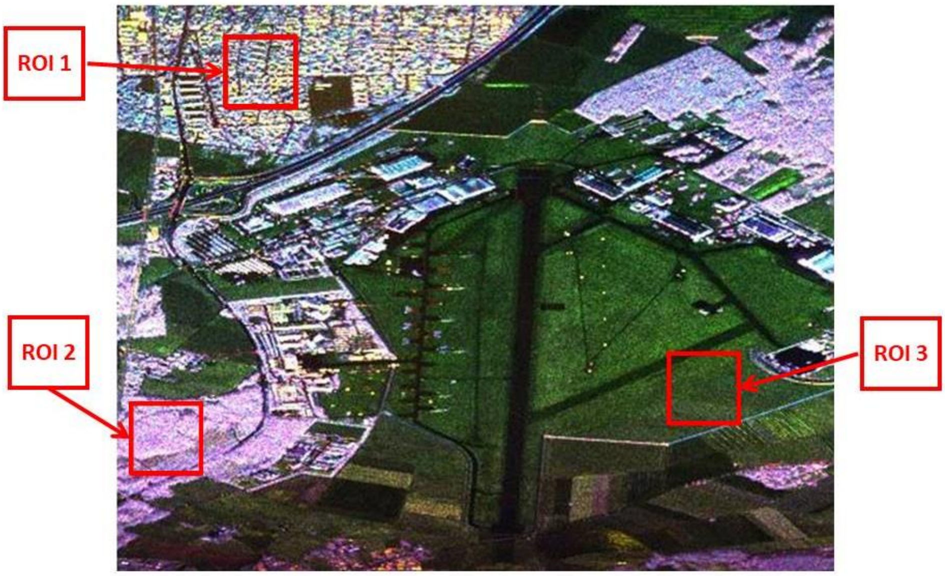

Figure 5.18 – Selection of ROIs containing examples of double-bounce scattering (ROI 1-Gilching city – upper left), volumetric scattering (ROI -2 - a small wood - lower left), and surface scattering (ROI 3 - grass – lower right).

The Pearson parameter is used to evaluate the performance of the three pseudo reconstruction algorithms, Souyris, Nord, and CP_{az} , in the three ROIs.

Figure 5.19 presents how it behaves the co-POL and cross-POL components, considering the Pearson parameters of Region of Interest 1 (ROI 1), double-bounce.

In Figure 5.19 (a) It can be observed that green line related to the CP_{az} algorithm presents higher values for Faraday rotation angles between 0^{o} and 30^{o}, which means better performance of the proposed algorithm for double-bounce samples at HH channel. The same result can be observed in Figure 5.19 (b) at channel VV, where the CP_{az} algorithm has a better performance compared with the other methods. Figure 5.19 (c) presents the channel HV, where effectively the CP_{az} algorithm stands out from the other methods, considering double-bounce scenarios.

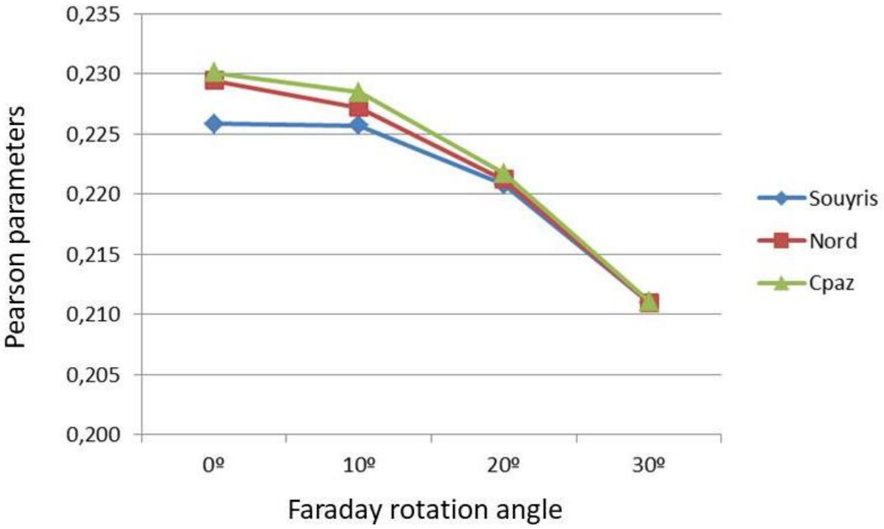

a) ROI 1 – Channel HH – CP Methods x E-SAR.

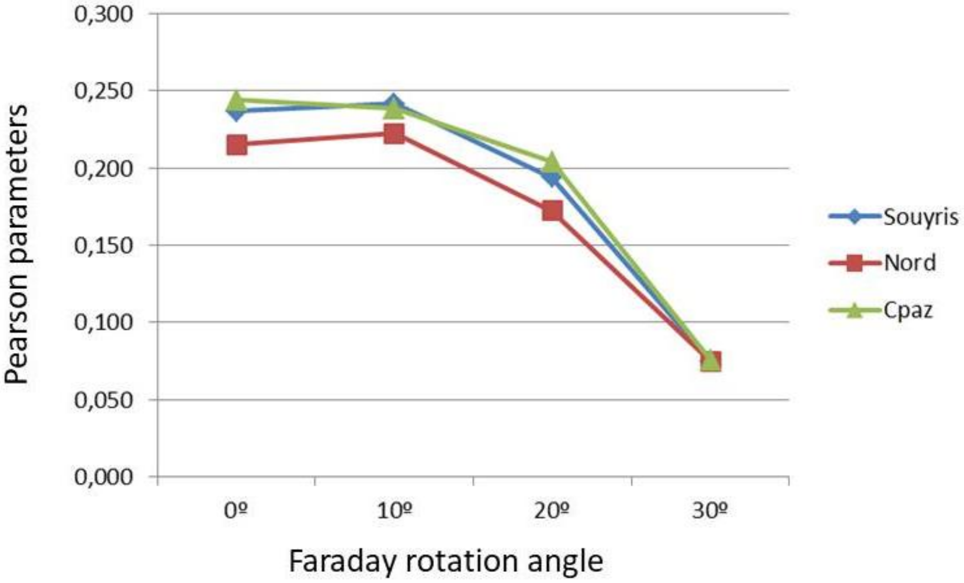

b) ROI 1 – Channel VV – CP Methods x E-SAR.

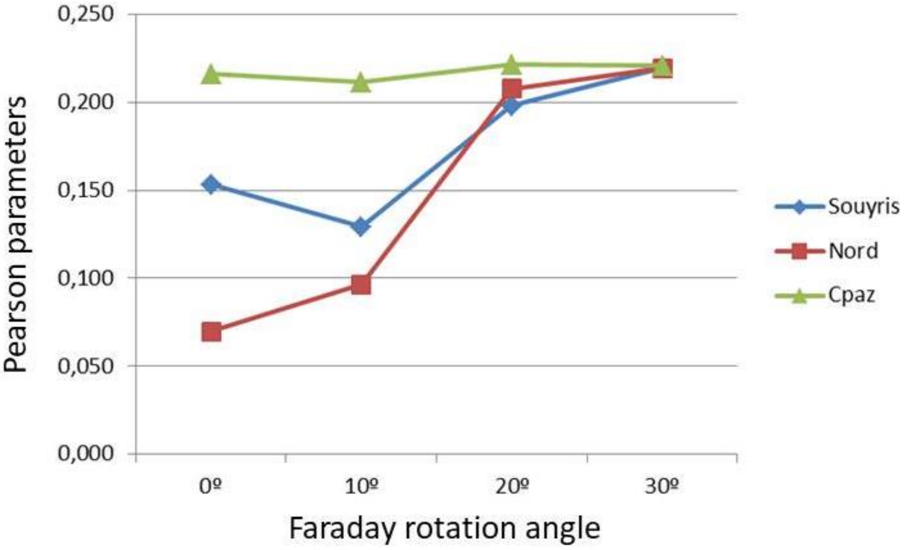

a) ROI 1 – Channel HV – CP Methods x E-SAR.

Figure 5.19 – Behavior of the co-POL and cross-POL components, considering the Pearson parameters of Region of Interest 1 (ROI 1), double-bounce.

Considering ROI 2, where there is the predominance of volumetric scattering, it can be observed in Figures 5.20 (a) and (b) that Souyris and the CP_{az} algorithm (the line blue and the line green, respectively) present similar results. However, at $\Psi = 30^{o}$, in channel HH, the proposed algorithm stands out over the other pseudo reconstruction algorithm. At channel HV, the CP_{az} algorithm presents better results when $\Psi = 0^{\circ}$.

Figure 5.21 presents how it behaves the pseudo reconstruction algorithms, considering the Pearson parameters of Region of Interest 3 (ROI 3), surface scattering.

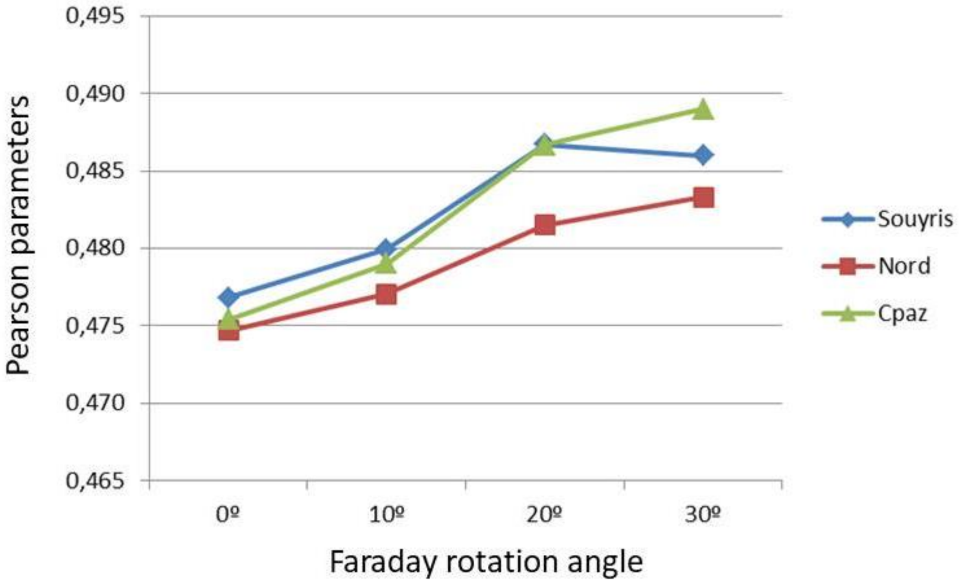

a) ROI 2 – Channel HH – CP Methods x E-SAR.

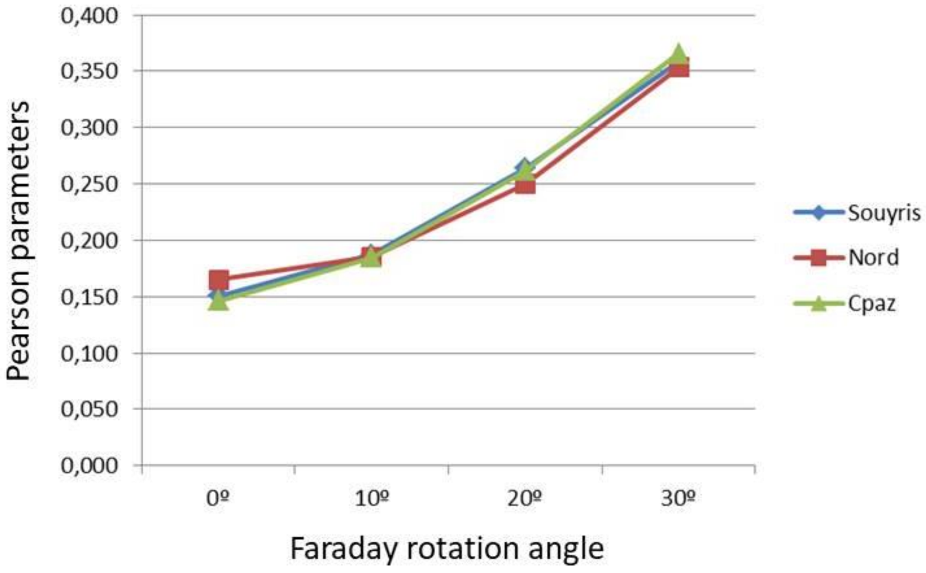

b) ROI 2 – Channel VV – CP Methods x E-SAR.

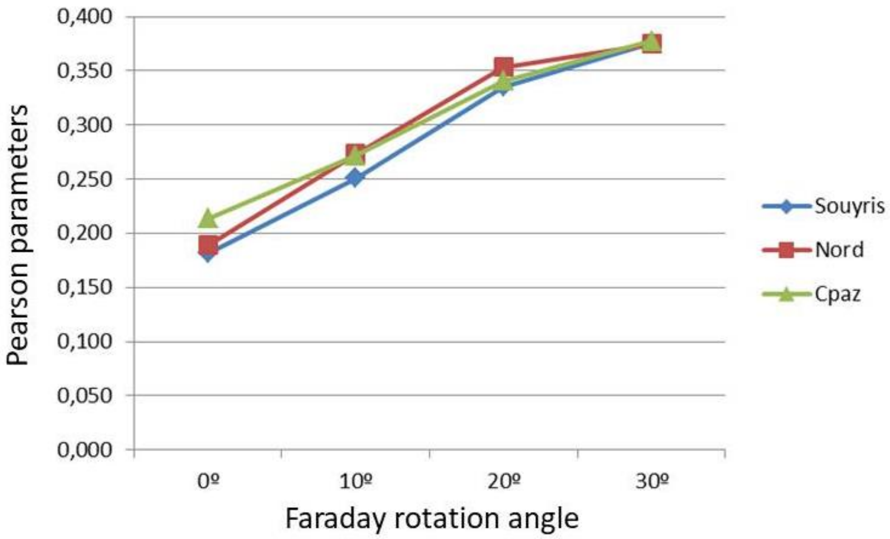

c) ROI 2 – Channel HV – CP Methods x E-SAR.

Figure 5.20 – Behavior of the co-POL and cross-POL components, considering the Pearson parameters of Region of Interest 2 (ROI 2), volumetric scattering.

With the predominance of surface scattering, the CP_{az} algorithm presents better results over the other methods of pseudo reconstruction at channels HH and VV, as presented in Figures 5.21 (a) and (b). In the case of channel HV (Figure 5.21 (c)), the CP_{az} algorithm presents similar results with Nord algorithm, and better results with Souyris algorithm, for the dataset considered.

Figure 5.22 presents same examples of scatter plots in order to illustrate the behave of the co-POL and cross-POL components, just considering the correlation between Souyris and the CP_{az} method.

The left image of the first line of the Figure 5.22 is a RGB false-compositions of E-SAR ROI 1 (double-bounce) image, follow by the scatter plots of the channel HH, at $\Psi = 0^{o}$. It can be observed that pixels of CP_{az} algorithm are closer to the red line than Souyris scatter plot, which means better performance of the proposed algorithm for double-bounce samples at HH channel.

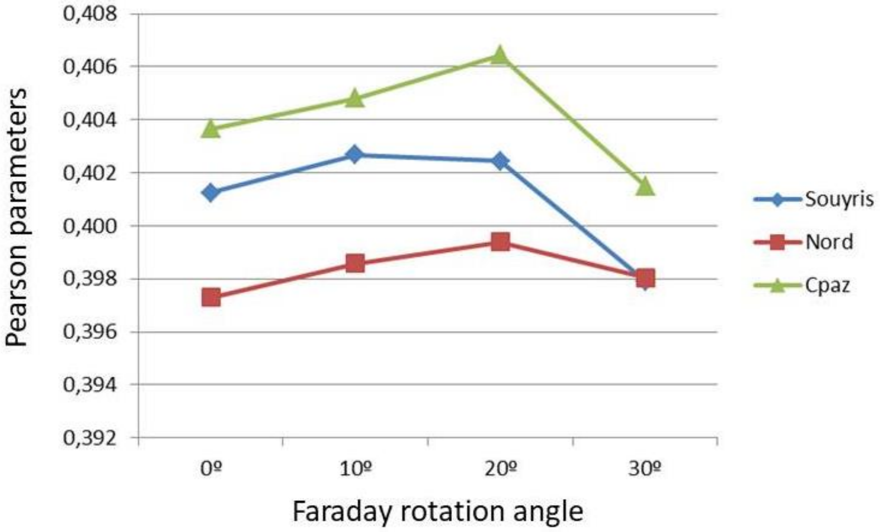

a) ROI 3 – Channel HH – CP Methods x E-SAR.

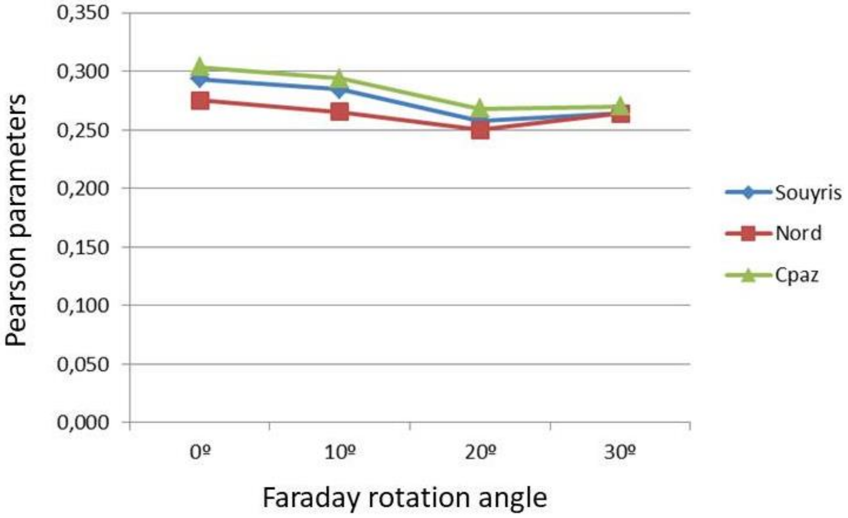

b) ROI 3 – Channel VV – CP Methods x E-SAR.

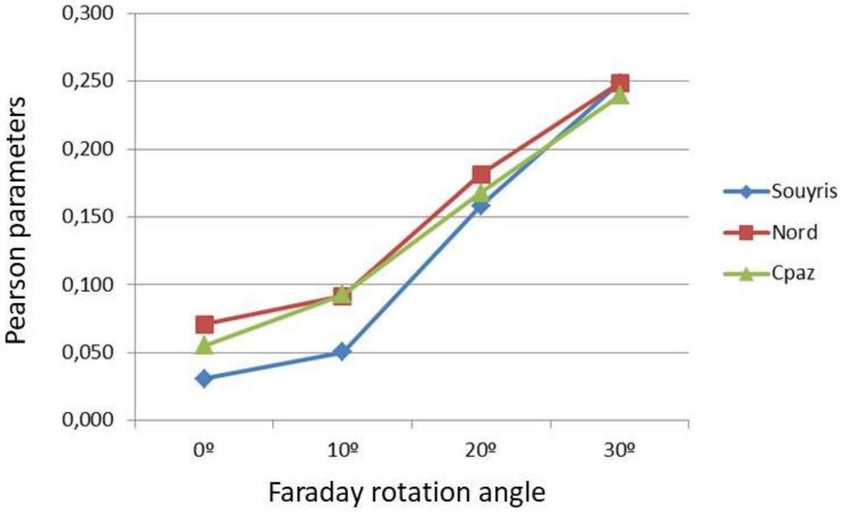

c) ROI 3 – Channel HV – CP Methods x E-SAR.

Figure 5.21 – Behavior of the co-POL and cross-POL components, considering the Pearson parameters of Region of Interest 3 (ROI 3), surface scattering.

The second line presents the scatter plots of the channel HV related to the volumetric scattering ROI. In this case, it can be observed that pixels of CP_{az} algorithm are distributed around the red line while the pixels of Souyris scatter plot are concentrated below the red line. Once again, the CP_{az} algorithm presents better performance than Souyris method.

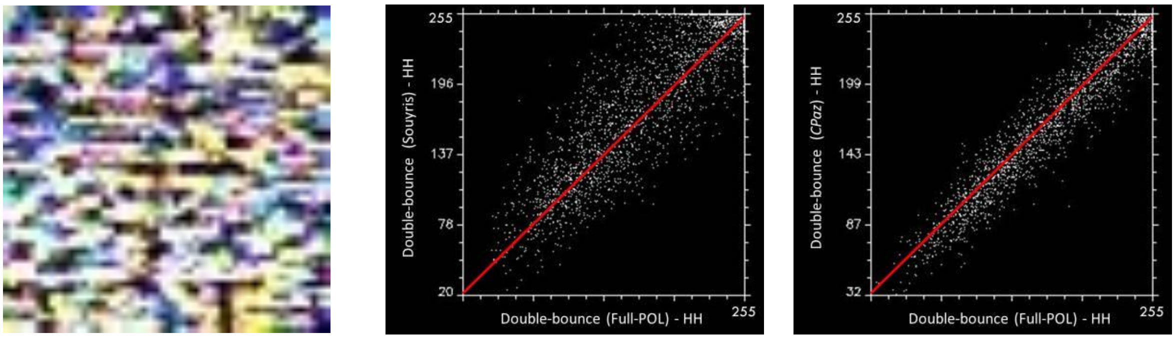

E-SAR RGB
(ROI 1 - Double-bounce)

(HH) E-SAR x Souyris

(HH) E-SAR x CP_{az}

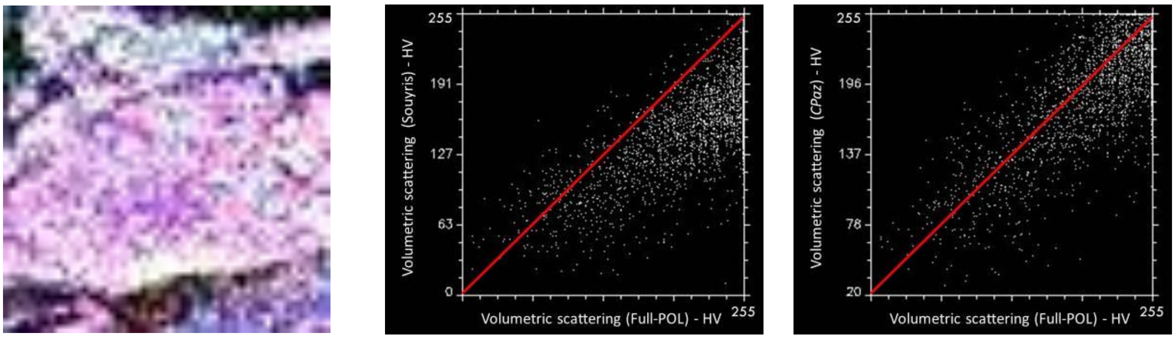

E-SAR RGB
(ROI 2 - Volumetric)

(HV) E-SAR x Souyris

(HV) E-SAR x CP_{az}

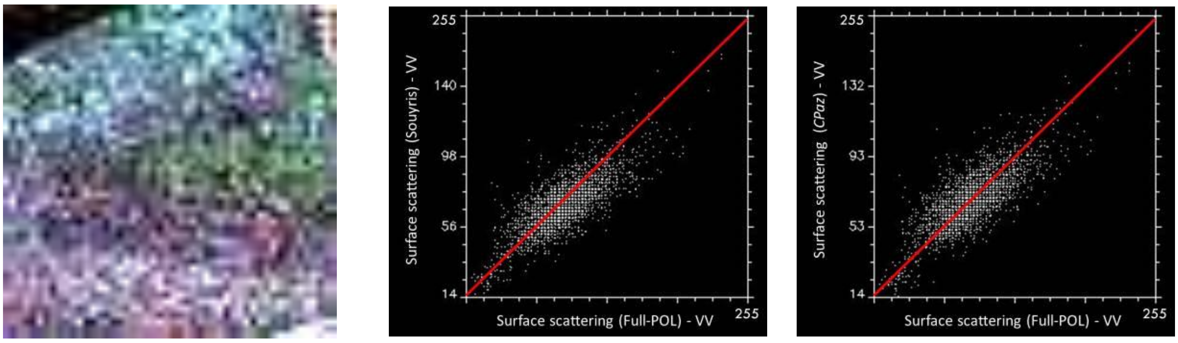

E-SAR RGB
(ROI 3 - Surface)

(VV) E-SAR x Souyris

(VV) E-SAR x CP_{az}

Figure 5.22 – CP_{az} algorithm and Souyris method comparison with the use of the Regions of Interest (ROI). The graphics were elaborated in the ENVI computational program [55].

The third line presents the scatter plots of the channel VV related to the surface scattering – ROI 3. In this case, both algorithms show closer results, with a slightly better performance of the CP_{az} algorithm.

This subsection closes this work and reinforces the concept that in the presence of Faraday rotation and other effects of the Ionosphere, there is a need to employ a specific Compact Polarimetry algorithm, in order to obtain better results in the pseudo reconstruction of the images.

6. CONCLUSIONS AND FUTURE WORK

6.1. Final considerations

This Thesis has explored a new approach for the Compact Polarimetry (CP), considering the use of the L band and a geophysical medium with azimuth symmetry properties.

The use of compact polarimetry is not yet unanimous in the scientific world. Some researchers use to say that the pseudo reconstructions methods are not able to collect all the information present in the scene. Indeed, this affirmative is correct if you have a complex spaceborne SAR system able to provide Full-POL resources.

However, observing the tendency of mass reduction and simplification of space systems, the CP could be an alternative to the high potential of application in the future. The technique allows reconstructing a pseudo Full-POL image from a simplified system with a similar quality of the image generated by complex space systems.

Considering that Brazil is an immense country, with six large continental biomes, a vast oceanic area that comprises about 10 million square kilometers, and counting with a limited budget for space activities, a micro satellite with CP resources presents as an attractive low cost as an attractive low-cost alternative to provide quality data and information on deforestation, forest fires, oil spills at sea, illicit border actions, slides, floods, to support precision agriculture, among other occurrences and strategic information.

In this context, this work presents the basic concepts of the CP and proposes a new approach for the CP pseudo reconstruction method, in order to provide subsidies for the future feasibility studies of Brazilian SAR satellite missions.

6.2. Contributions

On the CP algorithms developed until now has been considered appropriated simplifications for scenarios in Europa and North America. In this case, the CP models adopted in previous work have been considered geophysical media with reflection symmetry properties. However, the literature lacks studies appropriate to the vast and complex Brazilian scenarios, where the azimuthal symmetry is more relevant. The algorithm introduced in this Thesis has the potential to fill up this gap in the literature and provide new perspectives for Brazilian spaceborne SAR systems. This is the main contribution of this Thesis.

The first analysis conducted in this Thesis considers Pearson parameters to evaluate the behavior of the CP algorithms in the presence of Faraday rotation effects. This parameters shows how the Faraday rotation effects affects CP algorithms. As the Faraday rotation angle increases, channels HH, HV, and VV of the pseudo reconstructions image rotate observing the same behavior of the Full-POL channels. Close to Faraday rotation angle of 40º, the CP channels HH and VV overlap over the channel HV and the RGB false-color composition of the pseudo reconstruction image presents shades gray. The analyses also demonstrate that this effect is cyclical with the overlap of the CP channels at each 90º of Faraday rotation.

This finding is an important issue to consider when choosing the band of the SAR space system. The Faraday rotation can significantly affect the transmissions of the lower frequencies. Low frequencies are an interesting alternative because of the penetration of the microwaves in the scenario, but the Faraday rotation could deteriorate the CP pseudo reconstruction process.

The second analysis was performed using Pearson's correlation coefficient, Root Mean Square Error (RMSE), and scatter plots to evaluate the pseudo reconstruction process regarding the original Quad-POL images.

The analysis shows that CP_{az} algorithm presents better results than the other methods of pseudo reconstructions considered in this work, even under Faraday rotation effect. The better result of CP_{az} algorithm was observed with the channel HV, where the CP images obtained better correlations with the original E-SAR. The CP_{az} algorithm also had better results than the other methods for Faraday rotation angles between 0º and 30º.

For the third analysis, it was considered three areas of the dataset that have the predominance of double-bounce scattering, volumetric scattering, and surface scattering.

For the double-bounce scattering, the analysis based on the correlation of the scatter plots and the Pearson parameter shows that CP_{az} algorithm presents better results compared to the other pseudo reconstructions at the HV channel. For volumetric scattering, the results of the three algorithms are similar. The best result is observed in channel HH for the Faraday rotation angle of 30º. And for surface scattering, the CP_{az} algorithm presents better results on channel HH.

The results of this work reinforce the concept that in the presence of Faraday rotation and other effects of the Ionosphere, there is a need to employ a specific Compact Polarimetry algorithm, to obtain better results in the pseudo reconstruction of the images. Hence, the azimuthal symmetry must be considered.

6.3. Future works

Some specific suggestions for future works involve:

a) The use of other datasets with only volumetric scattering in order to make additional tests and analysis on the use CP_{az} algorithm.

b) The use of Brazilian datasets can provide several information that was not explored in this preliminary work. It could be an interesting approach for academic research or for operational applications by the Brazilian Center of Space Operations (COPE – Centro de Operações Espaciais).

c) The analysis of Oceanic areas is also important to allow monitoring oil spills at sea and must be explored with the CP methods.

d) This list does not end the possibility of the complementary studies using the algorithm.

There is no doubt about the prospective scenario on the use of the CP in the future spaceborne SAR literature and applications. The author is confident that this technology will be consolidated in the space missions of the future.

REFERENCES

[1] INSTITUTO BRASILEIRO DE GEOGRAFIA E ESTATÍSTICA. *Mapa de biomas e de vegetação do Brasil*. Rio de Janeiro: IBGE, 2004. Available: https://www.ibge.gov.br/. Accessed: 14-Sep-2019.

[2] MIRANDA, E. E. de; FONSECA, M. F. *Considerações fitogeográficas e históricas sobre o bioma cerrado no Estado de São Paulo*. Campinas: GIDE, EMBRAPA, 2013. (Notas Técnica 1).

[3] LARSON, W. J.; WERTZ, J. R.. *Space mission analysis and design.* 3th ed. Dordrecht: Microcosm Press, 2005.

[4] CHRISTOPHERSON, J. B.; CHANDRA, S. N. R.; QUANBECK, J. Q. *2019 Joint Agency Commercial imagery* evaluation:land remote sensing satellite compendium. Sioux Falls: U. S. Geological Survey, U.S. Department of the Interior, 2019. (Geological Survey Circular 1455).

[5] NGHIEM, S. V. *et al*. Symmetry properties in polarimetric remote sensing. *Radio Sci.*, v. 27, n. 5, p. 693–711, 1992.

[6] SOUYRIS, J. C. *et al*. Compact polarimetry based on symmetry properties of geophysical media: The π/4 mode. *IEEE Trans. Geosci. Remote Sens.*, v. 43, n. 3, p. 634–645, 2005.

[7] NORD, M. E. *et al*. Comparison of compact polarimetric synthetic aperture radar modes. *IEEE Trans. Geosci. Remote Sens.*, v. 47, n. 1, p. 174–188, 2009.

[8] LAVALLE, M. *Full and compact polarimetric radar interferometry for vegetation remote sensing*. 2010. 196 p. Thése (Docteur em Image et Télédétectio) -Institut d’Electronique et de Télécommunications de Rennes, l’Université Européenne de Bretagne Rennes, 2010.

[9] PANIGRAHI, R. K. *Information extraction from polarimetric SAR images*. 2011. 153 p. Thesis (Doctor of Philosophy) -Department of Electronics and Electrical Engineering, Indian Institute of Technology Guwahati, Guwahati, 2011.

[10] TRUONG-LOÏ, M.-L. *Potentiels d’un système RSO basse fréquence opérant en polarimétrie compacte.* 2010. Thése (Docteur em Image et Télédétection Structure et Propriétés de la Matière) -Institut d’Electronique et de Télécommunications de Rennes, l’Université Européenne de Bretagne Rennes, 2011.

[11] SHIRVANY, R., M.; CHABERT, M.; TOURNERET, J.-Y Comparison of ship detection performance based on the degree of polarization in hybrid/compact and linear dual-pol SAR imagery. *In*: IEEE INT. GEOSCI. REMOTE SENS. SYMP., 2011, Vancouver. *Proceedings* […] Piscataway: IEEE, 2011. p. 3550–3553.

[12] DENBINA, M. *Iceberg detection using compact polarimetric synthetic aperture radar*. 2014. Thesis (PhD) - University of Calgary, Calgary., 2014.

[13] PAES, R. L. *Detecção de Alvos no mar em imagens SAR explorando recursos da polarimetria compacta em modo híbrido*. 2015. 137 f. Tese (Doutorado em Sensoriamento Remoto) - Instituto Nacional de Pesquisas Espaciais, São José dos Campos, 2015.

[14] FIGUEIREDO C. A. *et al*. Medium-scale traveling ionospheric disturbances observed by detrended total electron content maps over Brazil. *J. Geophys. Res. Sp. Phys.*, v. 123, n. 3, p. 2215–2227, 2018.

[15] YOUNIS, M. *et al*. High performance reflector-based synthetic aperture radar -a system performance analysis. *In*: INTERNATIONAL RADAR SYMPOSIUM, 11., 2010. *Proceedings* […] [*S. l.*: *s. n.*], 2010. p. 1–4.

[16] SATELLITE Missions Database. Earth observation missions. [*S. l.*]: eoPortal Directory, ESA, 2019.Available: https://directory.eoportal.org/web/eoportal/satellite-missions.[Accessed: 16-Oct-2019.

[17] MOREIRA, A. *et al*. A tutorial on synthetic aperture radar. *IEEE Geoscience and Remote Sensing Magazine,* v.1, n. 1, p. 6–43, 2013.

[18] NATIONALSYSTEM FOR GEOSPATIAL INTELLIGENCE : GEOSPATIAL INTELLIGENCE(GEOINT). *Basic doctrine.* Publication 1.0. 2006. 52p.

[19] MOREIRA, A. A golden age for Spaceborne SAR systems. *In*: INTERNATIONAL CONFERENCE MICROWAVE, RADAR, AND RADAR WEEK, 2014 *Proceedings* […] [*S. l.*: *s. n.*], 2014. p. 1–4.

[20] CANTAFIO, L. J. *Space-based radar handbook*. Norwood, MA: Artech House Radar Library, 1989.

[21] TIBERT, G. *Deployable tensegrity structures for space applications*. 2002. 244 p. Thesis (PhD) - Department of Mechanics, Royal Institute of Technology, Stockholm, 2002.

[22] KARE, Jordin T. *Moving receive beam method and apparatus for synthetic aperture radar*. Depositante: The Regents of the University California. US6,175,326 B1. Concessão. 16 Jan 2001

[23] KRIEGER, G. *et al*. Advanced synthetic aperture radar based on digital beamforming and waveform diversity. *In*: *IEEE RADAR CONFERENCE, 2008. Proceedings* […] Piscataway: IEEE, 2008. p. 1–6.

[24] ENTEKHABI, D. *et al*. *SMAP handbook*: soil moistureative passive. Pasadena, California: NASA, 2014. 192 p.

[25] FREEMAN, A. *et al.* SweepSAR: Beam-forming on receive using a reflector-phased array feed combination for spaceborne SAR. *In*: IEEE NATL. RADAR CONFERENCE, 2009, Pasadena. *Proceedings* […] Piscataway: IEEE, 2009.

[26] HUBER S. *et al*. Spaceborne reflector SAR systems with digital beamforming. *IEEE Trans. Aerosp. Electron. Syst.*, v. 48, n. 4, p. 3473–3493, 2012.

[27] “MAPSAR - Phase A: Study Final Report,” São José dos Campos, 2007.

[28] DLR MICROWAVES RADAR INSTITUTE. *TANDEM-L*: a satellite mission for monitoring dynamic processes on the Earth’s surface. German: DLR, 2019. Available: https://www.dlr.de/hr/en/desktopdefault.aspx/tabid-8113/14171_read-35837/. Accessed: 16-Oct-2019.

[29] SPUDIS, P. D. *et al.* Results of the Mini-SAR imaging radar, Chandrayaan-1 Mission to the Moon. *Lunar Planet. Sci. Conf.*, v. 41, p. 1224, March 2010.

[30] THE CEOS Database: mission index. [*S. l.*]: CEOS, ESA, 2015. Available: http://database.eohandbook.com/database/missionindex.aspx. Accessed: 12-Mar-2015.

[31] COSTA, M. M. S.; PASSARO, A. Trends for spaceborne synthetic aperture radar for Earth-observation. *In*: SIMPÓSIO DE APLICAÇÕES OPERACIONAIS EM ÁREAS DE DEFESA, 17., 2015. *Anais* […] São José dos Campos: ITA. DCTA, 2015.

[32] COSTA, M. M. S.; SILVA, A. R. da; PAES, R. L.; PASSARO, A. BR-SAR: a small

spaceborne SAR with an offset reflector antenna and compact polarimetry architectures. *In*: AIAA SPACE AND ASTRONAUTICS FORUM AND EXPOSITION, 2016. *Proceedings* […] Reston: AIAA, 2016.

[33] COLLINS, M. J.; DENBINA, M.; ATTEIA, G. On the reconstruction of Quad-Pol SAR data from compact polarimetry data for ocean target detection. *IEEE Trans. Geosci. Remote Sens.*, v. 51, n. 1, p. 591–600, 2013.

[34] DUBOIS-FERNANDEZ, P. C. *et al*. The compact polarimetry alternative for spaceborne SAR at low frequency. *IEEE Trans. Geosci. Remote Sens.*, v. 46, n. 10, p. 3208–3222, 2008.

[35] FRANCESCHETTII,G.; LANARI,R. *Synthetic aperture radar processing*. Boca Raton, FL: CRC Press, 1999.

[36] WOODHOUSE, I. H. *Introduction to microwave remote sensing*. Boca Raton, FL: Book, CRC Press, 2006.

[37] CLOUDE, S. R. Polarization application in remote sensing. *Physics Today*, v. 63, n. 10, p. 53, 2010.

[38] LEE, J. S.; POTTIER, E *Polarimetric radar imaging:* from basics to applications. Boca Raton, FL: CRC Press, 2009.

[39] RICHARDS, J. A. *Remote sensing with imaging radar*. Canberra, Australia: Springer Science& Business Media, 2009.

[40] CLOUDE, S. *Polarisation:* applications in remote sensing. New York, NY: Oxford University Press., 2009.

[41] ESPESETH,M. M. *Synthetic aperture radar compact polarimetry for sea ice surveillance*. 2015. 202 p. Thesis (PhD in Energy, Climate and Enviroment) - Department of Physics and Technology, The Arctic University of Norway, 2015.

[42] STACY, N.; PREISS, M. Compact polarimetric analysis of X-band SAR data. *In*: EUROPEAN CONFERENCE ON SYNTHETIC APERTURE RADAR, 2006, Dresden. *Proceedings*.[…] Berlin: VDE Verlag, 2006. 4 p.

[43] RANEY, R. K. Hybrid-Polarity SAR overview of hybrid-polarity architecture. *Proceedings of SPIE*, v.45, p.3397-3404, Jan. 2007.

[44] SHIRVANY, R. *Estimation of the degree of polarization in polarimetric SAR Imagery:* principles and applications. 2012. Thesis (Doctorat en Signal, Image, Acostique et Optimisation.) - Institut National Polytechnique de Toulouse,Tolouse 2012.

[45] PAES, R. L. *Detecção de alvos no mar em imagens SAR explorando recursos da polarimetria compacta em modo híbrido.* 2015. 137 f. Tese (Doutorado em Sensoriamento Remoto) - Instituto Nacional de Pesquisas Espaciais, São José dos Campos, 2015.

[46] SILVA. A.de Q. da. *Avaliação de imagens sar no mapeamento de crostas lateríticas do depósito N1 província mineral de Carajás, Par*á. 2010 262 f. Tese (Doutorado em Sensoriamento Remoto) - Instituto Nacional de Pesquisas Espaciais, São José dos Campos, 2010.

[47] VILLAÇA, D. D. C*lassificação de imagens SAR utilizando a resposta polarimétrica.* 2008. Dissertação (Mestrado em Telecomunicações) - Instituto Tecnológico de Aeronáutica, ão José dos Campos,2008.

[48] COLLIN R. E. *Antennas and radiowave propagation*. Singapore: McGraw-Hill, 1985.

[49] ANDRADE, N. S. de O.; SANTA ROSA A. N. de C.; FARIA P. C. de C. As matrizes de covariância e de coerência na Polarimetria SAR. *In*: SIMPÓSIO BRASILEIRO DE SENSORIAMENTO REMOTO, 13., 2007, Florianopolis. *Anais* […] São José dos Campos: INPE, 2007. p. 4759–4766.

[50] CLOUDE, S. R.; POTTIER, E. A Review of target decomposition theorems in radar polarimetry. *IEEE Trans. Geosci. Remote Sens.*, v. 34, n. 2, p. 498–518, 1996.

[51] p. DUBOIS-FERNANDEZ, P. *et al.* Compact polarimetry mode for a low frequency sar in space. *Int. Geosci. Remote Sens. Symp.*, v. 5, n. 1, p. 279–282, 2008.

[52] KLOBUCHAR, J. A. *Ionospheric effects on Earth-space propagation*. Hanscom A. F. B., MA: Ionospheric Physics Division, Air Force Geophysics Lab.1983. 33p. (AFGL-TR-84-0004)

[53] ULABY, Fawwaz Tayssir *et al. Microwave radar and radiometric remote sensing*. An Arbor: University of Michigan Press, 2014.

[54] SAATCHI, S. S.; FREEMAN, Antony. He effects of Faraday rotation on backscatter signatures in SAR image data. *Proc. SPIE,* v. 3120, n. 1, p. 37, 1997.

[55] HARRIS, L. *Correlate function*. [*S. l.*]: L3Harris Geospatial Solutions, 2019. Available: https://www.harrisgeospatial.com/docs/CORRELATE.html. Accessed: 21-Jan-2020.

[56] DAVIES, K. *Ionospheric radio propagation*. Whashington, DC: U.S. Government Printing Office, 1965.

[57] WRIGHT, P. A. *et al.* Faraday rotation effects on L-band spaceborne SAR data. *IEEE Trans. Geosci. Remote Sens.*, v. 41, n. 12 part 1, p. 2735–2744, 2003.

[58] FREEMAN, A.; SAATCHI, S. S. On the detection of Faraday rotation in linearly polarized L-band SAR backscatter signatures. *IEEE Trans. Geosci. Remote Sens.*, v. 42, n. 8, p. 1607–1616, 2004.

[59] CONGRESS OF THE UNITED STATE. Congressional Budget Office. *Alternatives for military space radar*. Washington, DC: CBO, 2007.

[60] BUDDEN, K. G. *The propagation of radio waves*. Cambridge: University of Cambridge Press, 1985.

[61] SOUZA, J. R. *Estudo do conteúdo eletrônico total ionosférico*. 1992. 70 f. Dissertação (Mestrado) - Instituto Nacional de Pesquisas Espaciais, São José dos Campos, 1992. PI(INPE-5417-TDI/481)

[62] GARRIOTT, O. K. SMITH, F. L.; YUEN, P. C. Observations of ionospheric electron Content. *Planet. Sp. Sci.*, v. 13, n. 1, p. 829–838, 1965.

[63] RANEY, R. K. Hybrid-polarity SAR architecture. *IEEE Trans. Geosci. Remote Sens.*, v. 45, n. 11, p. 3397–3404, 2007.

[64] BRUDER, J. A. *IEEE Standard for letter designations for radar-frequency bands*. New York, NY: IEEE, 2003.

APPENDIX A – Symmetry properties in polarimetric remote sensing

a.1 Introduction

This Appendix summarizes the symmetry properties in polarimetric remote sensing presented by Nghiem et al. [5]. This knowledge is fundamental to understand some concepts discussed in this Thesis.

a.2 Reflection Symmetry

Consider the linear polarization basis $\hat{v}$ and $\hat{h}$, where $\hat{v}$ is parallel to plane *P* and $\hat{h}$ is perpendicular to plane *P*. The reflections symmetry conditions hold when the measurements of a linearly polarized wave transmitting V or H and receiving V in the basis rotated by $\alpha+(\pi/2)$ angle to be the same of a linearly polarized wave transmitting V or H and receiving H in the basis rotated by $-\alpha$ angle, as illustrated in Figure A.23.

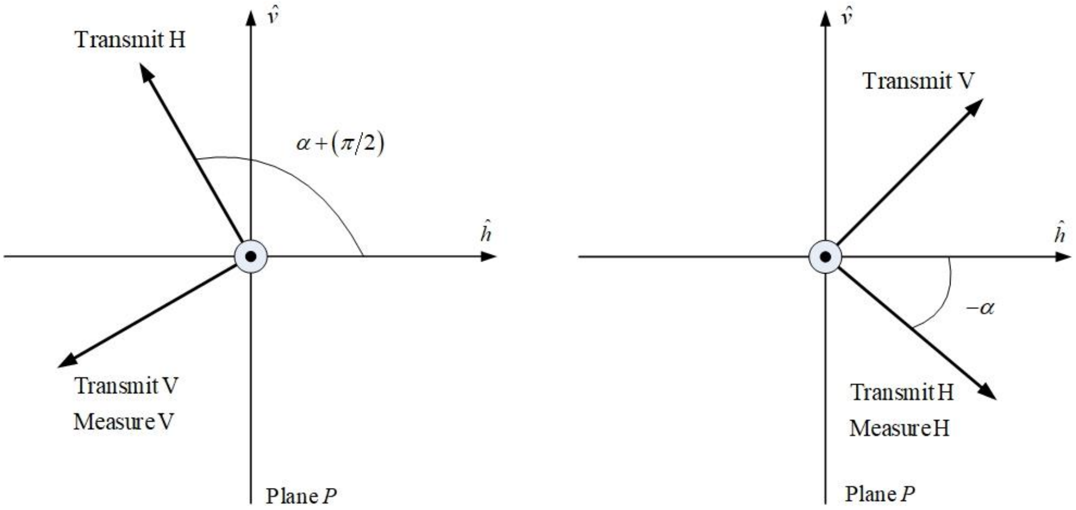

Figure A.23 – The reflection symmetry conditions.
Source: adapted from the original published by Nghiem et al. [5].

a.3 Rotation Symmetry

Consider a linearly polarized wave propaganting parallel to the axis L where the horizontal polarization H and the vertical polarization V are perpendicular to L. The rotation symmetry holds when the covariance matrix remais under wave rotation by an angle α angle, as illustrated in Figure A.24.

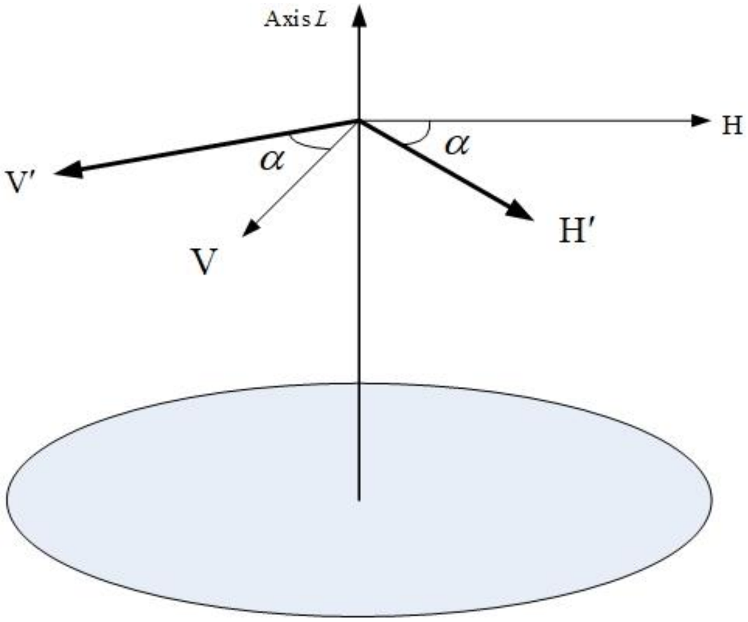

Figure A.24 – The rotation symmetry conditions.
Source: adapted from the original published by Nghiem et al. [5].

a.4 Azimuthal Symmetry

Consider the same conditions presented in Figure A.24. Now, adjoin the Plane P passing through the axis L of the rotation symmetry. This is the condition of azimuthal symmetry, which has both characteristics of the reflection symmetry and the rotation symmetry. Azimuthal symmetry is illustrated in Figure A.25.

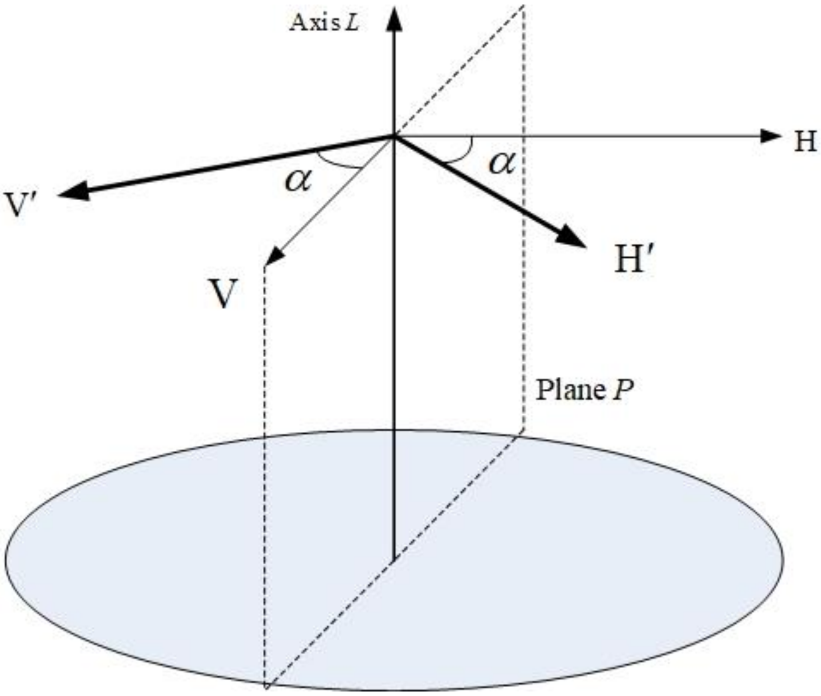

Figure A.25 – The azimuthal symmetry conditions.
Source: adapted from the original published by Nghiem et al. [5].

a.5 Centrical Symmetry

Centrical symmetry conditions hold when axis that has the vector $\hat{t}$ of the linear polarization basis $\hat{v}$ and $\hat{h}$ containing the point *O* and rotated in three dimensions, as illustrated in Figure A.26.

Considering that any plane *P* and any axis *L* passes through the point of centrical symmetry *O*. Hence, the centrical symmetry can be defined as the azimuthal symmetry that the axis L containing the center point O and rotates in three dimensions.

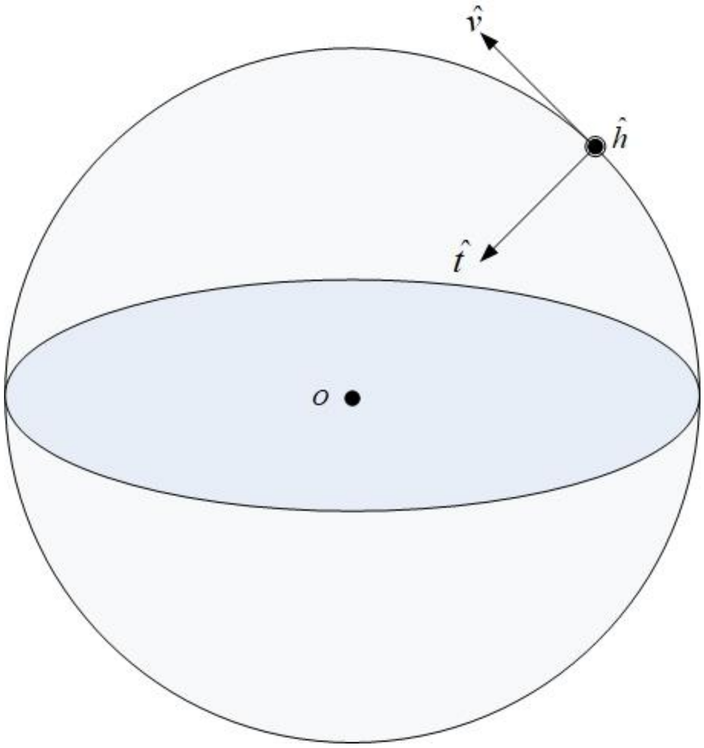

Figure A.26 – The centrical symmetry conditions.
Source: adapted from the original published by Nghiem et al. [5].

APPENDIX B – Effects of the Ionosphere in the Scattering Matrix

b.1 Ionosphere Characteristics

The Ionosphere is a region of the upper atmosphere composed of several regions, ranging from about 50 km to 1000 km (Figure B.27), presenting a large amount of charged particles defining it as an ionized medium. Among existing layers, F is the most relevant for this Thesis, because the peak of electron density occurs within this region at an altitude varying from 250 km to 400 km [56], [57].

The lowest layers, C and D, or low ionosphere, occupy a range from 50 km to 90 km, with the main sources of ionization as the Cosmic Rays for the C region, and the Hard X-rays and Lyman Solar Radiation -α, for the D region. Above these layers, extending from 90 km to about 140 km, is the normal E layer and the Es sporadic, both produced by soft X-rays. From 140 km to the limits with the Plasmasphere is the layer F, subdivided into regions F1 and F2, the first being ionized by extreme ultraviolet sunlight.

Under the influence of a stable magnetic field, such as the Earth's magnetic field, the particles dispersed in these layers are organized into an anisotropic plasma capable of generating various effects on the electromagnetic waves that cross their various regions [58], among which mentioned:

a) Group speed delay;

b) Advancement of the phase carrier;

c) Doppler shift of the carrier;

d) Angular refraction of the trajectory;

e) Distortion of the waveform of transmitted pulses;

f) Phase scintillation and amplitude; and the

g) Faraday rotation of the plane of polarization of linearly polarized waves [52], whose effect is the object of research of this study.

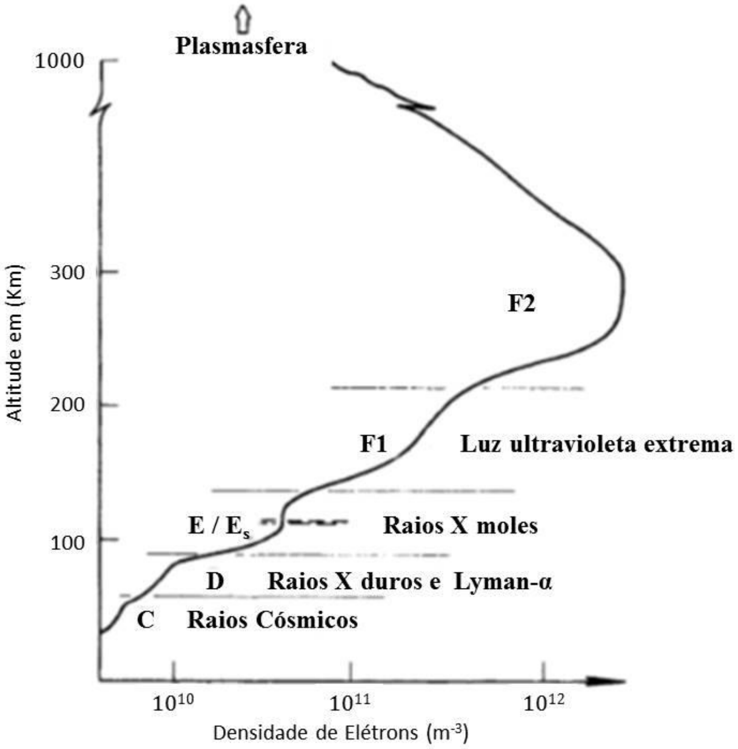

Figure B.27 – Structure of the Ionosphere in mid-latitudes for a summer day and its main ranges of ionizing radiation. Source: adapted from the original published by Davies [56].

b.2 Ionosphere conditions in regions near the Magnetic Equator

Since all space SAR systems operate in orbits ranging from 500 to 1,000 km [4], [59], all radar transmissions cross the ionosphere layers and suffering effects according to the density of the electrons in the pathway (TEC - Total Electron Content).

In the regions near the Magnetic Equator, located approximately 15º of the same, extending around 20º and 25º, there are the so-called *equatorial anomalies*, which deserve greater attention in view of the high TEC values that occur in this region.

Significant changes occur mainly during the day, at the time of the maximum values of solar incidence. Figure B.28 shows an example of TEC map of Brazil with data collected on March 17th, 2015, at 4:20 pm UTC by the Brazilian Space Weather Monitoring and Studies (EMBRACE) team of the National Institute for Space Research (INPE). It can be observed by the warm tones that the high TEC values cover a large part of the Amazonian, coastal and oceanic strip of the country.

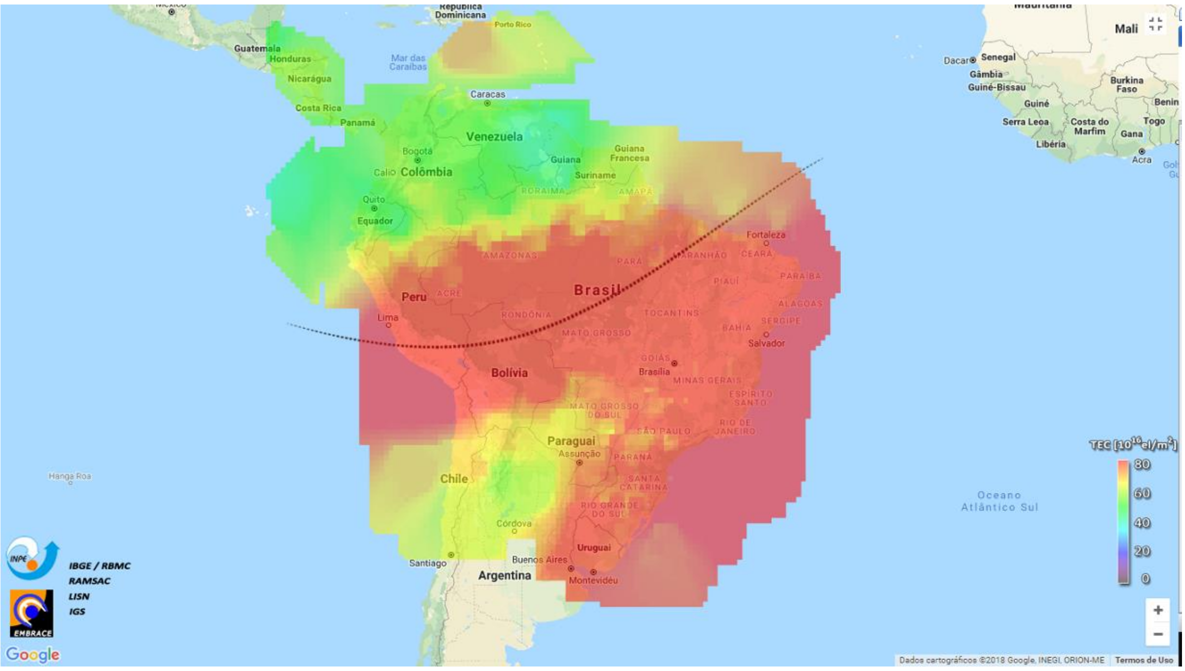

Figure B.28 – TEC map of Brazil at March 17th, 2015, 16h20 UTC (EMBRACE-INPE). Available at < http://www2.inpe.br/climaespacial/portal/tec-map-inicio/ >. Access: May 28th, 2018.

b.3 Faraday Effect and Total Electron Content (TEC)

When a linearly polarized wave passes through the Ionosphere (Figure B.29), it divides into two characteristic waves circularly polarized in the opposite sense. The waves are defined by an ordinary wave and an extraordinary wave. They propagate in parallel with different refractive indexes n_o and n_ε [48], [60].

The ordinary wave in $z = 0$ can be represented by a circularly polarized wave to the right, which in a simplified way

$$\vec{E}^o(0) = E_0^o\left(\vec{e}_h - j\vec{e}_v\right)\exp\{-j\omega t\}. \qquad \text{(B.1)}$$

In turn, the extraordinary wave is given by circular polarization to the left, where

$$\vec{E}^\varepsilon(0) = E_0^\varepsilon\left(\vec{e}_h + j\vec{e}_v\right)\exp\{-j\omega t\}. \qquad \text{(B.2)}$$

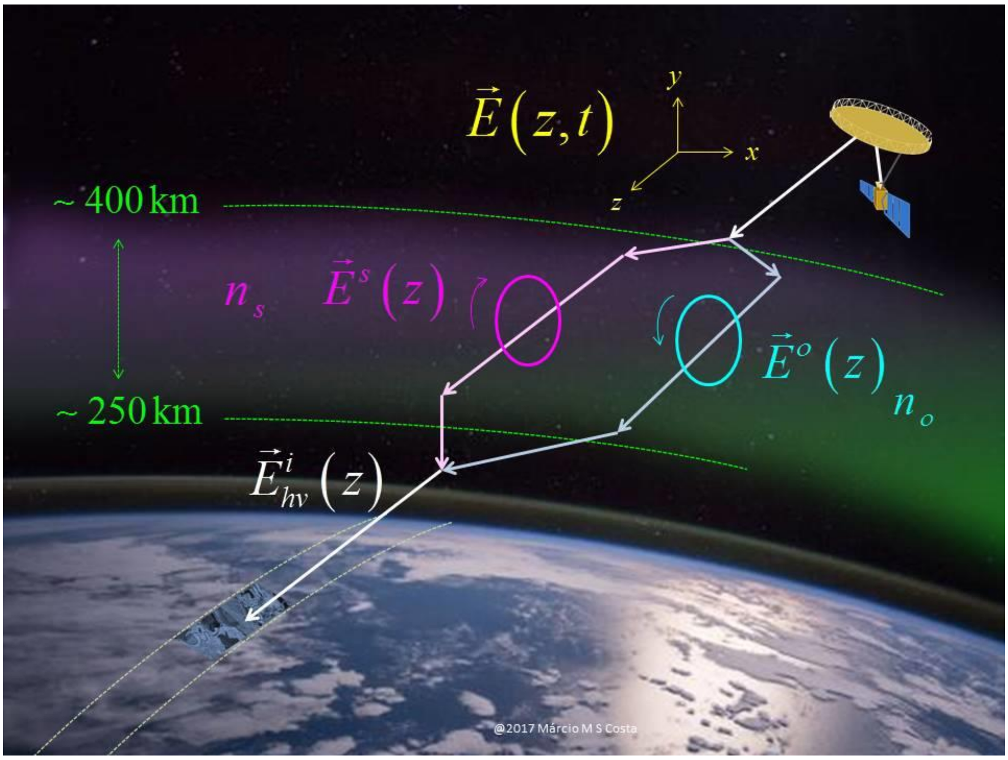

Figure B.29 – Faraday Rotation Effect at the Ionosphere. Source: adapted from the original published by Souza [61].

So that the incident linearly polarized wave is the sum of (B.1) and (B.2), with $E_0^o = E_0^\varepsilon$, which results

$$\begin{aligned}\vec{E}_{hv}^i(0) &= E_0^o\left(\vec{e}_h - j\vec{e}_v\right)\exp\{-j\omega t\} + E_0^\varepsilon\left(\vec{e}_h + j\vec{e}_v\right)\exp\{-j\omega t\}\\ \vec{E}_{hv}^i(0) &= 2E_0^o\exp\{-j\omega t\}\,\vec{e}_h .\end{aligned} \tag{B.3}$$

When traveling a distance z in the Ionosphere, the ordinary and extraordinary waves are represented, respectively, by

$$\vec{E}^o(z) = E_0^o\left(\vec{e}_h - j\vec{e}_v\right)\exp\{-j(\omega t - k_0 z n_o)\}, \tag{B.4}$$

$$\vec{E}^\varepsilon(z) = E_0^o\left(\vec{e}_h + j\vec{e}_v\right)\exp\{-j(\omega t - k_0 z n_\varepsilon)\}, \tag{B.5}$$

where n_o and n_ε are the refractive indices of the medium through which each wave travels.

Thus, the incident wave $\vec{E}_{hv}^i$ is now represented by the sum of (B.4) and (B.5)

$$\begin{aligned}\vec{E}_{hv}^i(z) = E_0^o&\left(\vec{e}_h - j\vec{e}_v\right)\exp\{-j(\omega t - k_0 z n_o)\}\\ &+ E_0^o\left(\vec{e}_h + j\vec{e}_v\right)\exp\{-j(\omega t - k_0 z n_\varepsilon)\}.\end{aligned} \tag{B.6}$$

Which can be rewritten, after mathematical manipulation, as

$$\begin{aligned}\vec{E}_{hv}^i(z) &= 2E_0^o e^{-j\omega t+}\left[\left\{\frac{1}{2}\vec{e}_h\left(e^{jk_0 z n_o} + e^{jk_0 z n_\varepsilon}\right)\right\} - \left\{\frac{1}{2}\,j\vec{e}_v\left(e^{jk_0 z n_o} - e^{jk_0 z n_\varepsilon}\right)\right\}\right]\\ &= 2E_0^o\exp\left\{j\left(\omega t - \frac{1}{2}k_0 z\left(n_o + n_\varepsilon\right)\right)\right\}\\ &\qquad\left[\cos\left\{\frac{1}{2}k_0\vec{z}\left(n_o - n_\varepsilon\right)\right\}\vec{e}_h - \sin\left\{\frac{1}{2}k_0\vec{z}\left(n_o - n_\varepsilon\right)\right\}\vec{e}_v\right],\end{aligned} \tag{B.7}$$

where half the difference between the two transcribed phases in the sine and cosine expressions indicates the angle between the resultant of the incident wave and the plane of polarization, expressed by

$$\Psi = \frac{1}{2} k_0 z \left(n_o - n_\varepsilon \right) . \tag{B.8}$$

This angle Ψ increases as the wave moves in the direction $\vec{z}$, following a variation given by

$$\frac{\partial \Psi}{\partial z} = \frac{1}{2} k_0 \left(n_o - n_\varepsilon \right) . \tag{B.9}$$

The refractive index in an anisotropic medium such as the Ionosphere can be expressed in a simplified form by

$$\mu_{o,\varepsilon} = 1 - \frac{1}{2} X \pm \frac{1}{2} XY \cos \phi_B , \tag{B.10}$$

where

$$\begin{aligned} X &= \frac{f_N^2}{f^2} = \frac{N\mathrm{e}^2}{4\pi^2 \varepsilon_0 m_\mathrm{e} f^2} = \frac{80,61N}{f^2} , \\ Y &= \frac{\mathrm{e}B}{2\pi m_\mathrm{e} f} , \end{aligned} \tag{B.11}$$

where f_N it is called the plasma frequency; ϕ_B is the angle formed between the normal direction of the propagating wave and the current magnetic field; N, e, m_e are the density, charge, and electron mass, respectively; ε_0 is the electrical permittivity in vacuum; and f is the wave frequency [60, p. 39 e 46].

By means of the relations presented in (B.11), it is known that for high frequencies, the values of X and Y are small. According to Budden [60, p. 373], this condition allows establishing the following approximation between expressions (B.9) and (B.11)

$$\frac{1}{2} \left(n_o - n_\varepsilon \right) \approx \frac{1}{2} XY \cos \phi_B . \tag{B.12}$$

Therefore, the variation of Ψ is represented by

$$\frac{\partial\Psi}{\partial z}=\left(\frac{N\mathrm{e}^2}{4\pi^2\varepsilon_0 m_\mathrm{e} f^2}\right)\left(\frac{\mathrm{e}B}{2\pi m_\mathrm{e} f}\right)\cos\phi_B \approx \frac{NB\mathrm{e}^3}{8\pi^2\varepsilon_0 c m_\mathrm{e}^2 f^2}\cos\phi_B\,. \tag{B.13}$$

Integrating in relation to $\vec{z}$ the expression (B.13), we have the expression for the value of the Rotation of Faraday

$$\Psi=\frac{\mathrm{e}^3}{8\pi^2\varepsilon_0 c_0 m_\mathrm{e}^2 f^2}\int_0^z NB\cos\phi_B dz\,, \tag{B.14}$$

that can be rewrite as

$$\Psi=\frac{K}{f^2}\int_0^z NB\cos\phi_B dz\,, \tag{B.15}$$

for a constante $K=2{,}36\cdot 10^4$ in the MKS system.

From the expression (B.15) we define the Total Electron Content – TEC

$$\mathrm{TEC}=\int_0^z Ndz\,, \tag{B.16}$$

and the “Factor of the Magnetic Fiel”, $B\cos\phi_B$, which is usually calculated at an altitude of 400 km [52], [57], [62].

b.4 Effect of Faraday Rotation on the Scattering Matrix

From the polarization ellipse, shown in Figure 2.1, the rotation imposed by the Faraday rotation in the electric field vector is shown in Figure B.30.

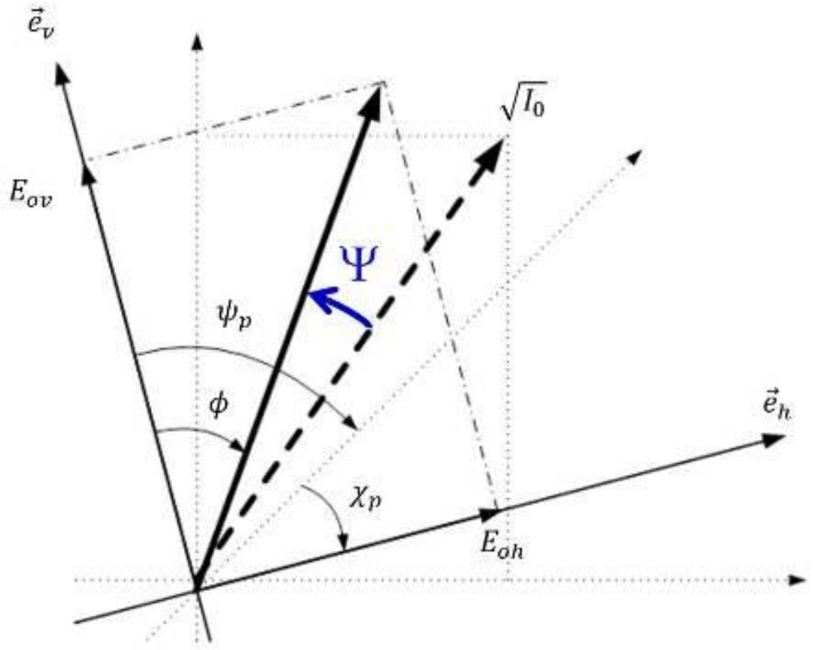

Figure B.30 – Rotation Ψ of the propagation axis.

Without assuming the Principle of Reciprocity presented in Section 2.3, for a Faraday Rotation in the counter-clockwise direction [51] the corresponding rotation of the Scattering Matrix *S*, transforming into the Rotating Matrix *M*

$$M = \begin{bmatrix} M_{HH} & M_{HV} \\ M_{VH} & M_{VV} \end{bmatrix} = \begin{bmatrix} \cos\Psi & \mathrm{sen}\Psi \\ -\mathrm{sen}\Psi & \cos\Psi \end{bmatrix} \begin{bmatrix} S_{HH} & S_{HV} \\ S_{VH} & S_{VV} \end{bmatrix} \begin{bmatrix} \cos\Psi & \mathrm{sen}\Psi \\ -\mathrm{sen}\Psi & \cos\Psi \end{bmatrix}, \text{ or} \tag{B.17}$$

$$M = R_\Psi \, S \, R_\Psi \,, \tag{B.18}$$

where *S* is the Sinclair matrix, or Scattering matrix, described in (2.18), and *M* is the scattering measure matrix, where each element is expressed by

$$\begin{aligned} M_{HH} &= S_{HH}\cos^2\Psi - S_{VV}\mathrm{sen}^2\Psi + \left(S_{HV} - S_{VH}\right)\mathrm{sen}\Psi\cos\Psi, \\ M_{HV} &= S_{HV}\cos^2\Psi + S_{VH}\mathrm{sen}^2\Psi - \left(S_{HH} + S_{VV}\right)\mathrm{sen}\Psi\cos\Psi, \\ M_{VH} &= S_{VH}\cos^2\Psi + S_{HV}\mathrm{sen}^2\Psi + \left(S_{HH} + S_{VV}\right)\mathrm{sen}\Psi\cos\Psi, \text{ and} \\ M_{VV} &= S_{VV}\cos^2\Psi - S_{HH}\mathrm{sen}^2\Psi + \left(S_{HV} - S_{VH}\right)\mathrm{sen}\Psi\cos\Psi. \end{aligned} \tag{B.19}$$

Observe that for $\Psi = 0$, *M* reduces to *S*.

The effect of Faraday rotation can significantly affect transmissions in L and P bands, where it can vary from 40º to 320º in the worst cases, respectively. C and X-bands, the interferences are much smaller, and can lead to values of the order of 2.5º in C-band [39]. The nominal frequency ranges of these bands are shown in appendix F.

One of the ways to mitigate these effects of the ionosphere is through the use of circular polarization in the transmission and the linear polarization in reception, called by Raney [63] as Hybrid mode. This mode is described in Section 2.4.

In the expression (B.20), we present the Jones vector associated with transmission in Hybrid-POL mode, considering the transmission of a circularly polarized wave to the right and the reception system formed by antennas with horizontal and vertical polarization, besides the rotation of Faraday.

$$\vec{J}_s = 1/\sqrt{2}\begin{bmatrix} \cos\Psi & \mathrm{sen}\Psi \\ -\mathrm{sen}\Psi & \cos\Psi \end{bmatrix}\begin{bmatrix} 1 \\ -j \end{bmatrix} = \begin{bmatrix} \exp\{-j\Psi\} \\ -\exp\{j\Psi\} \end{bmatrix} \tag{B.20}$$

where $\vec{J}_s$ is the vector of the wave that illuminates a surface, considering the Faraday rotation, and $1/\sqrt{2}\left[1 \quad -j\right]$ representing the Jones vector for the incident wave with right circular polarization.

In this case, the effects of the Ionosphere on the circular transmission are limited to a phase delay, which may be clockwise or not depending on the direction of the magnetic field *B* in the region of propagation. In the southern hemisphere, it assumes negative values for a coordinate system based on the right-hand rule, where *z* is the axis of propagation toward Earth; *x* equals the polarization H; and *y*, to the polarization V [34], [51], [52].

When the echo signal returns to the SAR system, again the electromagnetic wave crosses the Ionosphere and suffers once again the effect of Faraday's Rotation,

$$\vec{k}_{\Psi} = R_{\Psi} \vec{J}_s = R_{\Psi} \; S \; R_{\Psi} \begin{bmatrix} \exp\{-j\Psi\} \\ -\exp\{j\Psi\} \end{bmatrix} \tag{B.21}$$

Considering that the CP operates only with two degrees of freedom relative to antenna reception, the use of circular polarization has a significant advantage over linear, since it will be less subject to the effects of Faraday rotation.

Therefore, the calibration to be carried out shall take into account

$$\vec{k}_{CP} = \vec{k}_{\Psi} = \exp\left\{-j\Psi\right\}\left[S\right] R_{\Psi} \vec{J}_{Rhc} \text{, and} \tag{B.22}$$

$$C_{CP} = 2\left\langle \vec{k}_{CP} \vec{k}_{CP}^{*} \right\rangle . \tag{B.23}$$

APPENDIX C – Trends for Spaceborne Synthetic Aperture Radar for Earth-Observation

Trends for Spaceborne Synthetic Aperture Radar for Earth-Observation

Márcio Martins da Silva Costa[1] e Angelo Passaro[2]
[1]Technological Institute of Aeronautics, ITA, Praça Mal. Eduardo Gomes, 50, Vila das Acácias, 12228-611, São José dos Campos – SP, Brazil
[2] Institute for Advanced Studies (IEAv), Trevo Cel Aviador José Alberto Albano do Amarante, nº1, Putim, 12228-0011, São José dos Campos – SP, Brazil

***Abstract* — SAR satellites have been increasingly used in the last years. Nowadays, the main challenge is to combine high-resolution with large swath in order to acquire more data with more resolution in a shorter time. Several proposals have been considered in order to achieve this objective. This paper summarizes the trends on Spaceborne SAR systems that promise to overcome the current challenges.**

***Keywords* — Spaceborne SAR, Synthetic Aperture Radar, Remote Sensing.**

I. INTRODUCTION

The ability of monitoring large areas with high resolution images, independent of daylight, vegetal and cloud coverage, smoke, and weather conditions, gives to SAR system advantages over optical sensors. The SAR also has the ability to penetrate in vegetation and soil .

The cost associated to Spaceborn SAR are relatively high, however the coverage and the huge amount of data generated by this sensors are of considerable importance in Defense and for civilian activities, mainly in countries with continental dimensions, such as Brazil, China, and Canada [1]–[6].

In fact, the use of SAR satellites has growing in the last years. Several missions are already operational and there are at least 10 new missions to be launched in the next 5 years [1], [7], [8].

Nowadays, there is a considerable effort to optimize geospatial data collection, boosting the development of new SAR technologies [9].

The information obtained after the processing of SAR data are valuable for several civilian applications, such as the systematic monitoring and analysis of [1], [10], [11]:

a) deforestation, forest biomass change, forest height, vertical forest structure (applications in biosphere);

b) volcanic activities, earthquakes, landslides, plate tectonics (applications in geo/lithosphere);

c) ice cover and mass change, soil moisture, flooding, ocean currents, water level change (applications in hydro/cryosphere), among others.

SAR data have also several applications in Defense providing, for instance [8], [10]–[12]:

a) capacity to access, manipulate, analyze, and manage spatially reference data for mission planning in Geographic Information Systems (GIS);

c) operational environment awareness;

d) monitoring of borders;

c) surveillance of ship traffic;

d) detection and surveillance of targets, among others.

Until 2014, all conventional spaceborne SAR systems have used a planar antenna. In general, a few path of T/R elements are employed to steer the antenna beam towards the swath area [8], [13]. This approach limits the acquisition of SAR images combining high-resolution and wide-swath coverage. The SAR process involves the use of the Doppler shift generated by the relative movement to the ground. If the goal is to have a high-resolution in azimuth, the Doppler bandwidth must be higher on the receiver of the SAR. This implies in to increase the Pulse Repetition Frequency, PRF. However, if the PRF is increased, the echo window length is reduced in order to avoid the interference between consecutive pulses of the reflected signals. This implies in to reduce the swath width. In other words, with conventional technologies it seems that it’s not possible to have high-resolution and wide swath at the same time [1], [14].

In this paper the trends for Spaceborne SAR for Earth-observation is presented. The new technologies explored now attempt to overcome this limitation, allowing to combine high-resolution with large swath.

II. CONVENTIONAL SPACEBORNE SAR DESIGN

The geometry of conventional spaceborne SAR is illustrated in Fig. 1:

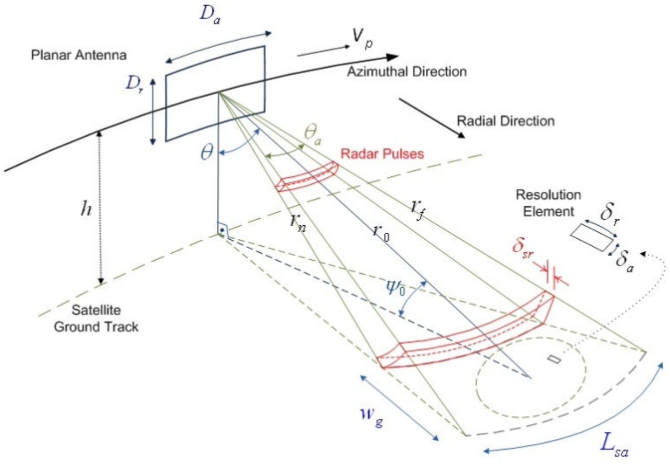

Fig. 1. Geometry of conventional spaceborne SAR.

Costa, Márcio M. S., marcio.costa.br@ieee.org; Passaro, A., angelopassaro@gmail.com.

where h is the altitude of the satellite; D_r is the width of the antenna; D_a is the azimuthal direction antenna length; v_p is the velocity of the platform; θ is the look angle; θ_a is the aperture azimuth beamwidth; r_n is the near range; r_0 is the range from the SAR sensor to the target; r_f is the far range; ψ_0 is the grazing angle; w_g is the swatch; δ_{sr} is the slant-range resolution; δ_r is the ground-plane spatial resolution; δ_a is the ground-plane azimuthal direction resolution; and L_{sa} is the synthetic aperture length [14].

The ground-plane azimuthal direction resolution is given by:

$$\delta_a = D_a/2 \tag{1}$$

The relation between D_a and PRF can be expressed by:

$$D_a = 2v_p/PRF\ , \tag{2}$$

i.e.:

$$\delta_a = v_p/PRF\ . \tag{3}$$

The slant-range resolution can be expressed by:

$$\delta_{sr} = c_0/2\beta \tag{4}$$

where c_0 is light speed and β is the transmitted pulse bandwidth.

The ground-plane spatial resolution is obtained by projecting δ_{sr} to the ground plane:

$$\delta_r = c_0/2\beta \cdot \cos\psi_0\ . \tag{5}$$

The several pulses transmitted from space by SAR satellite reach the target in different distances. In order to avoid ambiguity, i.e., the interference between consecutive pulses, a minimum time interval between each pulse is needed. This time interval increases as w_g increases and, consequently, it decreases *PRF*. The relation between w_g and *PRF* is given by:

$$w_g \approx c_0/\left(2 \cdot PRF \cdot \cos\psi_0\right). \tag{6}$$

Equations (3), (5) and (6) suggest that high resolution and large swath are conflicting requirements. As a consequence, it would not be possible to design a SAR satellite system providing at the same time high resolution and large swath [1], [3], [14]–[16].

However, several new techniques have been developed recently with the purpose to overcome this restriction.

III. HIGH RESOLUTION WIDE-SWATH (HRWS)

One of the new trends is to employ a planar antenna with digital beamforming (DBF) on receiver in elevation associated with multiple receive channels in azimuth (Fig.2).

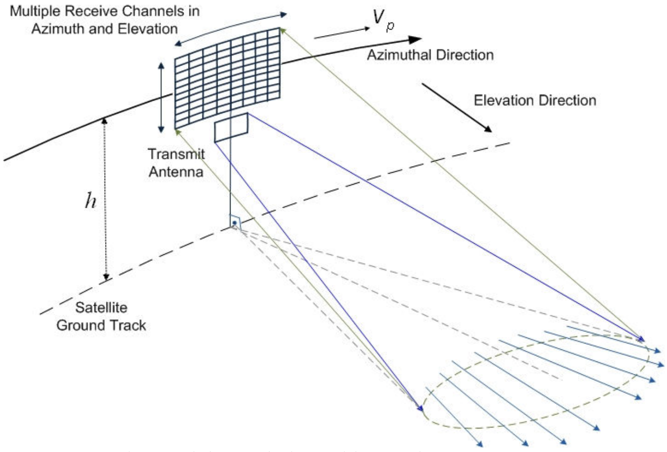

Fig. 2. High Resolution Wide-Swath SAR system.

The signal is transmitted by a single small antenna that doesn't use DBF. This antenna is designed to illuminate a wide swath with broad bandwidth. The echoes from the scene are received by DBF elements arranged in azimuth and elevation uniform path. The multiple sub-apertures are connected to a specific channel that amplifies, digitizes and records the signal for subsequent sending to the ground station. This technique is known by Scan-on-Receive (SCORE) and it has a good performance on planar scenes. However, mountainous terrains with large gaps reduce the high resolution performance [1], [13], [17]–[19].

The difference between this technique and the traditional stripmap mode lies in the coherent combination of the echo signals at the receiver.

In order to enlarge the swath, HRWS must have a long antenna. This requirement can be a limitation considering the launcher fairings [1], [19], [20].

IV. ULTRA-WIDE SWATH OPERATIONAL MODES

a) ScanSAR with Multiple Azimuth Channels

This technique employs the Burst Mode Operation. This mode allows switching the footprint presented in section III into different sub-swaths (Fig. 3). However, this technique reduces the illumination time per sub-swath. The alternative is to design a Multi-Channel in Burst Mode enabled to increase the time spent in one footprint [1], [19], [21].

According to [1] and [22] this SAR system might be used by ESA (European Space Agency) in the Sentinel-1 replacement. Nevertheless, this concept needs additional research in order to solve challenges like bandwidth variation, large variation on squint angles and different burst *PRF*[19].

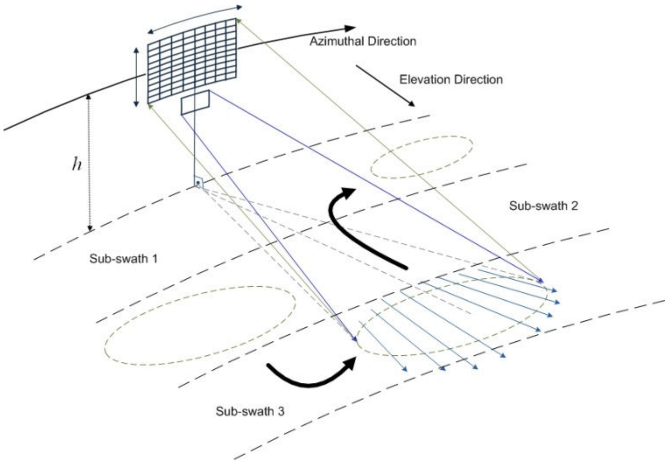

Fig. 3. ScanSAR with Multiple Azimuth Channels.

b) Single-channel SAR with Multiple Elevation Beams

This is an alternative to ScanSAR with Multiple Azimuth Channels operational mode. This approach considers a different path of elements disposed in elevation. The arrangement of elements in elevation faces different swaths that return the echo signal generated by a single transmitting antenna.

The challenge is to cover the blind ranges let between the illuminated swaths. The possible solution can be the use of a constellation where each satellite has different bursts with different *PRF* (Fig. 4) [1], [19].

The other challenge of this mode is the use of a higher SAR antenna, as discussed in Section III.

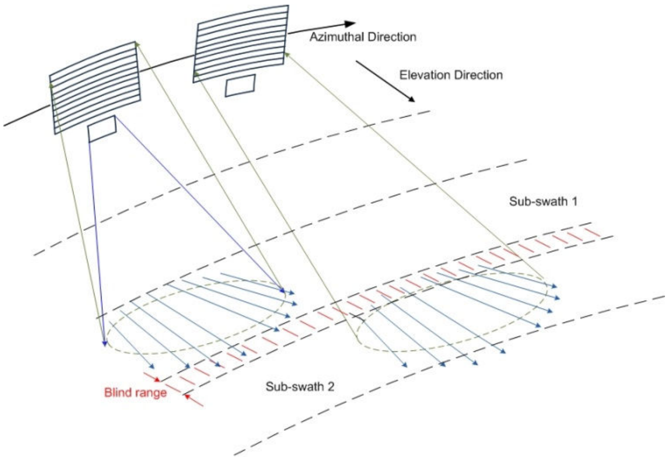

Fig. 4. Single-channel SAR with Multiple Elevation Beams.

c) Digital Beamforming with Reflector Antenna

A promising alternative to overcome the challenge of the higher planar antenna is to employ a deployable reflector antenna (Fig. 5).

The heritage of the successful employment of these antennas in telecommunication satellites enhances the trend to implement this technology in modern SAR systems.

These antennas are made with advanced light graphite-epoxy composite which has low sensitivity to space thermal variations.

The gain of the antenna allows to improve the signal-to-noise rate, using a lower transmission power. This feature reduces considerably the power requirement, usually between 3,000W and 5,000W for traditional planar systems, to levels about 1,000 W [1], [14], [19], [23]–[27].

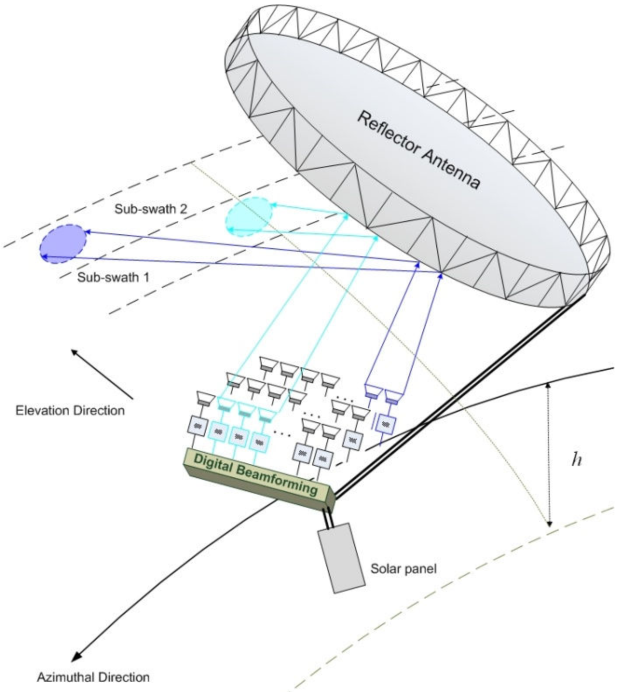

Fig. 5. Digital Beamforming with Reflector Antenna.

The antenna focuses the scene reflecting the signal transmitted by a set of feed T/R elements. This set depends on the swath that will be illuminate. The signal echoes back to the antenna and are registered through the feeds switched as receivers. Along azimuthal direction the beams are swept in order to cover the entire scene [23], [24].

This concept was introduced by NASA/JPL (Jet Propulsion Laboratory) and DLR during Tandem-L/DESDynI projects researches [1].

d) Rotating Reflector Antenna

This concept was introduce by NASA/JPL in the mission named Soil Moisture Active and Passive (SMAP).

This approach does not use a DBF technology. A single feed is pointed to the antenna that has a rotation rate about 13.0 to 14.6 rpm. The footprint has a swath about 40 km. However, the rotation along track, associated to processing algorithms, allows covering a 1.000 km of swath (Fig. 6).

The satellite was launched January, 29th 2015 and the intensive period of calibration and validation is expected to be finished at April, 27th 2016[26], [28], [29].

One of the advantages of this project is to cover a large area in a few days. The entire planet can be mapped at least four times faster than with the use of the present technology [28].

One of the difficulties to implement this technology is the spin of the antenna. The attitude of the satellite must be controlled when the rotation starts, in order to prevent displacement of the provided orbit [20].

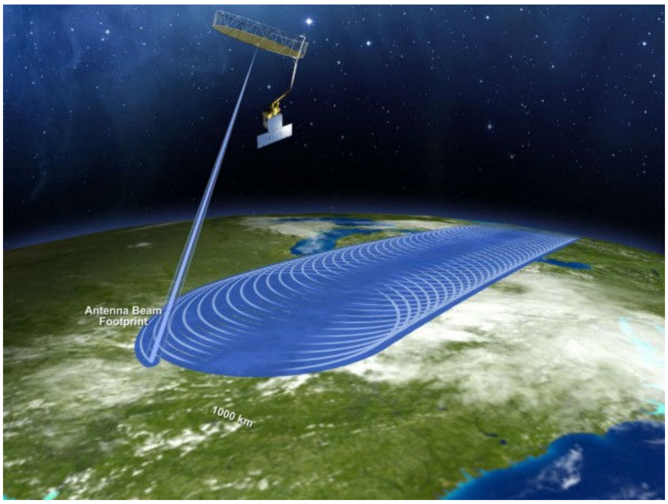

Fig. 6. SMAP Mission Illustrative concept. Available at <http://news.sciencemag.org/> and [26]. Access:July 10th.

V. FINAL CONSIDERATIONS

The future of the Spaceborne SAR systems is promising. Several missions are already launched and there are at least 10 new missions to be launched in the next 5 years[1], [7], [8].

The use of reflector antennas has a potential to cover large areas in short time. The first mission using this technology was already launched and there are new projects upcoming in the next years [26], [30].

DBF arises as a good solution to allow for SAR missions with high-resolution and large swath simultaneously. A very interesting alternative to DBF is the usage of rotating antennas with just one feed.

Ongoing researches in other areas, not mentioned in this work, the experience and results of SMAP mission, and the development of projects that use DBF will drive the trends of Spaceborne SAR Systems.

REFERENCES

[1] A. Moreira, P. Prats-iraola, M. Younis, G. Krieger, I. Hajnsek, and K. P. Papathanassiou, “A Tutorial on Synthetic Aperture Radar,” *Geoscience and Remote Sensing Magazine, IEEE*, no. 1, pp. 6 – 43, 2013.

[2] M. S. M. Costa and D. Fernandes, “Análise do Emprego de uma Constelação de Pequenos Satélites SAR em Vigilância Marítima .,” in *XVI Simpósio de Aplicações Operacionais em Áreas de Defesa - XVI SIGE*, 2014, pp. 90–95.

[3] G. Franceschetti and R. Lanari, *Synthetic Aperture Radar Processing*. Boca Raton, FL: CRC Press, 1999.

[4] I. H. Woodhouse, *Introduction to Microwave Remote Sensing*. Boca Raton, FL: Book, CRC Press, 2006.

[5] R. Schröder, J. Puls, I. Hajnsek, F. Jochim, T. Neff, J. Kono, W. R. Paradella, M. M. Q. Da Silva, D. M. De Valeriano, and M. P. F. Costa, “MAPSAR: A small L-band SAR mission for land observation,” *Acta Astronaut.*, vol. 56, no. 1–2, pp. 35–43, 2005.

[6] D. Entekhabi, E. G. Njoku, P. E. O’Neill, K. H. Kellogg, W. T. Crow, W. N. Edelstein, J. K. Entin, S. D. Goodman, T. J. Jackson, J. Johnson, J. Kimball, J. R. Piepmeier, R. D. Koster, N. Martin, K. C. McDonald, M. Moghaddam, S. Moran, R. Reichle, J. C. Shi, M. W. Spencer, S. W. Thurman, L. Tsang, and J. Van Zyl, “The soil moisture active passive (SMAP) mission,” *Proc. IEEE*, vol. 98, no. 5, pp. 704–716, 2010.

[7] “Satellite Missions Directory - Earth Observation Missions - eoPortal,” 2015. [Online]. Available: https://directory.eoportal.org/web/eoportal/satellite-missions. [Accessed: 13-Mar-2015].

[8] A. Moreira, “A Golden Age for Spaceborne SAR Systems,” in *Microwaves, Radar, and Wireless Communication (MIKON), 2014 20th International Conference on*, 2014, pp. 1–4.

[9] M. Younis, A. Patyuchenko, S. Huber, and G. Krieger, “High Performance Reflector-Based Synthetic Aperture Radar -A System Performance Analysis -,” in *Radar Symposium (IRS), 2010 11th International*, 2010, pp. 1–4.

[10] James B. Campbell, *Introduction to Remote Sensing*, 4th ed. New York, NY: The Guilford Press, 2007.

[11] U. S. N. G.-I. Agency, “Geospatial Intelligence (GEOINT) Basic Doctrine,” p. 51, 2006.

[12] J. Publication, “Geospatial Intelligence in Joint Operations,” no. October, 2012.

[13] M. Younis, S. Huber, A. Patyuchenko, F. Bordoni, and G. Krieger, “Performance Comparison of Reflector- and Planar-Antenna Based Digital Beam-Forming SAR,” *Int. J. Antennas Propag.*, vol. 2009, pp. 1–13, 2009.

[14] L. J. Cantafio, *Space-based Radar Handbook*. Norwood, MA 02062: Artech House Radar Library, 1989.

[15] John C. Curlander and Robert N. McDonough, *Synthetic aperture radar — systems and signal processing*, vol. 29, no. 1. Hoboken, NJ: John Wiley & Sons, Inc, 1992.

[16] N. Gebert, “Digital Beamforming on Receive : Techniques and Optimization Strategies for SAR Imaging,” vol. 45, no. 2, 2009.

[17] F. Bordoni, M. Younis, E. M. Varona, N. Gebert, and G. Krieger, “Performance Investigation on SCAN-ON-RECEIVE and Adaptive Digital Beam-Forming for High-Resolution Wide-Swath Synthetic Aperture Radar,” in *International ITG Workshop on Smart Antennas*, 2009, pp. 114–121.

[18] C. Fischer, E. A. Friedrichshafen, and C. Heer, “Development of a High-Resolution Wide-Swath SAR Demonstrator,” in *Synthetic Aperture Radar (EUSAR), 2010 8th European Conference on*, 2010, pp. 1166–1169.

[19] G. Krieger, M. Younis, N. Gebert, S. Huber, F. Bordoni, A. Patyuchenko, and A. Moreira, “Advanced Concepts for High-Resolution Wide-Swath SAR Imaging Multi-Channel ScanSAR Mode,” pp. 524–527, 2010.

[20] W. J. Larson and J. R. Wertz, *Space Mission Analysis and Design*, 3th ed. Dordrecht: Microcosm Press, 2005.

[21] N. Gebert, G. Krieger, and A. Moreira, “Multi-Channel ScanSAR for High-Resolution Ultra-Wide-Swath Imaging,” pp. 3–6.

[22] C. Schaefer, C. Heer, and M. Ludwig, “Advanced C-Band Instrument Based on Digital Beamforming,” pp. 1–4.

[23] T. Freeman, P. Rosen, B. Johnson, R. Jordan, and Y. Shen, “DESDynI A NASA Mission for Ecosystems , Solid Earth and Cryosphere Science,” 2008.

[24] a. Freeman, G. Krieger, P. Rosen, M. Younis, W. T. K. Johnson, S. Huber, R. Jordan, and a. Moreira, “SweepSAR: Beam-forming on receive using a reflector-phased array feed combination for spaceborne SAR,” *IEEE Natl. Radar Conf. - Proc.*, no. 818, 2009.

[25] W. a. Imbriale, S. S. Gao, and L. Boccia, *Space Antenna Handbook*. John Wiley & Sons, Inc., 2012.

[26] “SMAP Handbook.”

[27] Z. Liangbo, L. Jie, Z. Changjiang, and W. Zhenxing, “Considerations of spaceborne SAR system design,” in *Radar Conference 2013, IET International*, 2013, vol. 251, pp. 1 – 6.

[28] M. D. Stegman, “SMAP antenna feed radome: Design, development, and test,” in *IEEE Aerospace Conference Proceedings*, 2011, pp. 1 – 14.

[29] “SMAP: Timeline.” [Online]. Available: http://smap.jpl.nasa.gov/mission/timeline/. [Accessed: 10-Jul-2015].

[30] A. Moreira, I. Hajnsek, G. Krieger, K. Papathanassiou, and M. Eineder, “Tandem-L: Monitoring the Earth’s Dynamics with InSAR

and Pol-InSAR," in *Proc. of "4th Int. Workshop on SCience and Applications of SAR Polarimetry and Polarimetric Interferometry - PolInSAR 2009,"* 2009, no. April, pp. 26–30.

APPENDIX D – BR-SAR: a small spaceborne SAR with an offset reflector antenna and compact polarimetry architectures

AIAA 2016-5499

SPACE Conferences and Exposition
13 - 16 September 2016, Long Beach, California
AIAA SPACE 2016

BR-SAR: a small spaceborne SAR with an offset reflector antenna and compact polarimetry architectures

Márcio Martins da Silva Costa[1]
Technological Institute of Aeronautics, ITA, Praça Marechal Eduardo Gomes, 50, Vila das Acácias, 12228-611, São José dos Campos – SP, Brazil

Adenilson Roberto da Silva[2]
National Institute for Space Research (INPE), Avenida dos Astronautas, nº1758, Jardim da Granja, 12227-010, São José dos Campos – SP, Brazil

Rafael Lemos Paes[3] and Angelo Passaro[4]
Institute for Advanced Studies (IEAv), Trevo Cel Av José Alberto Albano do Amarante, nº1, Putim, 12228-0011, São José dos Campos – SP, Brazil

This paper introduces a new small L-Band Synthetic Aperture Radar conceptual mission, named BR-SAR. We associate a Mesh Deployable Offset Reflector Antenna and Compact Polarimetry technique in order to enlarge the swath in high resolution mode. The gain of the Offset Reflector Antenna allows to improve the signal-to-noise rate, using a lower transmissions power, and Compact Polarimetry allows to reduce the mass, cost and complexity of the system. The new configuration uses the same spacecraft bus of MAPSAR mission, the Brazilian Multi-Mission Platform (MMP). Additionally, aspects of the antenna design, of the array processing, and of the spacecraft bus are presented.

Nomenclature

P_{Dr} = total power delivered to the radar signal processor
P_t = peak transmitted power
G = antenna gain
λ = wavelength
σ = target-specific parameter called Radar Cross Section (*RCS*)
R = distance from the satellite to the imaged area
A_e = antenna effective aperture
ϕ = angle that the antenna pointing to the center of the paraboloid
f_s = sampling frequency
D = reflector diameter
D' = reflector offset
m = reflector clearance aperture efficiency
ϕ = angle that the antenna points to the center of the paraboloid
$s(t)$ = radar signal transmitted at time t
$ch1$ = feeder 1 of the offset antenna
$ch2$ = feeder 2 of the offset antenna
n = number of the channel, for n=1,2

---

[1] Doctoral Student in Science and Space Technologies, AIAA/IEEE Student Member, marcio.costa.br@ieee.org
[2] Program Manager of the Multi-mission Platform-Based Satellite Program, adenilson.silva@inpe.br
[3] Researcher, IEAv Geointelligence Division, IEEE Member, rafael.paes.it@ieee.org
[4] Posgradute Coordinator in Sciences and Space Tecnhonolgy, IEEE Member, IEAv Physical Applied Division, angelopassaro@gmail.com

$s(t,n)$ = radar signal transmitted at time t and channel n
$\mathrm{Re}[\cdot]$ = real part of one number or complex function
$\tilde{s}(t,n)$ = complex envelope of the radar signal transmitted at time t and channel n
$\exp\{\}$ = exponencial function
j = imaginary unit
ω_c = carrier frequency in radian
$r(t)$ = radar echo signal at time t
θ = angle of arrival of the echo signals at the channels
$r(t,n)$ = radar echo signal at time t and channel n
$a(\theta)$ = vector that incorporates all off the spatial characteristics of the channel array for θ angle
$\tilde{c}(t,n)$ = complex reflectivity of the target at time t and channel n
τ_n = signal delay for each channels
$u(t,n)$ = vector of additive noise at time t and channel n
$[\cdot]^T$ = transpose matrix
$y(t)$ = preliminary array output
$h_n(\tau)$ = impulse response of the channel array
$Y(\omega)$ = preliminary array outup at frequency domain
$H(\omega)$ = impulse response of the array at frequency domain
$R(\omega)$ = radar echo signal at frequency domain
$y_a(t)$ = array output
w_n = complex weight vector at channel n
u_c = noise covariance matrix
$\mathrm{E}\{\cdot\}$ = the expected value
G_a = the gain of the array
$\vec{E}$ = Jones vector
$E_{x,y}$ = amplitude of the x and y components of electrical field
$\delta_{x,y}$ = phase of the x and y components of electrical field
$\vec{E}_{Rhc}$ = unit right-circular transmit polarization Jones vector
c = speed of light
r_0 = the range from the SAR sensor to the target
S = Sinclair matrix
$S_{i,j}$ = complex backscatter coefficient with i transmit and j receive polarization
k_{Rhc} = scattering vector
C_{Rhc} = covariance matrix
$\langle\cdot\rangle$ = spatial or temporal averaging
$\left({}^{*T}\right)$ = complex conjugate transpose
$\Im$ = imaginary part
$\vec{k}_p$ = Pauli scattering vector

I. Introduction

Over the years Synthetic Aperture Radar (SAR) satellites has been extensively used in remote sensing activities. As an active system, SAR presents several advantages over optical sensors, such as, independence of daylight and weather conditions.

Spaceborne SAR systems follow different planning mission criteria from those observed by optical sensors launched into space. [1] In order to plan a SAR mission, the first step is the analysis of the radar equation

$$P_{Dr} = P_t G^2 \lambda^2 \sigma / (4\pi)^3 R^4, \text{ for } G = 4\pi A_e / \lambda^2 \tag{1}$$

where P_{Dr} denote the total power delivered to the radar signal processor; G is the antenna gain; P_t is the peak transmitted power; λ is the wavelength; σ is the target-specific parameter called Radar Cross Section (*RCS*); R is the distance from the satellite to the imaged area; and A_e the antenna effective aperture.

Expression (1) suggests that in order to double R, A_e must increase four times. Higher altitudes can provide a larger coverage area on the Earth, but at the expensive of more power demanding and a larger antenna, which means a higher cost. For several years, this relation was an engineering challenge, primarily because planar antennas were the main technology employed in the missions focused on the Earth observation.

Missions in deep space were the first ones to implement Reflector Antennas in SAR satellites. In 1983, the ancient URSS launched the Venera 15/16 missions to explore Venus.[2,3] Six years latter the Magellan mission from NASA/JPL followed the Venera spacecrafts. In the following, Cassini mission was launched in 1997 to explore Saturn. [2–5] All these missions used an architecture based on the Reflector Antennas concept. The design foresaw the parabolic dish attached adjoining to the spacecraft.

Years later, the parabolic dish was redesigned using deployable resources as supporting booms and mechanics systems for an offset architecture. [1–5] This approach was introduced at first by Kare,[6] in 1998, and reinvented by NASA/JPL and DLR during joint studies for Tandem-L and DESDynI (Deformation, Ecosystem Structure and Dynamics of Ice) missions. [7,8] In January 31th, 2015, NASA/JPL launched the Soil Moisture Active Passive (SMAP) satellite mission into a Sun-synchronous orbit (*SSO*) with a 685 km altitude, incorporating this new concept for Earth observation.[3,9]

The offset architecture has several advantages over the planar antennas. The gain of the Reflector Antennas allows improving the signal-to-noise rate, using a lower transmission power. If Digital Beamforming (*DBF*) array is implemented in association, the transmission of the path of feed elements generates a broad transmitting beam able to illuminate a wide swath on the Earth. The echoes received from a given direction activate only one or a small number of elements, which means that a low number of signals will be processed. In other words it reduces the necessity of on board processing, if compared with traditional planar antennas. This implies yet in a hardware reduction, reduction of energy and increase of lifetime of satellite. [1,10] This feature reduces considerably the power requirement, usually between 3,000W and 5,000W for traditional planar systems, to levels about 1,000 W.[3,5,7,10–14]

Considering the conditions about length of A_e mentioned in equation (1), deployable structures are the only way to built a large and lightweight antennas able to be applied in a satellite. Another advantage lies in the fact that these structures can better withstand the efforts inside the launcher fairing. So, the deployable antenna is only subject to the orbital loads, which are considerably lower than loads during the launch. The disadvantage of deployable offset reflector antennas is the risky of the reconstruction in space. However, e.g., SMAP mission shows that the open of the structure can be performed successfully in space. [2]

The future of the employment of mesh deployable offset reflector antenna is promising. The next mission to implement the same antenna concept will be NISAR (NISAR-ISRO Synthetic Aperture Radar). NISAR is a joint mission between United States and Indian with the purpose to launch a satellite with L-band and S-band SAR systems into a 747 km polar orbit. Another mission to implement the same antenna concept is the Tandem-L, conducted by DLR. The relevant differences between SMAP and Tandem-L are the feed and the antenna architecture. Whereas SMAP uses just one feed horn and a rotating antenna, Tandem-L incorporate the benefits of the innovative *DBF* technique associated with a fixed offset reflector antenna in order to have a wide swath about 350 km. The mission is planned to be launched in 2023. [15–23]

In addition to these examples, there are other SAR missions planned which proposes the use of small platforms, e.g., RADARSAT Constellation. In this case, the use of Micro-Electro-Mechanical Systems (*MEMS*), the Micro-Opto-Eletro-Mechanical Systems (*MOEMS*) and microphotonic devices as the core of microwave-photonic outfit for telecommunications satellite payload have been a remarkable solution to reduce the mass and the power necessity of the platform.[24]

Compact Polarimetry, CP, is a technique that also contributes to reduce cost, mass, and complexity of SAR satellites, presenting several advantages over traditional polarimetric modes as the increase of the gain and swath. [25–29] CP is a general term used to describe a number of techniques based on coherent dual-polarized SAR. The basic idea is to transmit a circularly polarized wave, or a linear wave oriented at 45 degrees, in order to gain increased polarimetric information over horizontal/vertical dual-pol transmissions, without the swath width reduction of full polarimetry (full-pol).[25,30–34]

Finally, it was not found in the extensive literature reviewed space missions which employ a Mesh Deployable Offset Reflector Antenna Design on board of a small satellite with CP techniques associated. Hence, the contribution of this work lies in the analysis of this conceptual and innovative proposal of space system based on small satellites. For this purpose, the Brazilian Multi-Mission Platform (MMP) has been used.

II. BR-SAR Satellite

In order to analyze the employment of a Reflector Antenna and CP in a small satellite, the Brazilian Multi-Mission Platform (MMP) is used as a baseline for the spacecraft bus (Fig. 1).

The Multimission Platform have being developed by INPE (National Institute for Space Research), using a modular concept (Fig. 2). The MMP has been used as spacecraft bus for a SAR payload. The preliminary studies for the Phase A MAPSAR mission, were conducted by DLR and INPE, in 2007.[35,36]

With the mass about 250 Kg, the platform can provide resources for a payload up to 280 Kg. Then, considering the mass reduction by using the compact polarimetry and the length designed for the Reflector Antenna, it is expected that MMP bus can withstand the mass and estimated required resources for the SAR payload. It is also important to note that the MMP bus performance figures provided are nominal ones. Special needs and/or additional requiments can be analyzed case by case.

Furthermore, the MMP provides capacity for support missions in low earth orbit where all the current SAR satellite systems have been placed. [37] Moreover, the power budget supplies the output peak power of 304W and it can provide enough power for a SAR system based on a Reflector Antenna.

The MMP modular concept and design allows to fullfil different missions requirements concerning orbit, pointing orientation and payload accommodation and monitoring. The first mission to use the MMP bus will be the Amazonia 1 mission. The Amazonia 1 mission will be a remote sensing mission using an optical payload. The Amazonia 1 satellite is planned to be launched in 2018.

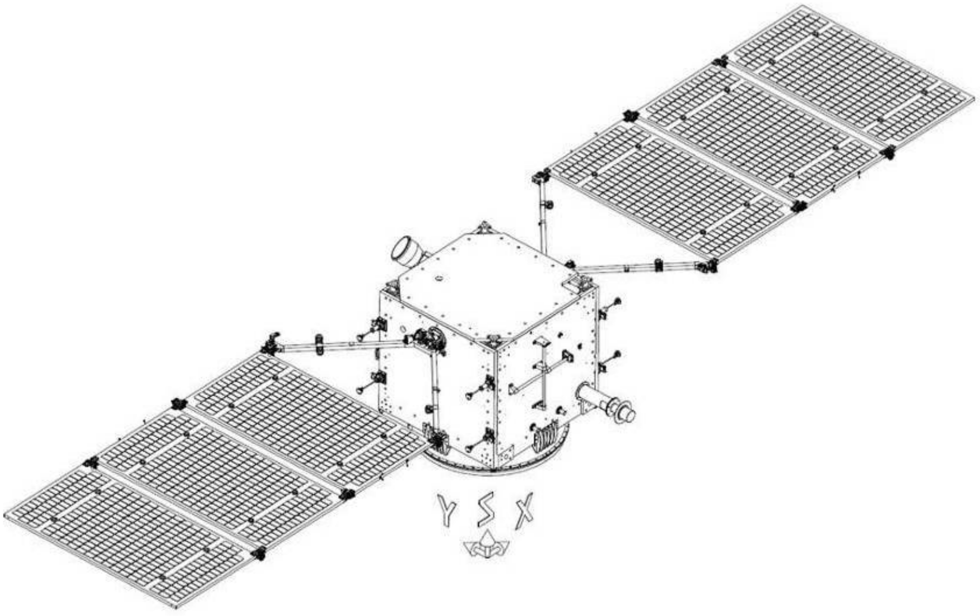

Figure 1. Brazilian Multi-Mission Platform (MMP) in orbit configuration (Courtesy of National Institute for Space Research, INPE)

The basic specifications are summarized by Table 1.

Table 1 Brazilian Multi-Mission Platform (MMP) Parameters

Parameters	Value
Dry Mass	*300 kg*
Total Mass	*345 kg*
Power (average)	*225 W*
Power (total)	*304 W*
Peak power (10 minutes)	*900 W*
MMP/Payload Mechanical Interface	*951.6x951.6 mm(xy-axis)*

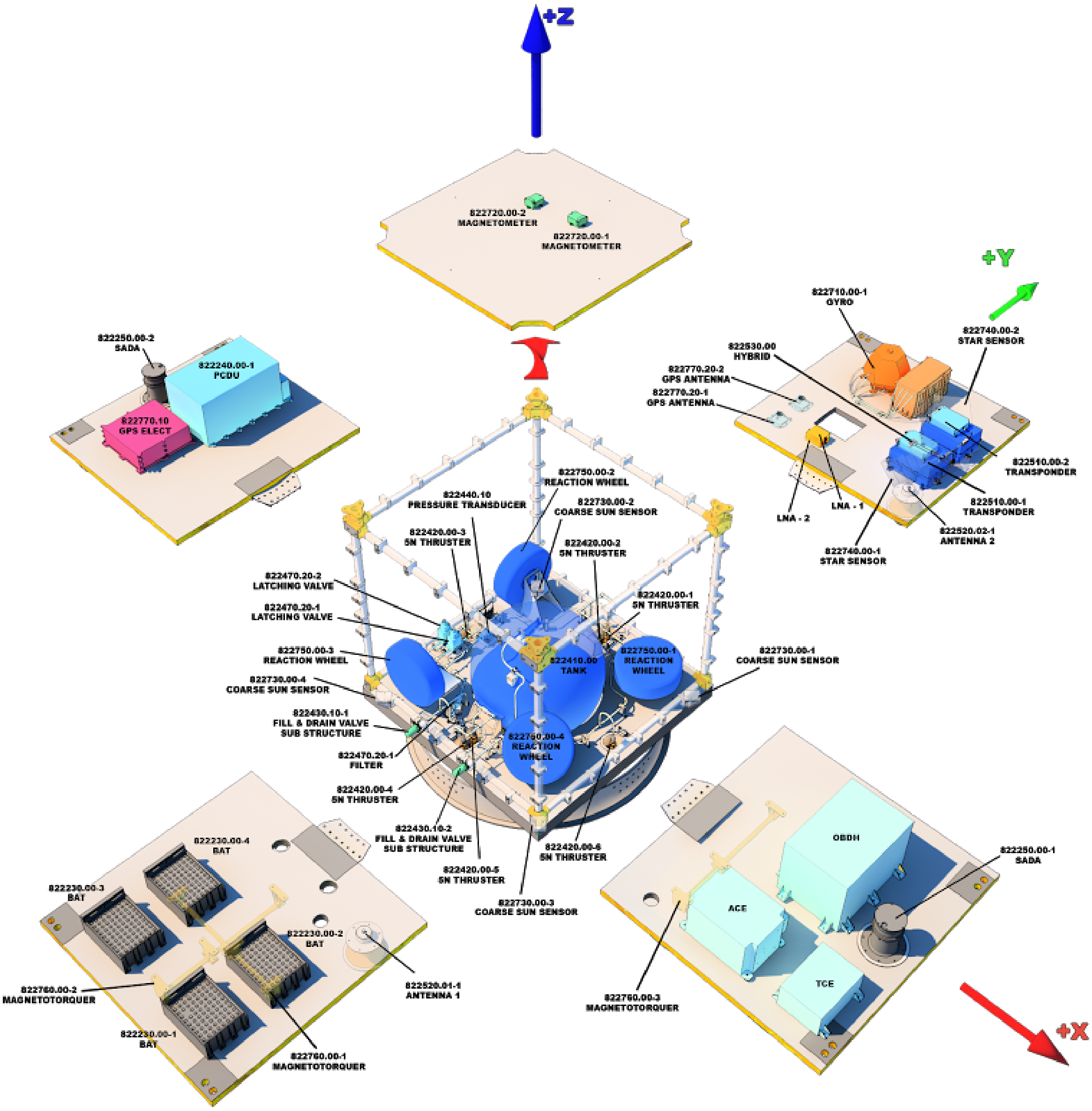

Figure 2. MMP blow-up illustration
(Courtesy of National Institute for Space Research, INPE)

III. Payload configuration

In the following itens the payload configuration is discussed.

A. Mesh Deployable Offset Reflector Antenna Design

The set of preliminary input parameters considered for the Reflector Antenna patterns is listed in Table 3. The antenna modeling was performed using TICRA-GRASP Student Edition® software, version 10.3.0. In all the cases studies, it was considered the right-circular transmit polarization (*Rhc*).

Table 3 Offset Reflector Antenna Design

Parameter	Symbol	Value
Sampling Frequency	*fs*	1.5GHz
Wavelength	λ	0.2 m
Reflector Diameter	*D*	7 m
Reflector Offset	*D'*	0.572 m
Reflector Clearance Aperture Efficiency	*m*	0.504 m

Considering the MMP dimensions, it was possible to use two channels in azimuth, following the concept of One-dimensionally Defocused Reflector Antennas, illustrated in Fig. 3, where the *y*-axis (green arrows) represents the coordinates of the elements willing along-track direction along which the satellite is moving. [38–40]

For the operation modes, we define *mode 1* when a single channel is fed, using 225W, and *mode 2* when both channels are fed. The mode 2 observes the limit of ten minutes for peak power consumption (Table 1).

In both operational modes, the echo signals received by each channel are amplified, digitized and processed by dedicated algorithms to allow the reconstruction of the high resolution image with *large swath*.

Notice that the term *large swath* is used in this work to represent values about 60 km, thus, very inferior to the 300 km expected for other missions such as Tandem-L. However, this approach considers the use of a small satellite, presenting a considerable gain comparing with the previous design adopted for MAPSAR. The MAPSAR mission analysis takes into account one horn to feed the Cassegrain antenna of the satellite. [35,36] This architecture enabled a swath illumination about 30 km in high resolution mode.

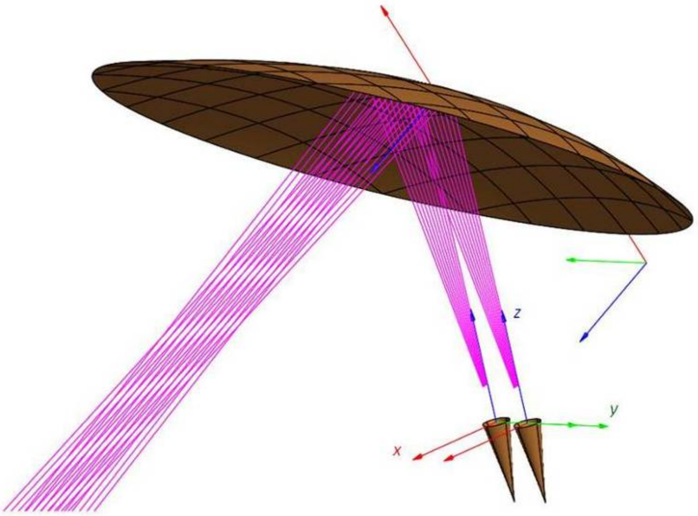

Figure 3. Offset Reflector Antenna illuminated by two feeds

For *mode 1*, the antenna gain pattern, depicted in Fig. 4(a), can reach values about 35 dB with the swath about 30 km, as suggested in MAPSAR high resolution mode.

For *mode 2*, the power rate is divided between the two channels. The antenna gain patterns reduces to about 14dB (Fig. 4(b)), but the bandwidth increases from 6º (at *mode 1*) to 8º. In this mode, the mechanical molding of the reflector dish allow illuminate a swath about 60 km.

If the channels are separated by 0.85m, the bandwidth increases almost to 10º. However, the antenna gain pattern significantly reduces to about 8 dB. [40] Therefore, the configuration adopted for BR-SAR assumes the two channels adjoined.

Figure 5 exhibits an artistic conception of BR-SAR spacecraft, using MMP bus associated with a 7 m mesh deployable Offset Reflector Antenna. The two swaths projected on the Earth represents the second mode mentioned before.

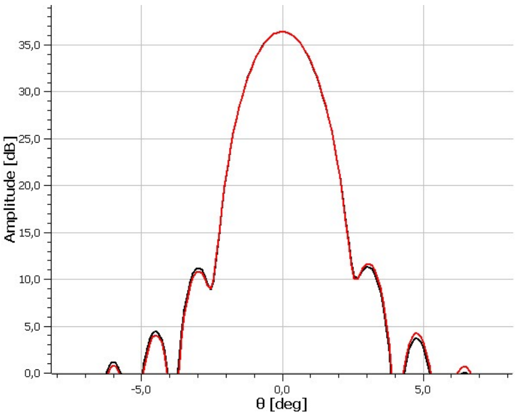

a) Reflector Antenna illuminated by single channel

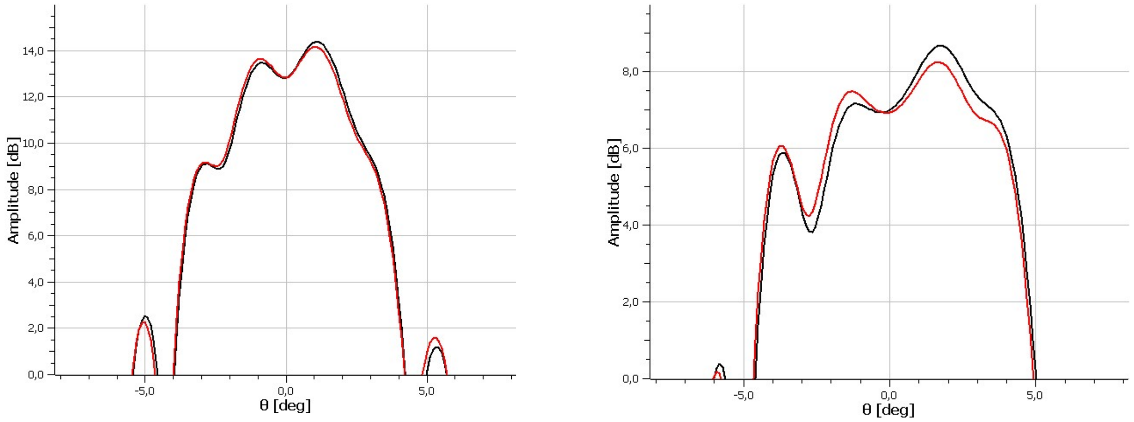

b) Reflector Antenna illuminated by two channels

c) Two channels displaced by 0.85 m

Figure 4. Reflector Antenna gain patterns.

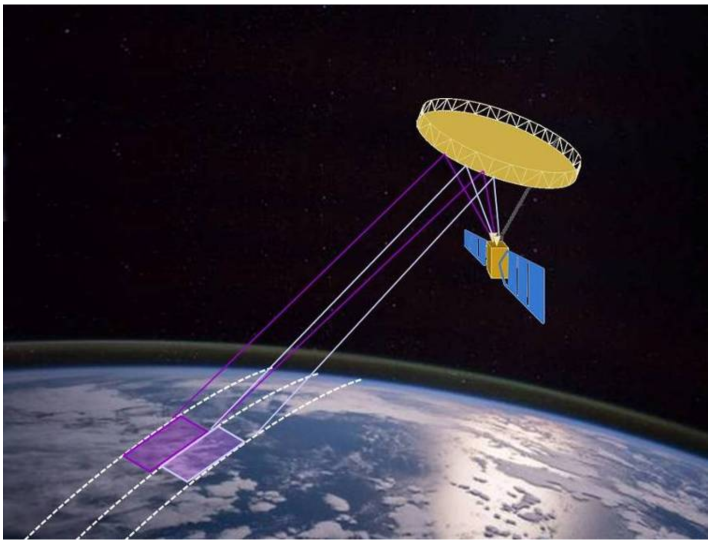

Figure 5. Artistic conception of BR-SAR spacecraft, using Brazilian Multi-Mission Platform (MMP) associated with a 7 m mesh deployable offset Reflector Antenna

B. Array Processing Design

The MMP is able to provide 225 W average power and 900 W peak power for 10 minutes (Table 1), allowing use an array in azimuth with two channels, *Rhc* polarized, aligned along-track direction. Three traveling wave tube amplifier (TWTA) provides the power that is combining in the High Power Summation Assembly (HPSA) with its "4 out of 6" redundancy to provide the necessary power to the operating modes (Fig. 6).

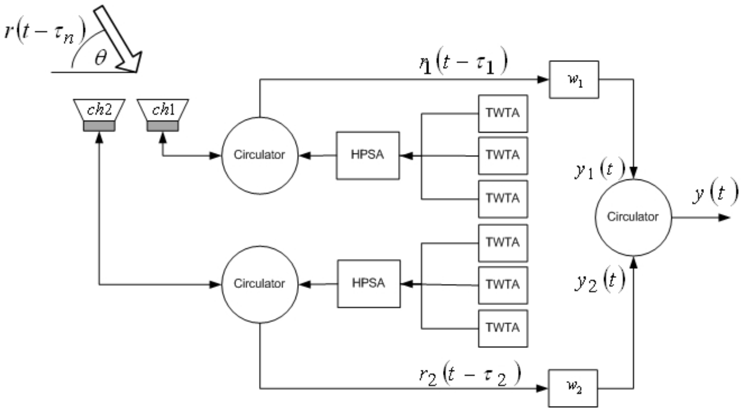

Figure 6. Array with linear processing

The bandpass signal $s(t)$ transmitted by the channels ($ch1$ and $ch2$) can be represented by

$$s(t,n)=\sqrt{2}\,\mathrm{Re}[\tilde{s}(t,n)\exp\{j\omega_c t\}],\ n=1,2\,, \tag{2}$$

where $\tilde{s}(t,n)$ is the complex envelope and ω_c is the carrier frequency in radian.

The echo signal $r(t)$ that arrives to the channels ($ch1$ and $ch2$) at θ angle (Fig. 6) is represented by

$$r(t,n)=a(\theta)\tilde{c}(t-\tau_n,n)G^2(t-\tau_n,n)\tilde{s}(t-\tau_n,n)+u(t-\tau_n,n), \tag{3}$$

where: $a(\theta)$ is the vector that incorporates all of the spatial characteristics of the feeder array for θ angle, called *array manifold*; $\tilde{c}(t,n)$ is the complex reflectivity of the target; τ_n is the signal delay for each channel; and $u(t,n)$ is the vector of additive noise. $^{40\text{–}42}$

The signal $r(t,n)$ can be rewritten and simplified in a vector notation as

$$\vec{r}(t,n)=[r(t-\tau_1)\ r(t-\tau_2)\ ]^T\,, \tag{4}$$

where $[\cdot]^T$ stands for the transpose matrix.

Considering that the array is a system with impulse response $h_n(\tau)$, each channel output is processed by a linear, time-invariant filter. The sum of the output gives the preliminary array output $y(t)$, which can be written in a vector notation as

$$y(t)=\int_{-\infty}^{\infty} h^T(t-\tau_n)r(\tau_n,n)d\tau, \tag{5}$$

where

$$\vec{h}(\tau)=[h_1(\tau_1)\ h_2(\tau_2)]^T\,. \tag{6}$$

In the frequency domain, expression (5) turns to

$$Y(\omega) = H^T(\omega)R(\omega). \tag{7}$$

Defining the complex weight vector as

$$\vec{w}_n^T = \lfloor w_1^* \; w_2^* \rfloor, \tag{8}$$

the array output $y_a(t)$ can be written as

$$y_a(t) = w_n^T y(t). \tag{9}$$

With the implementation of the weighted array, the signal-to-noise ratio (*SNR*) becames

$$SNR = \frac{\sigma \left| w_n^T a(\theta) \right|}{w_n^T u_c w_n}, \tag{10}$$

where u_c is the noise covariance matrix, expressed by

$$u_c = \mathrm{E}\left\{ u(t,n) u^T(t,n) \right\}, \tag{11}$$

and $\mathrm{E}\{\cdot\}$ is the expected value. [43]

Finally, considering that both channels have the same and uncorrelated white noise $u(t,n)$, the gain of the array G_a associated to a Reflector Antenna of the BR-SAR can be summarizing as [40,42,43]

$$G_a = \frac{\left| w^T a(\theta) \right|^2}{w^T w}. \tag{12}$$

C. Compact Polarimetry Technique

CP was introduced by Souyris, in 2005, as a partial polarimetry design. The purpose was to reduce cost and the complexity of the space segments. Over the years, the development of new techniques has resulted in several advantages over traditional polarimetric modes, e.g., the increase of gain and swath, mass reduction, data rate increasing, cost and complexity reduction. [25–29,44,45]

Nowadays, there are two spaceborne SAR using CP for Earth observation: Radar Imaging Satellite-1 (Risat-1), launched in April 2012; and Advanced Land Observing Satellite-2 (ALOS-2), launched in May 2014. [26,46] It is expected that new missions as Radarsat Constellation, NISAR, Risat-1A, can be launched in the next five years incorporating this technique. A brief survey on the CP literature shows that the researches conducted in the last ten years have been used pseudo-reconstructions from full-pol data, because only recently SAR satellites using CP techniques.[34]

In order to analyse the signals received by CP, we consider a *Rhc* radar signal $s(t,n)$ from the origin of the channels coordinate system, illustred at Fig. 3. For $z = 0$, the Jones vector represented by x and y components of the electric field $\vec{E}$ can be expressed by

$$\vec{E} = \begin{bmatrix} E_x \exp\{j\delta_x\} \\ E_y \exp\{j\delta_y\} \end{bmatrix}, \tag{12}$$

where $E_{x,y}$ are the amplitudes of the x and y components of electrical field E, respectively, and the $\delta_{x,y}$ are their respective phases. For a unit *Rhc* Jones vector $\vec{E}_{Rhc}$,[47] expression (12) can be represented by

$$\vec{E}_{Rhc} = \frac{1}{\sqrt{2}}\begin{bmatrix} 1 \\ -j \end{bmatrix}. \tag{13}$$

Considering the scattering process on the ground and the basic concepts of the electromagnetic theory, we can define the incident electric field and the scattered electric field with the notation of the signal transmitted and received, respectively, as

$$r(t,n) = \frac{\exp\{-j\omega_c/c\}}{r_0} S\, s(t,n), \tag{14}$$

where c is the speed of light, r_0 is the range from the SAR sensor to the target, and S is the Sinclair matrix, or scattering matrix. For a tipical full-pol SAR, S can be respresented by

$$S = \begin{bmatrix} S_{HH} & S_{HV} \\ S_{VH} & S_{VV} \end{bmatrix}, \tag{15}$$

where $S_{i,j}$ is the complex backscatter coefficient with i transmit and j receive polarization.[48]

Following the concepts proposed by Raney[45] for the CP-SAR data reconstruction from full-pol SAR, we define the scattering vector k_{Rhc} from equations (14) and (15) as

$$\vec{k}_{Rhc} = \frac{1}{\sqrt{2}}\begin{bmatrix} S_{HH} & S_{HV} \\ S_{VH} & S_{VV} \end{bmatrix}\begin{bmatrix} 1 \\ -j \end{bmatrix} = \frac{1}{\sqrt{2}}\begin{bmatrix} S_{HH} - jS_{HV} \\ S_{VH} - jS_{VV} \end{bmatrix}. \tag{16}$$

So, the Covariance Matrix C_{Rhc} is given by

$$C_{Rhc} = \left\langle \vec{k}_{Rhc} \cdot \vec{k}^{*T}_{Rhc} \right\rangle =$$
$$\left\langle \begin{bmatrix} |S_{HH}|^2 & j\left(S_{HH}S^*_{VV}\right) \\ -j\left(S^*_{HH}S_{VV}\right) & |S_{VV}|^2 \end{bmatrix} + \begin{bmatrix} |S_{HV}|^2 & -j|S_{HV}|^2 \\ j|S_{HV}|^2 & |S_{HV}|^2 \end{bmatrix} + \begin{bmatrix} -2\Im\left(S_{HH}S^*_{VV}\right) & S_{HH}S^*_{HV} + S_{HV}S^*_{VV} \\ S^*_{HH}S_{HV} + S^*_{HV}S_{VV} & -2\Im\left(S^*_{HV}S_{VV}\right) \end{bmatrix} \right\rangle \tag{17}$$

where $\langle\cdot\rangle$ is the spatial or temporal averaging and the $\left({}^{*T}\right)$ is the complex conjugate transpose. As pointed out by Denbina,[25] the first matrix on the right-hand side of equation (17) presents only the co-polarization terms, the second one contains only cross-polarization terms and the last one consist of the product of both referred terms. [25,30,34,40,49,50]

Figure 7 presents a Radarsat-2 full-pol data acquired with the fine quad beam mode over the Vancouver city (Canada), processed with PolSARpro v5.0 Software (Polarimetric SAR Data Processing and Educational Toolbox). Some parameters of the product file are show in Table 3.

Table 3 Radarsat-2 Product File

Parameter	Value
Beam	FQ15
Acq. Date/Time	2008-05-06/14:25:39
Inc. Angle(°)	34.49-36.08
Az. Spacing (m)	4.73

Figure 7(a) shows a Pauli decomposition[47] where the Pauli scattering vector $\vec{k}_p$ can be represented by

$$\vec{k}_p = \frac{1}{\sqrt{2}}\left[\left(S_{HH} + S_{VV}\right) \ \left(S_{HH} - S_{VV}\right) \ \left(S_{HV} + S_{VH}\right) \ j\left(S_{HV} - S_{VH}\right)\right]^T, \tag{18}$$

and Fig. 7(b) is a CP decomposition using k_{Rhc} instead of the scattering vector S in equation (14).

This simple example shows that the scattering characteristics of the sea are more evident at the CP decomposition.

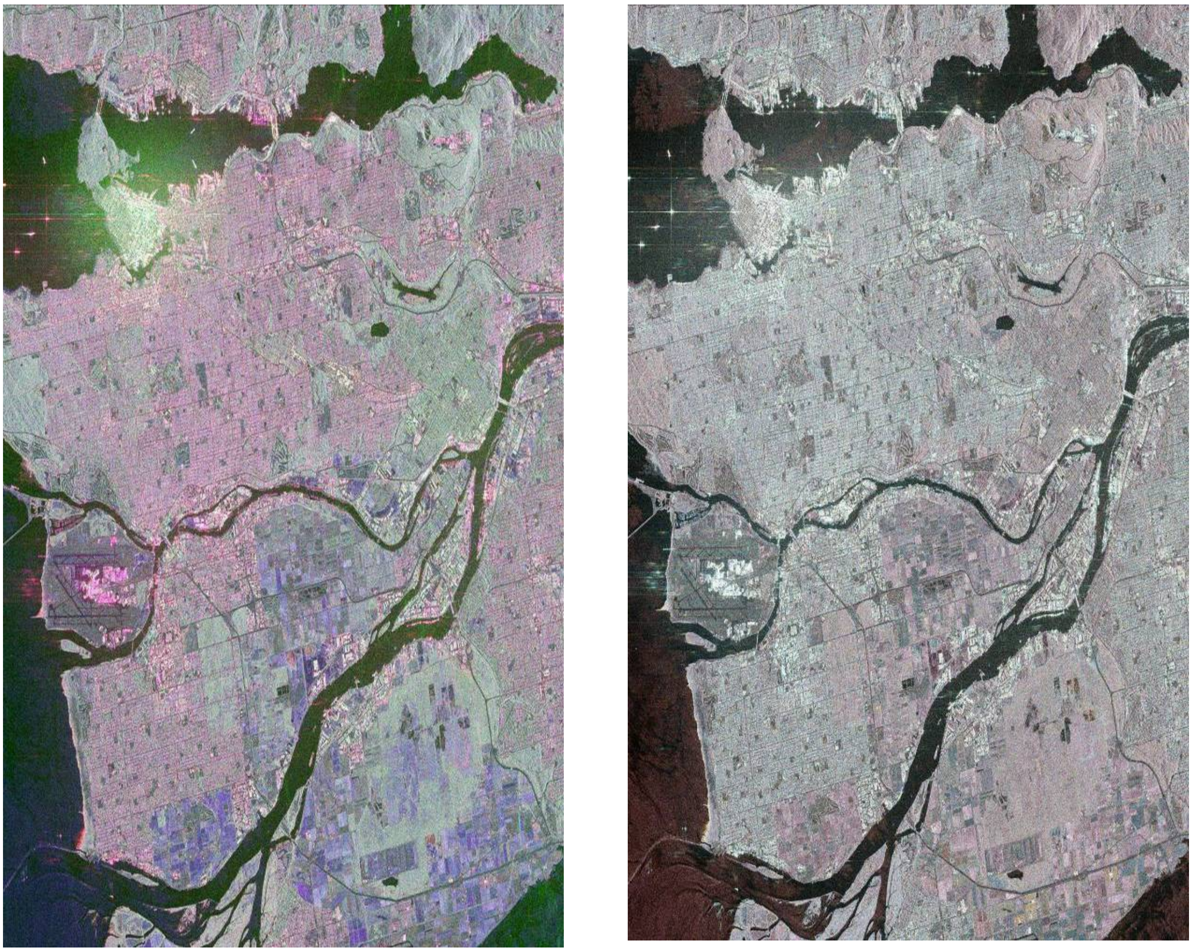

a) Pauli decomposition **b) CP decomposition**

Figure 7. Decompositions from Radarsat-2 full-pol data acquired with the fine quad beam mode over the Vancouver city (Canada)

Conclusion

In this paper we review a previous proposal of a small satellite mission with a L-Band SAR, MAPSAR and we introduce a new mission proposal named as BR-SAR. A Mesh Deployable Offset Reflector Antenna has been used and the Compact Polarimetry technique has been explored in order to double the swath in high resolution mode. This preliminary study indicates that with the new configuration it is feasible to enlarge the swath using the same spacecraft bus of MAPSAR, the MMP. Additionally, the use of CP techniques can provide a reduction of the mission cost.

The next steps will include a mission analysis, scheduled for the next months, and an experimental evaluation of CP performace, which, at the best of our knowledge, has not been fully explored yet.

Acknowledgment

The authors thank the Brazilian Navy Department of Science Technology and Innovation (SecCTM) and the Technological Institute of Aeronautics (ITA) for the financial support and incentive. Furthermore, the authors thank the Institute for Advanced Studies (IEAv), the National Institute for Space Research (INPE), the Brazilian Navy

Research Institute (IPqM), Brazilian Navy Electronic Warfare Center (CGEM), and the Space System Coordination and Implementation Comission (CCISE) for the support, partnership, and incentive in this doctoral research.

References

[1] Larson, W. J., and Wertz, J. R., *Space Mission Analysis and Design*, Dordrecht: Microcosm Press, 2005.

[2] Tibert, G., "Deployable Tensegrity Structures for Space Applications," Royal Institute of Technology, 2002.

[3] Entekhabi, D. et al., *SMAP Handbook*, Pasadena, California: National Aeronautics and Space Administration - NASA, 2014.

[4] Mobrem, M., Kuehn, S., Spier, C., and Slimko, E., "Design and performance of Astromesh reflector onboard Soil Moisture Active Passive spacecraft," *IEEE Aerospace Conference Proceedings*, Big Sky, MT: IEEE, 2012, pp. 1 – 10.

[5] Imbriale, W. A., Gao, S. S., and Boccia, L., *Space Antenna Handbook*, Noida, India: John Wiley & Sons, Inc, 2012.

[6] Jordin T. Kare, "Moving Receive Beam Method and Apparatus for Synthetic Aperture Radar," 6175326B1, 2001.

[7] Moreira, A., Prats-iraola, P., Younis, M., Krieger, G., Hajnsek, I., and Papathanassiou, K. P., "A Tutorial on Synthetic Aperture Radar," *Geoscience and Remote Sensing Magazine, IEEE*, 2013, pp. 6 – 43.

[8] Krieger, G., Hajnsek, I., Papathanassiou, K. P., Younis, M., and Moreira, A., "Interferometric Synthetic Aperture Radar (SAR) Missions Employing Formation Flying," *Proceedings of the IEEE*, vol. 98, 2010, pp. 816–843.

[9] Cole, S., Buis, A., Diller, G., and Gran, R., "SMAP - Soil Moisture Active Passive," 2015.

[10] Krieger, G., Younis, M., Gebert, N., Huber, S., Bordoni, F., Patyuchenko, A., and Moreira, A., "Advanced Concepts for High-Resolution Wide-Swath SAR Imaging Multi-Channel ScanSAR Mode," 2010, pp. 524–527.

[11] Freeman, T., Rosen, P., Johnson, B., Jordan, R., and Shen, Y., "DESDynI A NASA Mission for Ecosystems , Solid Earth and Cryosphere Science," 2008.

[12] Freeman, a., Krieger, G., Rosen, P., Younis, M., Johnson, W. T. K., Huber, S., Jordan, R., and Moreira, a., "SweepSAR: Beam-forming on receive using a reflector-phased array feed combination for spaceborne SAR," *IEEE National Radar Conference - Proceedings*, 2009.

[13] Cantafio, L. J., *Space-based Radar Handbook*, Norwood, MA 02062: Artech House Radar Library, 1989.

[14] Liangbo, Z., Jie, L., Changjiang, Z., and Zhenxing, W., "Considerations of spaceborne SAR system design," *Radar Conference 2013, IET International*, Xi'an: IET, 2013, pp. 1 – 6.

[15] Hajnsek, I., "Tandem-L : Science Requirements and Mission Concept," 2014, pp. 1255–1258.

[16] Moreira, A., Hajnsek, I., Krieger, G., Papathanassiou, K., and Eineder, M., "Tandem-L: Monitoring the Earth's Dynamics with InSAR and Pol-InSAR," *Proc. of "4th Int. Workshop on SCience and Applications of SAR Polarimetry and Polarimetric Interferometry - PolInSAR 2009,"* Frascati, Italy: ESA SP-668, 2009, pp. 26–30.

[17] Costa, M. S. M., and Fernandes, D., "Análise do Emprego de uma Constelação de Pequenos Satélites SAR em Vigilância Marítima .," *XVI Simpósio de Aplicações Operacionais em Áreas de Defesa - XVI SIGE*, São José dos Campos: Instituto Tecnológico de Aeronáutica, 2014, pp. 90–95.

[18] Krieger, G., Hajnsek, I., Papathanassiou, K., Eineder, M., Younis, M., Zan, F. De, Prats, P., Huber, S., Werner, M., Fiedler, H., Freeman, A., Rosen, P., Hensley, S., Johnson, W., Veilleux, L., Grafmueller, B., Werninghaus, R., Bamler, R., and Moreira, A., "The Tandem-L Mission Proposal : Monitoring Earth ' s Dynamics with High Resolution SAR Interferometry," 2009, pp. 0–5.

[19] Krieger, G., Gebert, N., Younis, M., and Moreira, A., "Advanced synthetic aperture radar based on digital beamforming and waveform diversity," *Radar Conference, 2008. RADAR '08. IEEE*, Rome: IEEE, 2008, pp. 1–6.

[20] Younis, M., Huber, S., Patyuchenko, A., Bordoni, F., and Krieger, G., "Performance Comparison of Reflector- and Planar-Antenna Based Digital Beam-Forming SAR," *International Journal of Antennas and Propagation*, vol. 2009, 2009, pp. 1–13.

[21] Moreira, A., Krieger, G., Hajnsek, I., Papathanassiou, K., Younis, M., Lopez-Dekker, P., Huber, S., Villano, M., Pardini, M., Eineder, M., De Zan, F., and Parizzi, A., "Tandem-L: A Highly Innovative Bistatic SAR Mission for Global Observation of Dynamic Processes on the Earth's Surface," *IEEE Geoscience and Remote Sensing Magazine*, vol. 3, 2015, pp. 8–23.

[22] Younis, M., Patyuchenko, A., Huber, S., Krieger, G., and Moreira, A., "A concept for high performance reflector-based Synthetic Aperture Radar," *Geoscience and Remote Sensing Symposium (IGARSS), 2010 IEEE International*, Honolulu, HI: IEEE, 2010, pp. 249–252.

23 Süss, M., and Wiesbeck, W., “Side-looking synthetic aperture radar system,” EP1241487, 2002.

24 McKenzie, I., Karafolas, N., and Van Loock, P., “Microphotonics in satellite payloads and platforms,” *International Conference on Optical MEMS and Nanophotonics*, Glasgow: IEEE, 2014, pp. 19–20.

25 Denbina, M., “Iceberg Detection Using Compact Polarimetric Synthetic Aperture Radar,” University of Calgary, 2014.

26 Atteia, G. E., and Collins, M. J., “On the use of compact polarimetry SAR for ship detection,” *ISPRS Journal of Photogrammetry and Remote Sensing*, vol. 80, 2013, pp. 1–9.

27 Souyris, J. C., Imbo, P., Fjørtoft, R., Mingot, S., and Lee, J. S., “Compact polarimetry based on symmetry properties of geophysical media: The π/4 mode,” *IEEE Transactions on Geoscience and Remote Sensing*, vol. 43, 2005, pp. 634–645.

28 Boularbah, S., Ouarzeddine, M., and Belhadj-Aissa, A., “Investigation of the capability of the Compact Polarimetry mode to Reconstruct Full Polarimetry mode using RADARSAT2 data,” *Advanced Electromagnetics*, vol. 1, 2012, p. 19.

29 Guo, S., Tian, Y., Li, Y., Chen, S., and Hong, W., “UNSUPERVISED CLASSIFICATION BASED ON H / ALPHA DECOMPOSITION AND WISHART CLASSIFIER FOR COMPACT POLARIMETRIC SAR 1 . Institute of Electronics , Chinese Academy of Sciences , Beijing , 100190 , China 2 . University of Chinese Academy of Sciences , Beijing ,” vol. 1, 2015, pp. 1614–1617.

30 Lavalle, M., “Full and Compact Polarimetric Radar Interferometry for Vegetation Remote Sensing,” Institut d’Electronique et de Télécommunications de Rennes, 2010.

31 Shirvany, R., “Estimation of the Degree of Polarization in Polarimetric SAR Imagery: Principles & Applications,” Institut National Polytechnique de Toulouse (INP Toulouse), 2012.

32 Panigrahi, R. K., “Information Extraction from Polarimetric SAR Images,” Indian Institute of Technology Guwahati, 2011.

33 Liu, C., Vachon, P. W., English, R. A., and Sandirasegaram, N., *Ship detection using RADARSAT-2 Fine Quad Mode and simulated compact polarimetry data*, Ottawa: 2010.

34 Collins, M. J., Denbina, M., and Atteia, G., “On the Reconstruction of Quad-Pol SAR Data From Compact Polarimetry Data For Ocean Target Detection,” *IEEE Transactions on Geoscience and Remote Sensing*, vol. 51, 2013, pp. 591–600.

35 *MAPSAR - Phase A: Study Final Report*, São José dos Campos: 2007.

36 Schröder, R., Puls, J., Hajnsek, I., Jochim, F., Neff, T., Kono, J., Paradella, W. R., Silva, M. M. Q. Da, De Valeriano, D. M., and Costa, M. P. F., “MAPSAR: A small L-band SAR mission for land observation,” *Acta Astronautica*, vol. 56, 2005, pp. 35–43.

37 Office, C. B., “Alternatives for Military Space Radar,” 2007.

38 Yang, R., and Andrew Corporation, Chicago, I., “Illuminating curved passive reflector with defocused parabolic antenna,” *WESCON/58 Conference Record (Volume:2)*, IEEE, 1958, pp. 260–265.

39 Olver, A. D., and Syed, J. U. I., “Variable beamwidth reflector antenna by feed defocusing,” *IEE Proceedings - Microwaves, Antennas and Propagation (Volume:142 , Issue: 5)*, vol. 142, 1995, pp. 2–6.

40 Huber, S., “Spaceborne SAR Systems with Digital Beamforming and Reflector Antenna,” 2013.

41 Trees, H. L. Van, *Detection, Esimation, and Modulation Theory. Part I*, New York, NY: John Wiley & Sons, Inc., 2001.

42 Melo, R. L., “Digital beamformers applied to reflector based synthetic aperture radar system,” 2013.

43 Trees, H. L. Van, *Detection, Estimation, and Modulation Theory, Optimum Array Processing*, New York, NY: John Wiley & Sons, Inc., .

44 Souyris, J., and Mingot, S., “Polarimetry based on one transmitting and two receiving polarizations : the π /4 mode,” vol. 00, 2002, pp. 629–631.

45 Raney, R. K., “Hybrid-Polarity SAR Architecture,” *IEEE Transactions on Geoscience and Remote Sensing*, vol. 45, 2007, pp. 3397–3404.

46 Yokota, Y., Nakamura, S., Endo, J., Suwa, K., Endo, T., Tsuji, M., Hariu, K., Kankaku, Y., Suzuki, S., and Shimada, M., “Evaluation of compact polarimetry and along track interferometry as experimental mode of PALSAR-2,” *Proceedings of IEEE International Geoscience and Remote Sensing Symposium (IGARSS’15)*, Milan: IEEE, 2015, pp. 4125–4128.

47 Lee, J. S., and Pottier, E., *Polarimetric Radar Imaging*, Boca Raton, FL: CRC Press, 2009.

48 Atteia Allah, G. E. M., “On the Use of Hybrid Compact Polarimetric SAR for Ship Detection,” University of Calgary, 2014.

49 James B. Campbell, *Introduction to Remote Sensing*, New York, NY: The Guilford Press, 2007.

[50] Paes, R. L., "Detecção de Alvos no Mar em Imagens SAR Explorando Recursos da Polarimetria Compacta em Modo Híbrido," Instituto Nacional de Pesquisas Espaciais, 2015.

APPENDIX E – Tables and Figures of the results from Section 5.3

e.1 Faraday Rotation angle $\Psi = 0°$

Table E.3 – Statistics of the images for $\Psi = 0°$.

Pearson correlation coefficient			
Method/Image	Mhh	Mhv	Mvv
Souyris	0.96	0.65	0.95
Nord	0.96	0.65	0.96
CP_{az}	0.96	0.67	0.95

a) Pearson correlation coefficient

RMSE			
Method/Image	Mhh	Mhv	Mvv
Souyris	382.12	685.85	257.57
Nord	411.31	684.29	294.01
CP_{az}	383.68	1106.57	258.72

b) RMSE

Maximum amplitude value of the images for each channel			
Max/Image	HH	HV	VV
Full-POL	29333.50	9686.87	17455.60
Souyris	30056.70	17562.80	15821.30
Nord	30056.70	17562.80	15821.30
CP_{az}	30056.70	30021.40	15821.30

c) Maximum amplitude value of the images for each channel

RMSE percentage error			
Max/Image	HH	HV	VV
Souyris	0.01	0.04	0.02
Nord	0.01	0.04	0.02
CP_{az}	0.01	0.04	0.02

d) RMSE percentage error

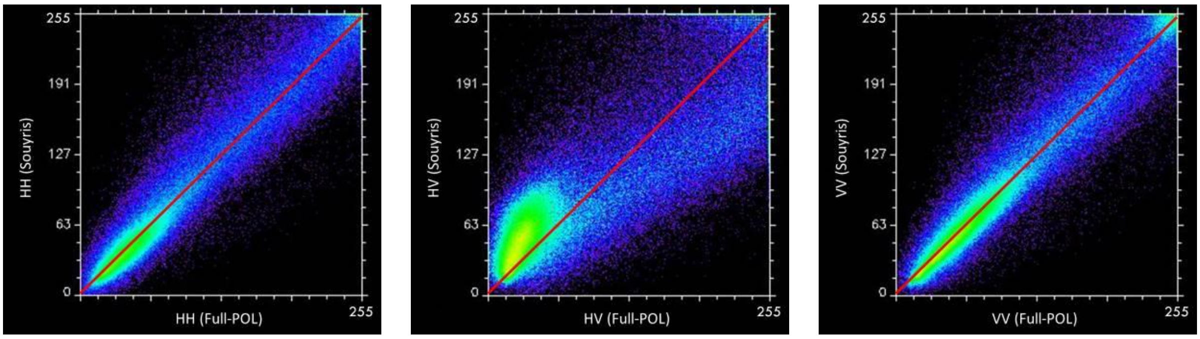

HH (Full-POL x Souyris) HV (Full-POL x Souyris) VV (Full-POL x Souyris)

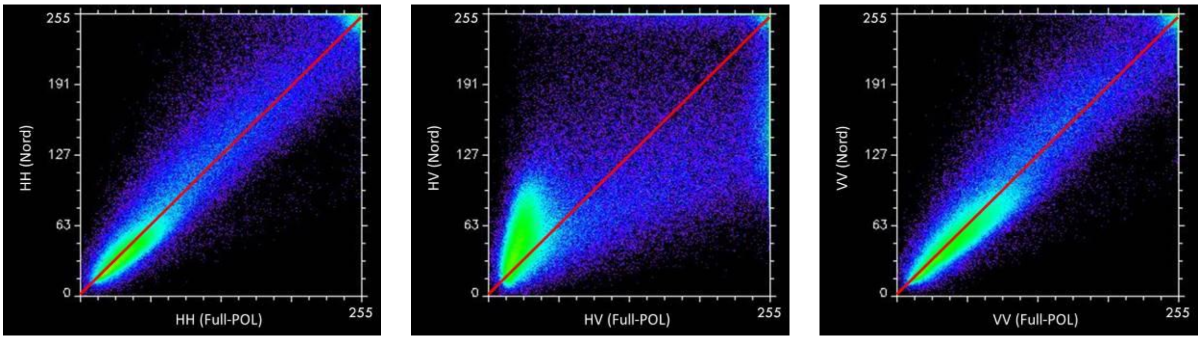

HH (Full-POL x Nord) HV (Full-POL x Nord) VV (Full-POL x Nord)

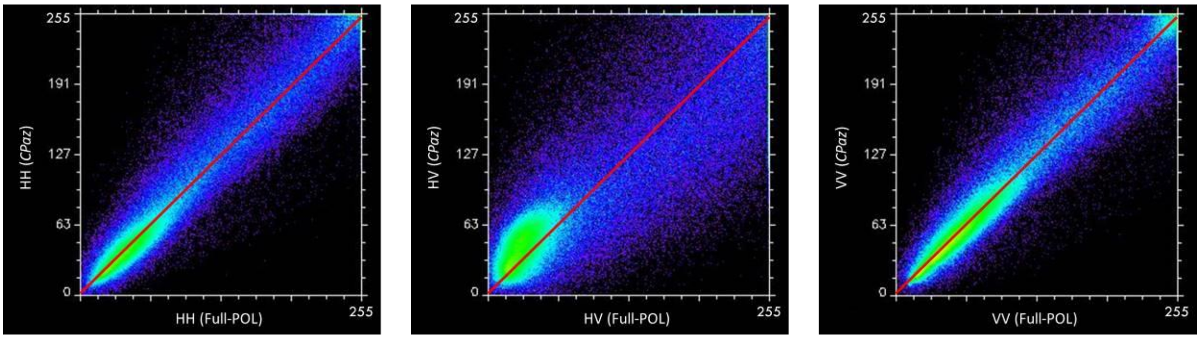

HH (Full-POL x CP_{az}) HV (Full-POL x CP_{az}) VV (Full-POL x CP_{az})

Figure E.31 – Scatter plots HH, HV, and VV of original dataset (Full-POL), Souyris, Nord, and CP_{az} algorithm when $\Psi = 0°$.

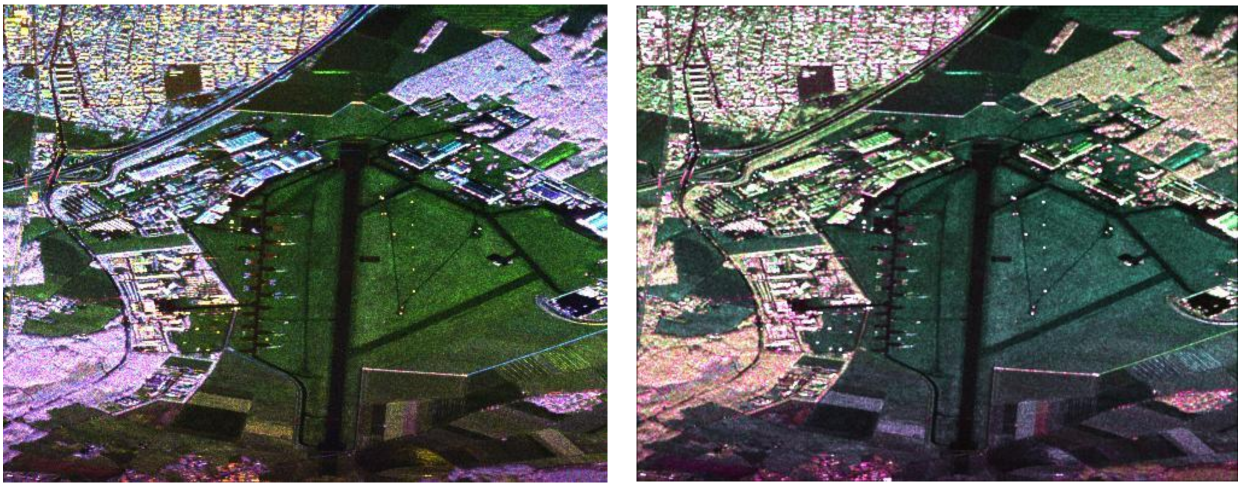

a) RGB E-SAR image.

b) RGB pseudo reconstruction by Souyris.

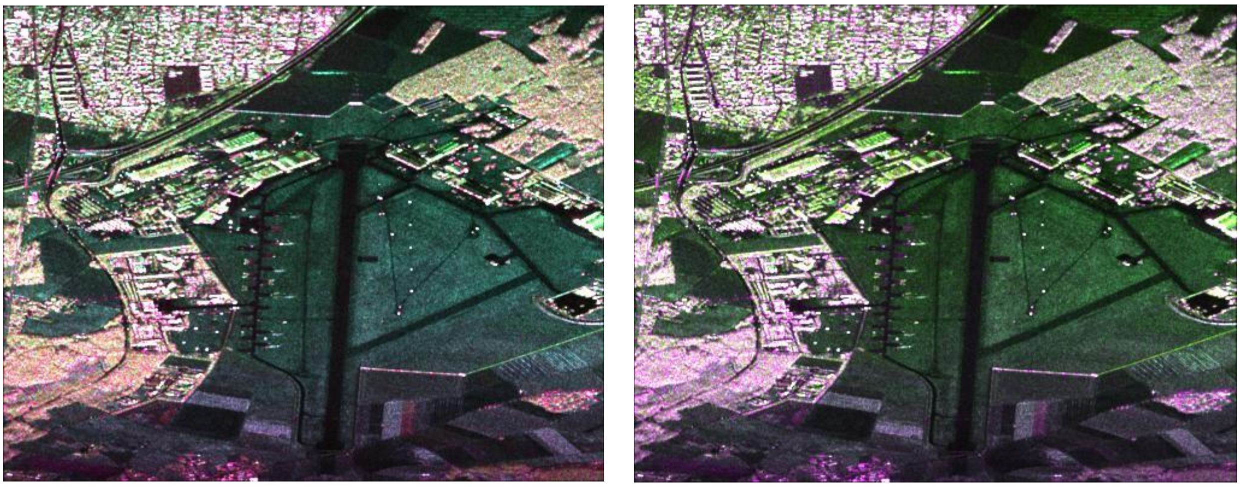

c) RGB pseudo reconstruction by Nord.

d) RGB pseudo reconstruction by CP_{az} algorithm.

Figure E.32 – Comparison of the Full-POL image with the pseudo reconstruction by Souyris, Nord, and CP_{az} algorithm.

e.2 Faraday Rotation angle $\Psi = 10°$

Table E.4 – Statistics of the images for $\Psi = 10°$.

Pearson correlation coefficient			
Method/Image	Mhh	Mhv	Mvv
Souyris	0.96	0.74	0.95
Nord	0.96	0.75	0.95
CP_{az}	0.96	0.77	0.95

a) Pearson correlation coefficient

RMSE			
Method/Image	Mhh	Mhv	Mvv
Souyris	397.73	576.08	289.50
Nord	417.12	578.12	314.79
CP_{az}	396.50	971.32	288.09

b) RMSE

Maximum amplitude value of the images for each channel			
Max/Image	HH	HV	VV
Full-POL	28572.70	14999.20	17111.60
Souyris	31498.10	16955.30	18583.90
Nord	31498.10	16955.30	18583.90
CP_{az}	31498.10	31464.40	18583.90

c) Maximum amplitude value of the images for each channel

RMSE percentage error			
Max/Image	HH	HV	VV
Souyris	0.01	0.03	0.02
Nord	0.01	0.03	0.02
CP_{az}	0.01	0.03	0.02

d) RMSE percentage error

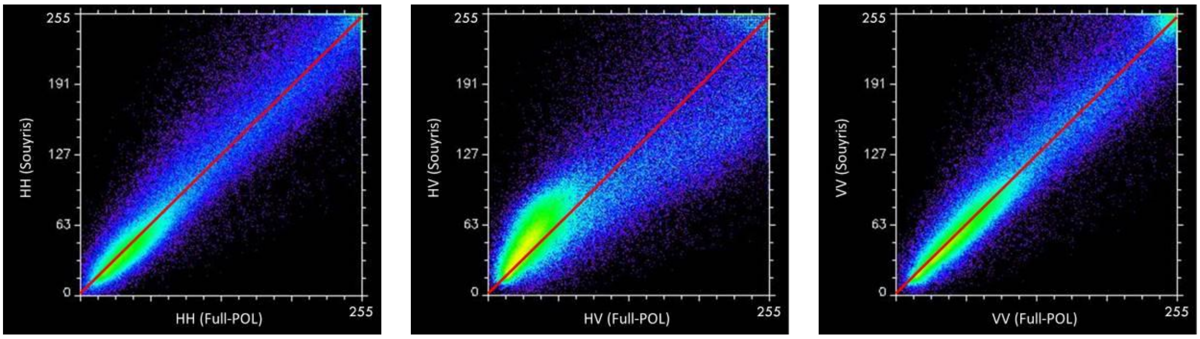

HH (Full-POL x Souyris) HV (Full-POL x Souyris) VV (Full-POL x Souyris)

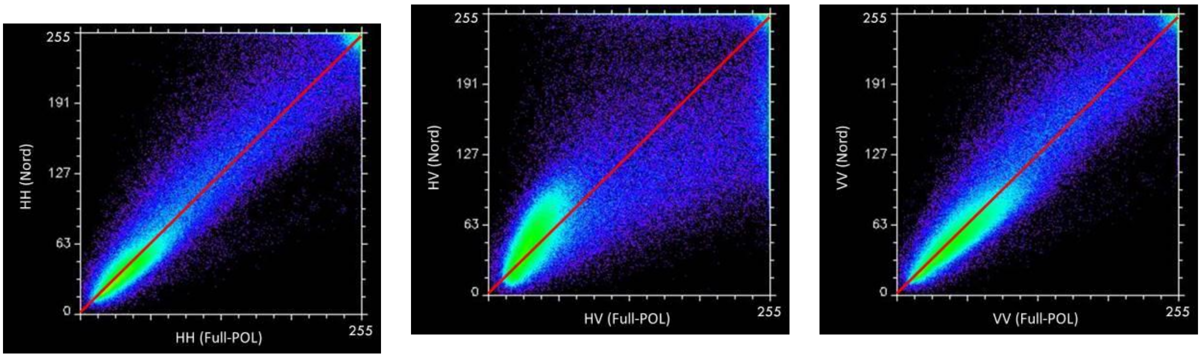

HH (Full-POL x Nord) HV (Full-POL x Nord) VV (Full-POL x Nord)

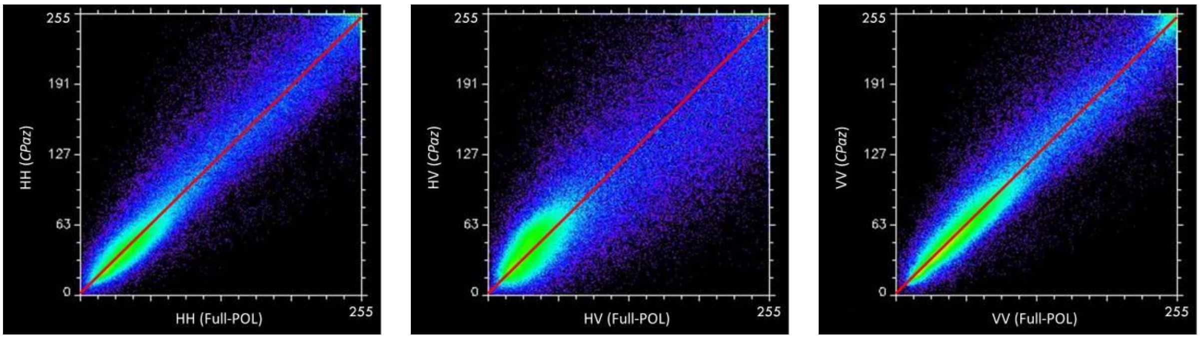

HH (Full-POL x *CPaz*) HV (Full-POL x *CPaz*) VV (Full-POL x *CPaz*)

Figure E.33 – Scatter plots HH, HV, and VV of original dataset (Full-POL), Souyris, Nord, and CP_{az} algorithm when $\Psi = 10^\circ$.

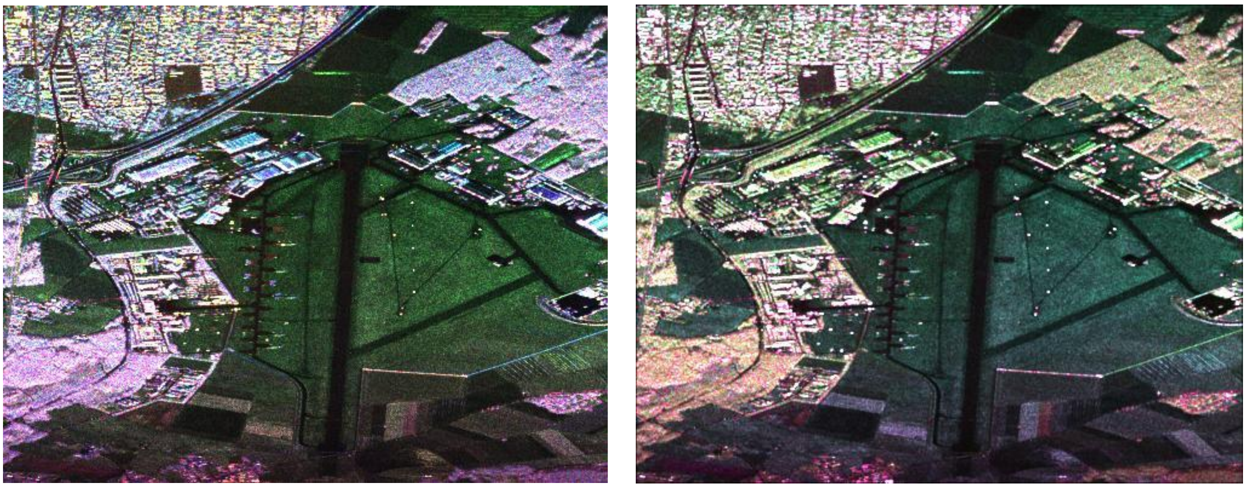

a) RGB E-SAR image.

b) RGB pseudo reconstruction by Souyris.

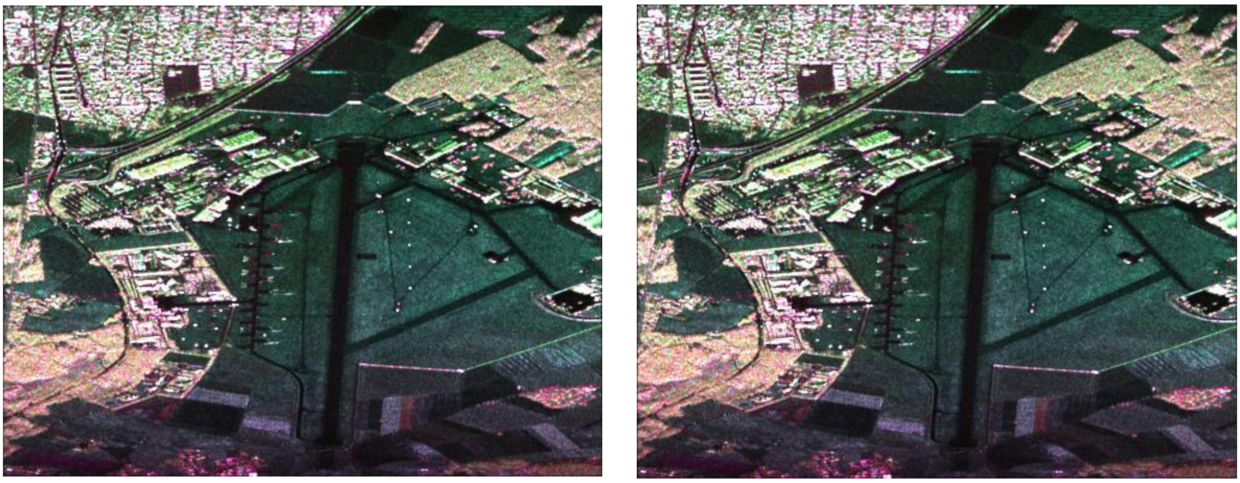

c) RGB pseudo reconstruction by Nord.

d) RGB pseudo reconstruction by CP_{az} algorithm.

Figure E.34 – Comparison of original dataset (Full-POL), Souyris, Nord, and CP_{az} algorithm when $\Psi = 10°$.

e.3 Faraday Rotation angle $\Psi = 20°$

Table E.5 – Statistics of the images for $\Psi = 20°$.

Pearson correlation coefficient			
Method/Image	Mhh	Mhv	Mvv
Souyris	0.96	0.83	0.93
Nord	0.96	0.84	0.93
CP_{az}	0.96	0.84	0.93

a) Pearson correlation coefficient

RMSE			
Method/Image	Mhh	Mhv	Mvv
Souyris	451.80	483.18	399.93
Nord	459.61	483.15	410.94
CP_{az}	438.35	753.48	381.91

b) RMSE

Maximum amplitude value of the images for each channel			
Max/Image	HH	HV	VV
Full-POL	26441.40	20019.30	16400.20
Souyris	32074.50	18465.00	22395.90
Nord	32074.50	18465.00	22395.90
CP_{az}	32074.50	32041.40	22395.90

c) Maximum amplitude value of the images for each channel

RMSE percentage error			
Max/Image	HH	HV	VV
Souyris	0.01	0.03	0.02
Nord	0.01	0.03	0.02
CP_{az}	0.01	0.03	0.02

d) RMSE percentage error

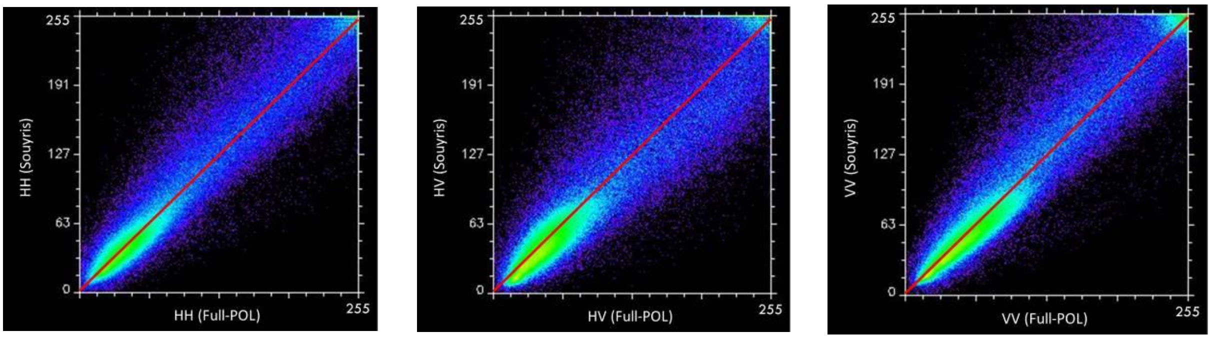

HH (Full-POL x Souyris) HV (Full-POL x Souyris) VV (Full-POL x Souyris)

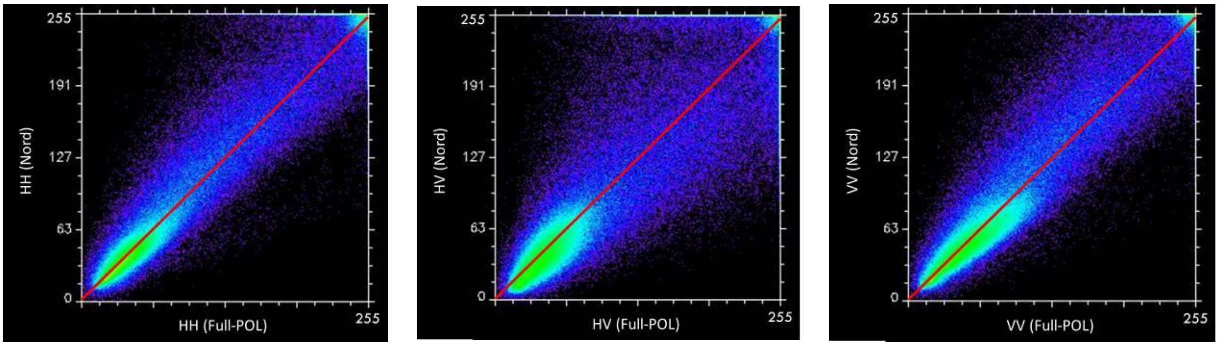

HH (Full-POL x Nord) HV (Full-POL x Nord) VV (Full-POL x Nord)

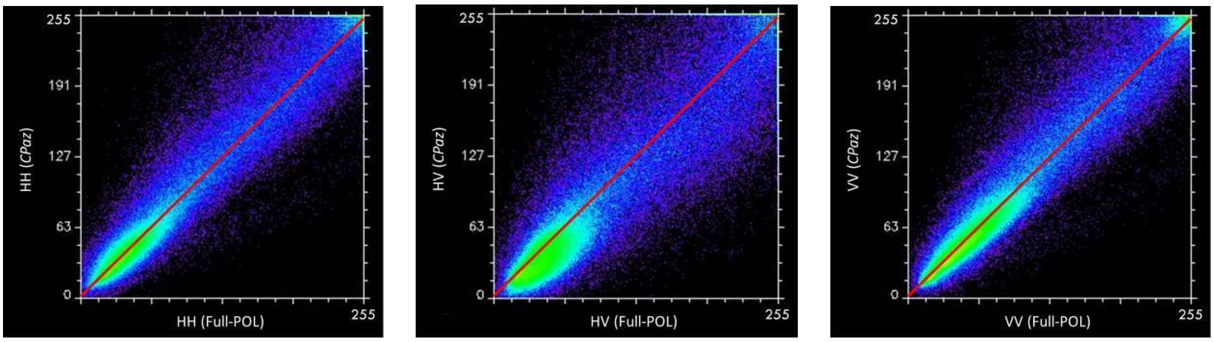

HH (Full-POL x CP_{az}) HV (Full-POL x CP_{az}) VV (Full-POL x CP_{az})

Figure E.35 – Scatter plots HH, HV, and VV of original dataset (Full-POL), Souyris, Nord, and CP_{az} algorithm when $\Psi = 20^\circ$.

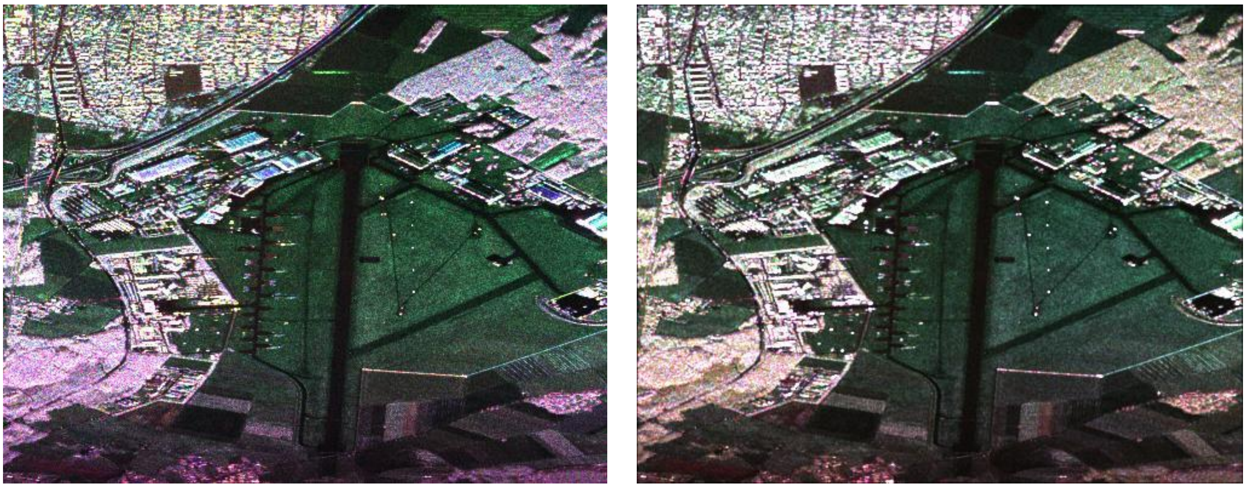

a) RGB E-SAR image.

b) RGB pseudo reconstruction by Souyris.

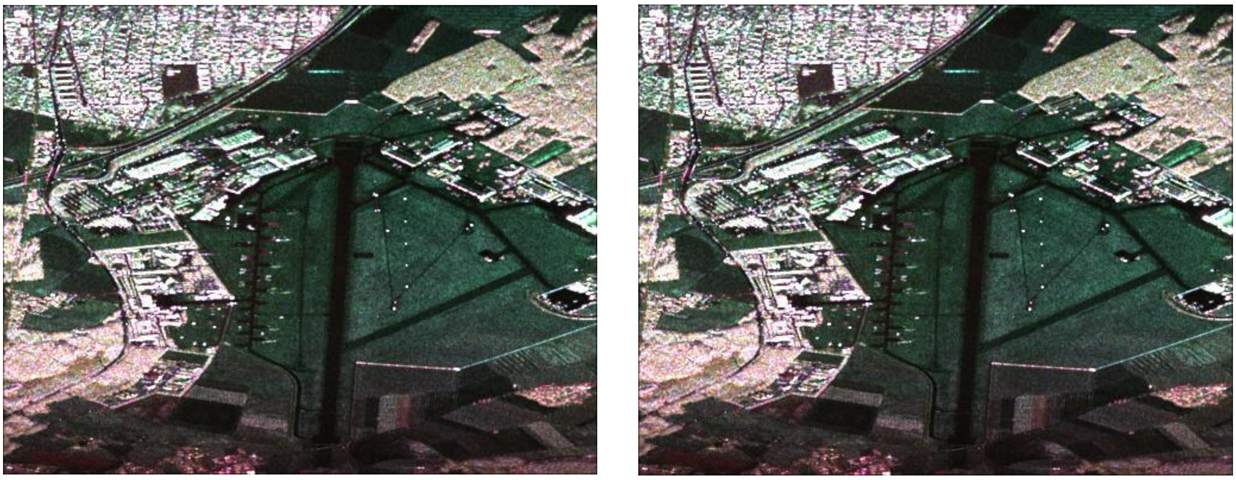

c) RGB pseudo reconstruction by Nord.

d) RGB pseudo reconstruction by CP_{az} algorithm.

Figure E.36 – Comparison of original dataset (Full-POL), Souyris, Nord, and CP_{az} algorithm when $\Psi = 20^\circ$.

e.4 Faraday Rotation angle $\Psi = 30°$

Table E.6 – Statistics of the images for $\Psi = 30°$.

Pearson correlation coefficient			
Method/Image	Mhh	Mhv	Mvv
Souyris	0.94	0.91	0.91
Nord	0.94	0.91	0.91
CP_{az}	0.94	0.89	0.91

a) Pearson correlation coefficient

RMSE			
Method/Image	Mhh	Mhv	Mvv
Souyris	574.34	519.26	592.33
Nord	564.76	510.64	580.76
CP_{az}	548.77	636.48	561.62

b) RMSE

Maximum amplitude value of the images for each channel			
Max/Image	HH	HV	VV
Full-POL	23393.70	23832.50	16221.70
Souyris	31764.30	25568.50	25786.00
Nord	31764.30	25568.50	25786.00
CP_{az}	31764.30	31730.80	25786.00

c) Maximum amplitude value of the images for each channel

RMSE percentage error			
Max/Image	HH	HV	VV
Souyris	0.02	0.02	0.02
Nord	0.02	0.02	0.02
CP_{az}	0.02	0.02	0.02

d) RMSE percentage error

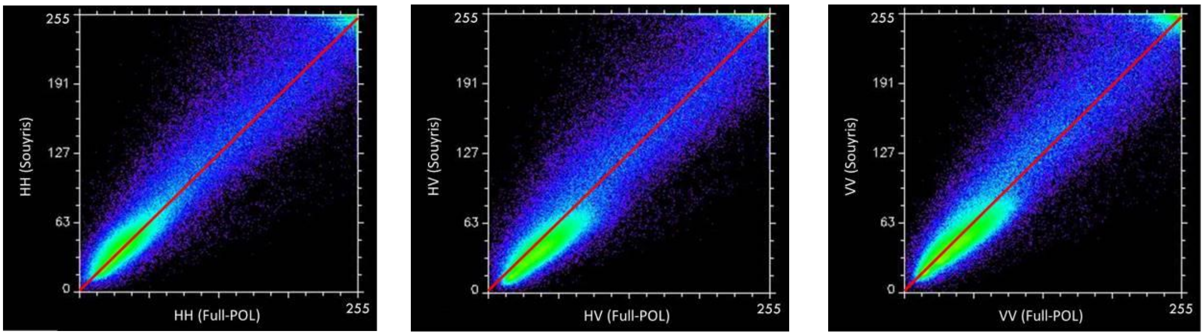

HH (Full-POL x Souyris)
HV (Full-POL x Souyris)
VV (Full-POL x Souyris)

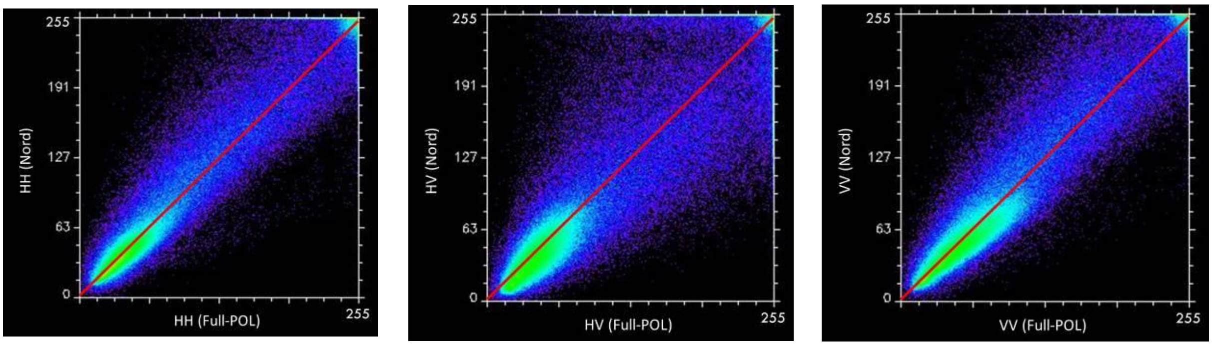

HH (Full-POL x Nord)
HV (Full-POL x Nord)
VV (Full-POL x Nord)

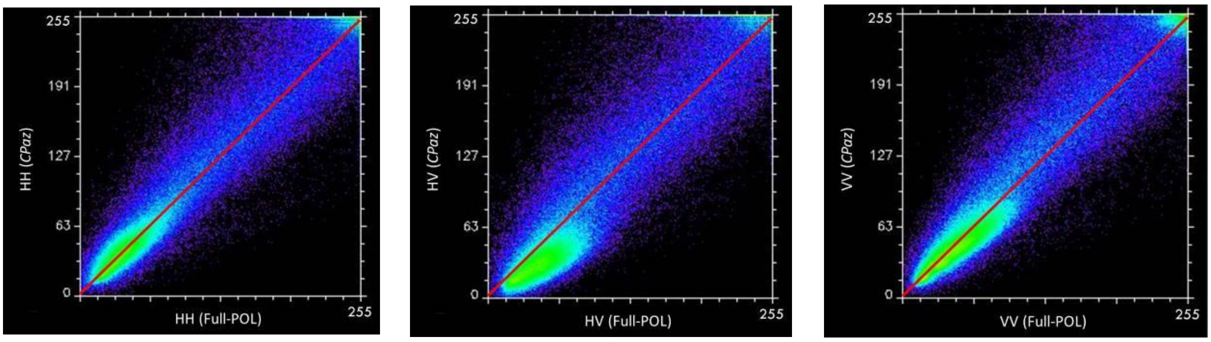

HH (Full-POL x CP_{az})
HV (Full-POL x CP_{az})
VV (Full-POL x CP_{az})

Figure E.37 – Scatter plots HH, HV, and VV of original dataset (Full-POL), Souyris, Nord, and CP_{az} algorithm when $\Psi = 30^\circ$.

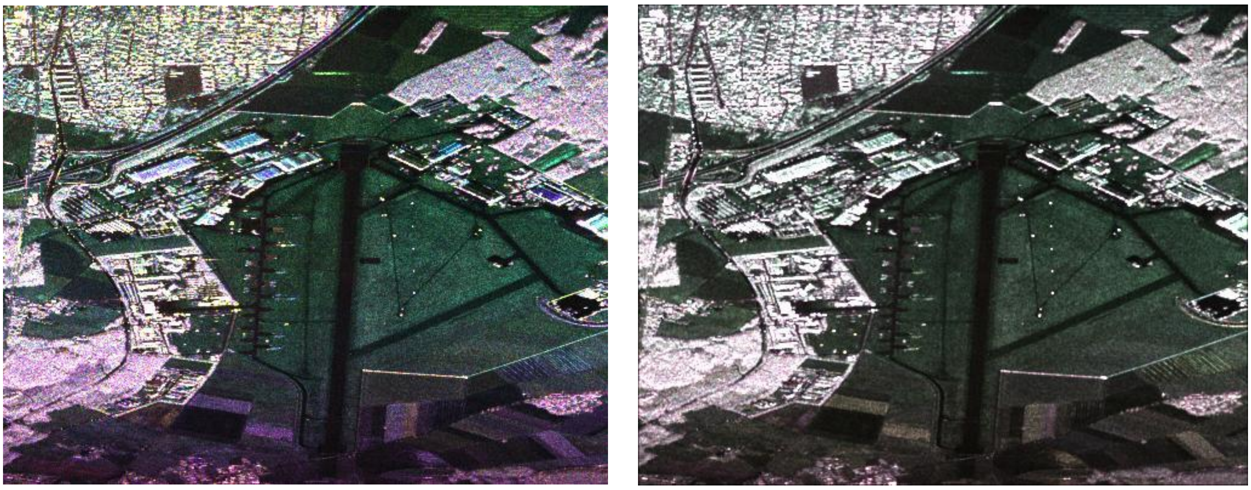

a) RGB E-SAR image.

b) RGB pseudo reconstruction by Souyris.

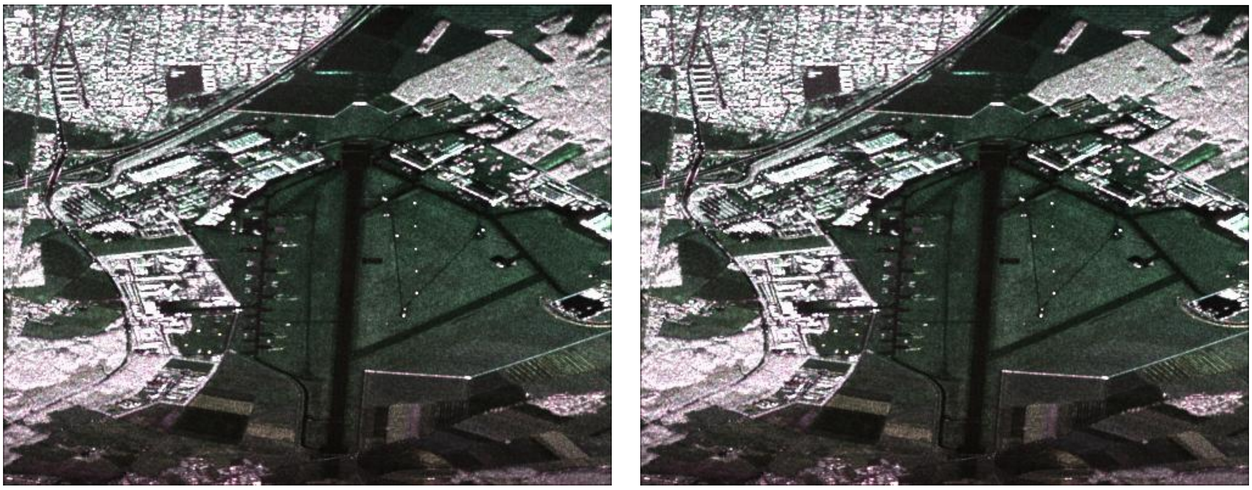

c) RGB pseudo reconstruction by Nord.

d) RGB pseudo reconstruction by CP_{az} algorithm.

Figure E.38 – Comparison of original dataset (Full-POL), Souyris, Nord, and CP_{az} algorithm when $\Psi = 30°$.

e.5 Faraday Rotation angle $\Psi = 40°$

Table E.7 – Statistics of the images for $\Psi = 40°$.

Pearson correlation coefficient			
Method/Image	Mhh	Mhv	Mvv
Souyris	0.92	0.93	0.90
Nord	0.92	0.93	0.90
CP_{az}	0.92	0.93	0.90

a) Pearson correlation coefficient

RMSE			
Method/Image	Mhh	Mhv	Mvv
Souyris	702.50	586.89	723.26
Nord	698.10	583.37	718.61
CP_{az}	696.16	617.61	716.57

b) RMSE

Maximum amplitude value of the images for each channel			
Max/Image	HH	HV	VV
Full-POL	20130.80	25878.90	17499.70
Souyris	30579.20	29211.30	28559.90
Nord	30579.20	29211.30	28559.90
CP_{az}	30579.20	30544.50	28559.90

c) Maximum amplitude value of the images for each channel

RMSE percentage error			
Max/Image	HH	HV	VV
Souyris	0.02	0.02	0.03
Nord	0.02	0.02	0.03
CP_{az}	0.02	0.02	0.03

d) RMSE percentage error

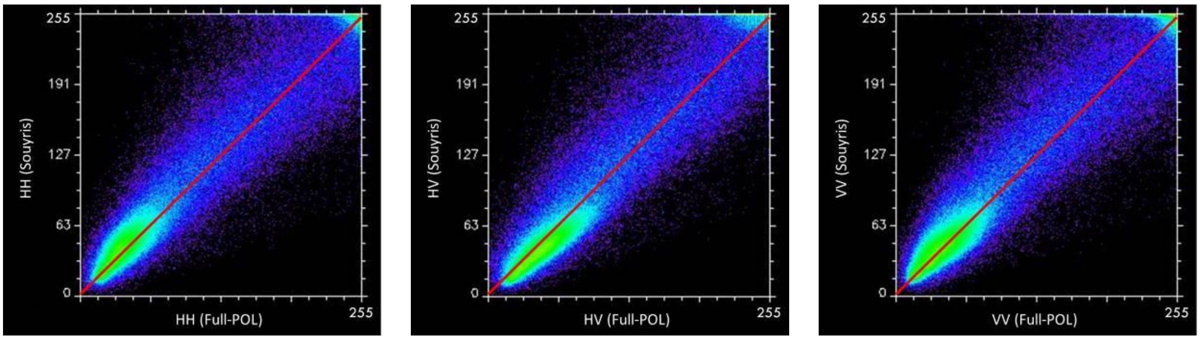

HH (Full-POL x Souyris) HV (Full-POL x Souyris) VV (Full-POL x Souyris)

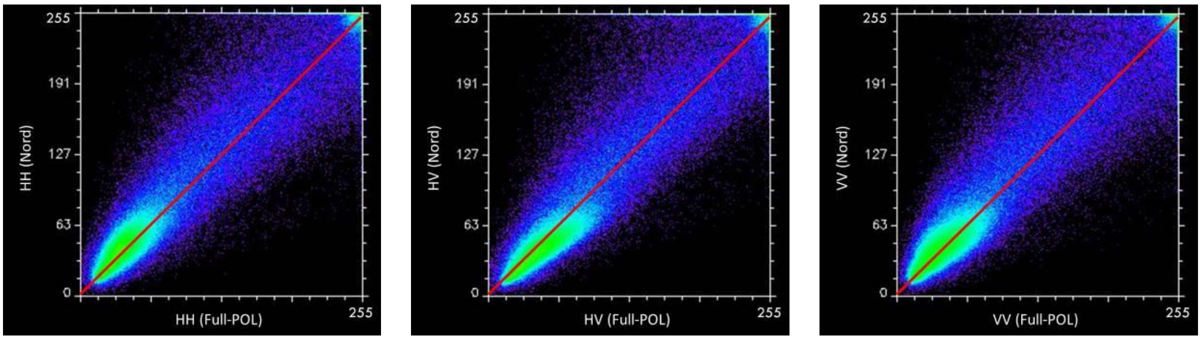

HH (Full-POL x Nord) HV (Full-POL x Nord) VV (Full-POL x Nord)

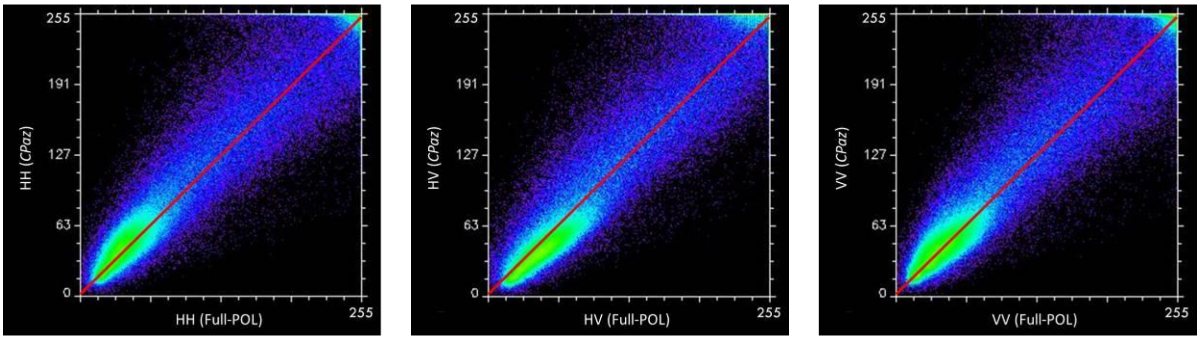

HH (Full-POL x CP_{az}) HV (Full-POL x CP_{az}) VV (Full-POL x CP_{az})

Figure E.39 – Scatter plots HH, HV, and VV of original dataset (Full-POL), Souyris, Nord, and CP_{az} algorithm when $\Psi = 40°$.

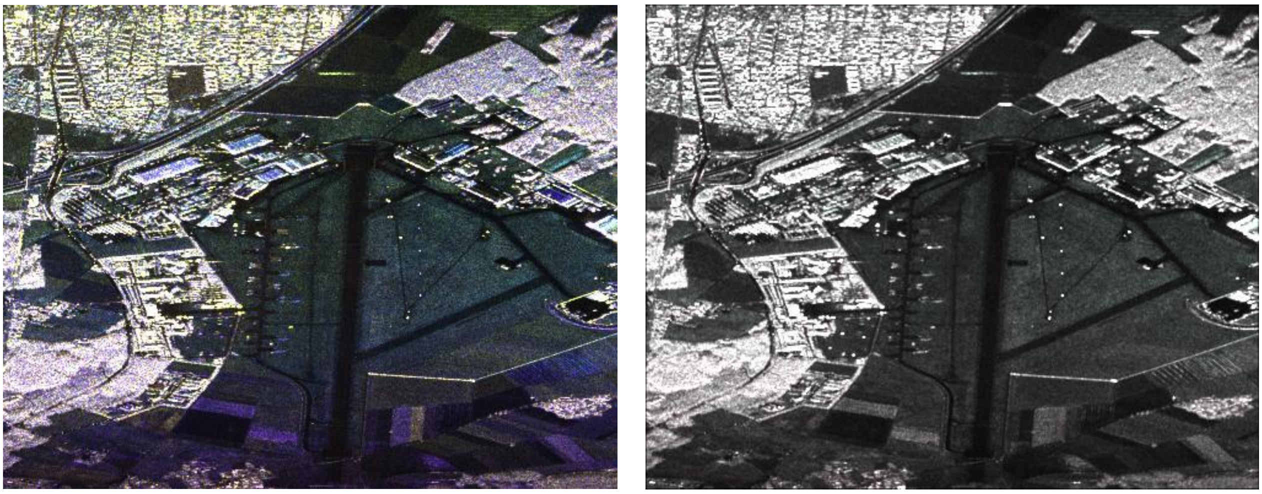

a) RGB E-SAR image.

b) RGB pseudo reconstruction by Souyris.

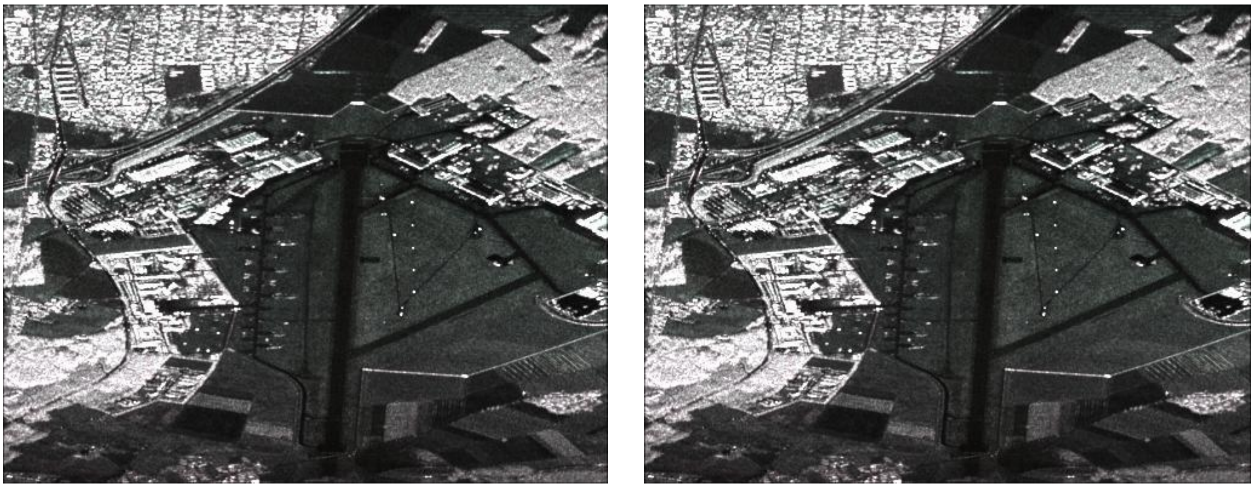

c) RGB pseudo reconstruction by Nord.

d) RGB pseudo reconstruction by CP_{az} algorithm.

Figure E.40 – Comparison of original dataset, Souyris, and CP_{az} algorithm when $\Psi = 40°$.

APPENDIX F – Radar Frequency Bands

Table F.8 – Radar Frequency Bands [64].

Band	Rated Frequency Range	Frequency Range ITU (Region 2)
HF	3-30 MHz	
VHF	30-300 MHz	138-144 MHz 216-225 MHz (P Band)
UHF	300-1000 MHz	420-450 MHz / 890-942 MHz
L	1-2 GHz	1215-1400 MHz
S	2-4 GHz	2300-2500 MHz / 2700-3700 MHz
C	4-8 GHz	4200-4400 MHz / 5250-5925 MHz
X	8-12 GHz	8,5-10,68 GHz
Ku	12-18 GHz	13,4-14 GHz / 15,7-17,7 GHz
K	18-27 GHz	24,05-24,25 GHz / 24,65-24,75 GHz
Ka	27-40 GHz	33,4-36 GHz
V	40-75 GHz	59-64 GHz
W	75-10 GHz	76-81 GHz / 92-100 GHz
mm	110-300 GHz	126-142 GHz / 144-149 GHz / 231-235 GHz / 238-248 GHz

FOLHA DE REGISTRO DO DOCUMENTO

1. CLASSIFICAÇÃO/TIPO TD	2. DATA 21 de janeiro de 2020	3. REGISTRO N° DCTA/ITA/TD-046/2019	4. N° DE PÁGINAS 152

5. TÍTULO E SUBTÍTULO:

Compact Polarimetry Reconstruction Algorithm for a Geophysical Media with Volumetric Scattering using L-band Quad-POL Data

6. AUTOR(ES):

Márcio Martins da Silva Costa

7. INSTITUIÇÃO(ÕES)/ÓRGÃO(S) INTERNO(S)/DIVISÃO(ÕES):

Instituto Tecnológico de Aeronáutica - ITA

8. PALAVRAS-CHAVE SUGERIDAS PELO AUTOR:

1. Compact Polarimetry. 2. Radar polarimetry. 3. Radar remote sensing. 4. Spaceborne radar. 5. Synthetic Aperture Radar (SAR).

9.PALAVRAS-CHAVE RESULTANTES DE INDEXAÇÃO:

Polarimetria; Radar de abertura sintética; Sensoriamento remoto; Algoritmos; Engenharia eletrônica.

10. APRESENTAÇÃO: **(X) Nacional ( ) Internacional**

ITA, São José dos Campos. Curso de Doutorado. Programa de Pós-Graduação em Ciências e Tecnologias Espaciais. Área de Sensores e Atuadores Espaciais. Orientador: Angelo Pássaro; co-orientador: Rafael Lemos Paes. Defesa em 28/11/2019. Publicada em 2019.

11. RESUMO:

One of the objectives of the Brazilian Space Program (PEB) is to launch a Synthetic Aperture Radar (SAR) satellite in the next years. To provide subsidies for the future feasibility studies, this Thesis proposes a Compact Polarimetry (CP) reconstruction algorithm for a geophysical media with volumetric scattering. This study considers the L-band, volume scattering mechanisms, and a geophysical medium with azimuthal symmetry properties. The main contribution of this work is the introduction of an algorithm for CP, considering the azimuthal symmetry. This approach is an important issue for SAR satellite systems that will operate in Brazilian low latitudes, especially in regions with volume scattering mechanisms such as the Amazon rainforest, and in the areas of the country covered by ionospheric irregularities, as plasma bubbles and Medium Scale Traveling Ionospheric Disturbances (MSTIDs). The process of pseudo reconstruction of SAR images obtained from this new CP algorithm presents better results than the CP methods discussed in the literature for the considered scenario. Pearson's correlation coefficient, Root Mean Square Error (RMSE), and scatter plots are used to analyze the pseudo reconstruction process regarding the original Quad-POL images.

12. GRAU DE SIGILO:

(X) OSTENSIVO ( ) RESERVADO ( ) SECRETO